論文 / 著書情報
Article / Book Information

題目(和文)	実験及び分子動力学法による液体鉛合金中の金属不純物拡散に関する研究
Title(English)	Experimental and Molecular Dynamics Study on Metallic Impurity Diffusion in Liquid Lead Alloys
著者(和文)	高雲
Author(English)	Yun Gao
出典(和文)	学位:博士(工学), 学位授与機関:東京工業大学, 報告番号:甲第10497号, 授与年月日:2017年3月26日, 学位の種別:課程博士, 審査員:高橋 実,竹下 健二,加藤 之貴,小林 能直,塚原 剛彦
Citation(English)	Degree:Doctor (Engineering), Conferring organization: Tokyo Institute of Technology, Report number:甲第10497号, Conferred date:2017/3/26, Degree Type:Course doctor, Examiner:,,,,
学位種別(和文)	博士論文
Category(English)	Doctoral Thesis
種別(和文)	要約
Type(English)	Outline

DOCTORAL DISSERTATION

Experimental and Molecular Dynamics Study on Metallic Impurity Diffusion in Liquid Lead Alloys

A dissertation submitted for the degree of

Doctor of Engineering

in the Department of Nuclear Engineering

Tokyo Institute of Technology

by

Yun GAO

Supervised by
Professor Minoru TAKAHASHI

Department of Nuclear Engineering

Graduate School of Science and Engineering

Tokyo Institute of Technology

March 2017

CONTENTS

ABSTRACT

Fe and Ni diffusion in liquid Lead-bismuth eutectic (LBE) and Pb-17Li (17mol% Li) are studied experimentally and computationally. A conventional long capillary method is improved to perform the diffusion experiment and a new measurement method by using ion exchange ion chromatography with ICP-MS is developed to measure the diffused Fe and Ni concentrations. On the other hand, the classical molecular dynamics simulation where the potential energy of the atoms are presented by using embedding atom method is developed and applied to simulation the Fe and Ni diffusion in liquid LBE and Pb-17Li. The quantitative and qualitative study of Fe and Ni diffusion in both liquid LBE and Pb-17Li are estimated by those experimental and computational methods. The temperature dependence of Fe and Ni diffusion coefficients are obtained experimentally. It is found that the diffusion coefficients increase with temperature and they are independent on the time. The diffusion coefficient of Fe is lightly bigger than that of Ni in liquid LBE since the radius of Fe is bigger than Ni. The diffusion of Fe and Ni in liquid Pb-17Li at temperature of 723K show roughly the same value. It is assumed that the diffusion coefficient of Fe is smaller than that of Ni at temperature lower than 723K and the diffusion coefficient of Ni is smaller than that of Fe at temperature higher than 723K through the experimental results.

On the other hand, the simulation results show that Fe and Ni atom aggregation happen during the diffusion when temperature is not sufficiently high. The atomic diffusion of Fe and Ni are in good agreement with the theoretical results from Stokes Einstein, however, they are 1 order in magnitude bigger than the experimental results. It is considered that the aggregation of Fe and Ni atoms happened just after the dissolution in the experiment. Since Fe and Ni are saturated, the atoms aggregate fast, then the formed clusters diffusing into the LBE. According to results comparison, it is also assumed that the aggregation will not happen when the temperature is higher than 2000K and the diffusion would be atomic diffusion. Furthermore, it is found that the diffusion activation energy of Fe is

twice bigger than that of Ni. It is because the radius of Fe is bigger than that of Ni, Fe needs more energy to jump into a vacancy in the liquid LBE. Besides, Fe and Ni atoms show stronger affinity for Bi atom during the diffusion. In case of Fe and Ni diffusion in Pb-17Li, there is no Fe and Ni atom aggregation during the diffusion. Fe atom show stronger affinity for Li atom but Ni atom has stronger affinity for Pb atom during the diffusion. The diffusion activation energy of Fe is lightly smaller than Ni, which shows reverse tendency compared to the diffusion in liquid LBE. This result assume that the diffusion activation energy may also influenced by the affinity. Since Ni has stronger affinity for Pb atom of which radius is significantly larger than Li atom, Ni needs more energy to jump to the vacancy site. Besides, the diffusion coefficient of Fe increases with decreasing the lithium concentration in solvent. By contrast, the diffusion coefficient of Ni decreases with the lithium concentration. The reasons are considered as the different affinities of Fe and Ni during the diffusion.

Overall, since the liquid LBE and Pb-17Li show similar physical properties to each other, Fe and Ni diffusion coefficient in both alloys show comparable values. However, the diffusion mechanism of them are largely different. It is implied that the corrosion phenomenon of Fe and Ni in liquid LBE may differ from that in liquid Pb-17Li.

ACKNOWLEGEMENT

Firstly, I would like to express my deepest gratitude to my academic advisor, Professor Minoru Takahashi for giving me priceless opportunity to work and study about metallic impurity diffusion in lead alloys for future advance reactors in his laboratories. I would like to thank him for nice and kind guidance and supports during the master and doctor courses. By working under his supervision, I could get huge amount of knowledge not only about my own field of research but also many other fields such as thermal dynamics in light water nuclear reactor, oxygen sensors development for lead cooled fast reactor, etc. I also would like to express my special thanks to him for his encouragements whenever I faced the difficulties during the study and research work.

Secondly, I would like to express my sincere gratitude to my advisor Professor Guido Raos in Politecnico di Milano (Polimi). I appropriate all his contributions of time, ideas to teach me how to perform molecular dynamic simulation theoretically and computationally. I appreciate his kind teaching and discussions with me when I stayed in Polimi and also after I came back to Japan. Besides, I also would like to thank Professor Carlo Cavallotti in Polimi for his kind suggestion and collaboration with my simulation study. The determination of modification factor for Fe and Ni which is described in Chapter 5 would not be possible without his Ab-initio simulation.

Thirdly, in my attempted measurements of Fe and Ni diffusion coefficients in liquid LBE and Pb-17Li, I thank Mr. Shoji Matsui gave me lots of technical assistance.to set up the experimental apparatus for high temperature diffusion. For measurements of the diffused Fe and Ni concentration in the specimen, I thank Dr. Nomura very much for his significant contribution. He helped me set up the ion exchange apparatus and taught me how to perform the ion exchange and develop the ion chromatography for separating Fe and Ni ions from the stock solution. Meanwhile, he also taught me how to perform the ICP-MS analysis and always stayed by my side for support. Without his enthusiastic and kind support, the diffusion coefficient of Fe and Ni in liquid LBE and Pb-17Li would not be obtained successfully.

Fourthly, I gratefully acknowledge the Uatom program for financial support that made my Ph.D work possible. I also thank the program together with Prof. Masaki Saito and Prof. Masayuki Igashira for providing me a good opportunity to study abroad for 10 months and study in Japan atomic energy agency (JAEA) for 4 months. Meanwhile I appreciate all the officers in UATOM program for kind supports.

Besides, my special thanks go to all members of my PhD defense committee, Prof. Kenji Takeshita, Prof. Yukitaka Kato, Assoc. Prof. Yoshinao Kobayashi and Assoc. Prof Takehiko Tsukahara for their helpful comments and suggestions. I would also like to thank the other two members of my oral defense of doctoral thesis in UATOM program, Prof. Kazuhiko Kuto from Kyushu Univ. and Prof. Vladimir Artisiuk from Rosatom Central Institute for Continuing Education & Training for their time and insightful questions and comments.

My time at Tokyo Institute of Technology was made enjoyable due to many friends and groups that became a part of my life. I am grateful for time spent with all my lab mates in Takahashi laboratory, Adhi for his kind discussion about my study and also the dissertation, Dr. Mereu for his kind suggestion and guidance to study in Polimi together with his life support when I stayed in Polimi, Dr. Pramuditya, Dr Inaba, Dr Dan, Maehara, Tanabe, Watanabe, Marion, Mihalache, Radu, for all of their nice discussions and friendship during these 5-year-stay in Takahashi Lab. It would be unforgettable memories on my life.

Finally, I would like to thank my family for all their love and encouragement. For my parents who raised me with a love of science and supported me in all my pursuits. For my Japanese host family and friends in Niigata for their warm encouragements. And most of all for my loving, supportive, encouraging and patient partner Keisuke Tsukada whose faithful support during the final stages of this Ph.D is so appreciated. Thank you.

Yun GAO

Tokyo Institute of Technology

LIST OF FIGURE

Chapter 1

Chapter 2

Chapter 3

Chapter 4

Chapter 5

Chapter 6

Chapter 7

LIST OF TABLE

NOMENCLATURE

J: Mass transfer flux	[cm/s]
k: Mass transfer coefficient	[cm/s]
Sh: Sherwood number	[-]
δ: Thickness	[cm]
L: Bulk length	[cm]
C_s: Solubility	[wt% or wppm]
C: Concentration	[wt%]
D: Diffusion coefficient	[cm^2/s]
t: Time	[s]
T: Absolute temperature	[K]
E_a: Diffusion activation energy	[J/mol]
x: Distance	[cm]
E: Potential energy	[eV]
Φ: Two body potential energy	[eV]
f: Effective electron density	[-]
ρ: Density	[g/cm^3]
β: Thermal expansion coefficient	[K^{-1}]
C_p: Isobaric heat capacity	[J/K mol]
η: viscosity	[Pa S]

Chapter 1 Introduction

1.1. Background

Liquid metals have been studied since the early phase of development of fission energy as reactor core coolants of fast reactors (FRs) **[1-1]**, fusion reactor blanket **[1-2]** and more recently as reactor core coolant and spallation target of accelerator driven systems (ADS) proposed for high-level radioactive waste transmutation **[1-3]**. Liquid metals are attractive because of the apparent simplicity of the core or blanket systems in the reactor. Liquid lead alloy is one of the candidate metals, because of its favorable nuclear, thermal hydraulic and chemical properties.

In the fission energy field, lead-bismuth eutectic, so-called LBE, which is a binary alloy of 44.5wt%Pb and 55.5wt% Bi, has been considered as a coolant for FR in 1950s by A. I. Leypunsly **[1-4]** and spallation target for ADS. It has low melting point of 124.5°C, high boiling temperature of 1670°C, low chemical reactivity with water and air and good neutron yield. The high boiling temperature heightens the reliability of heat removal from the core, and assures safety due to lack of a crisis due to heat transfer. Moreover, coupled with a safeguard casing of the reactor vessel, loss of coolant accidents (LOCA) have been eliminated **[1-5]**. LBE is chemically inert. It reacts only slightly with water and air. Progression of the processes caused by tightness loss in the primary circuit and the steam generator's (SG) inter-circuit leaks will occur without release of hydrogen and without any exothermic reactions. There are no materials within the core and reactor facility which release hydrogen as a result of thermal and radiation effects and chemical reactions with coolant. Therefore, the likelihood of chemical explosions and fires as internal events is virtually eliminated. Furthermore, LBE are weak absorbers of neutrons, however, they are good scatters. These facts beneficially affect the neutron-physical characteristics of the reactor. In addition, the density of LBE strongly depends on temperature which contributes to development of natural circulation.

In the fusion energy field, lead-17lithium (Pb-17Li) which is composed of 17mol% lithium was proposed as one of the tritium breeding materials since 1980s **[1-2]**. Since Pb-17Li shows low chemical reactivity with water and air compared to the pure lithium blanket, this chemical property makes it easier to use in the reactor. The lead in Pb-17Li blanket can also play a role of a neutron multiplier in the reactor system. Besides, it, as distinct from the solid breeder compounds, presents the possibility of self-cooling, i. e. the liquid Pb-17Li can also be the heat transfer and transport fluid because of its high thermal conductivity.

However, LBE and Pb-17Li show high aggressiveness for conventional structural materials **[1-1, 1-2, 1-6]**. In the static liquid LBE and Pb-17Li, it is reported that the austenitic steel A316L forms peculiar sponge surface layer depleted in alloying elements with high solubility **[1-7]** and the martensitic steel T91 imposed to liquid LBE has been observed to be uniformly penetrated and to develop a kind of complex oxide surface structure **[1-8]**. **Table 1.1** summarizes the detailed composition of A316L and T91 structural materials. Then, an example corrosion study result on the appearance of A316L cross section after exposing to the liquid LBE at temperature of 848K for 1250 h **[1-9]** is represented in **figure 1.1** and **figure 1.2** shows the A316L cross-section condition after exposing to the liquid Pb-17Li at temperature of 723K for 1250 h **[1-10]**. Both results show that the intensive diffusion by the liquid LBE and Pb-17Li happened after the stable oxide layers on the surface of the steel are dissolved and liquid lead alloys penetrated into the material. Ni and Cr preferentially dissolved in the penetration zone, and mainly Cr redistributed in the material. It is found that dissolution of the Fe matric occurred after the penetrated region is sufficiently depleted in Cr and Ni.

Table 1.1 Main chemical composition of A316L and T91 materials, [wt%]

Material	Fe	Cr	Ni	Mo	Mn	Si	C
A316L	Balance	16	10.1	2.1	1.58	0.51	0.022
T91	Balance	8.3	0.13	0.95	0.4	0.4	0.11

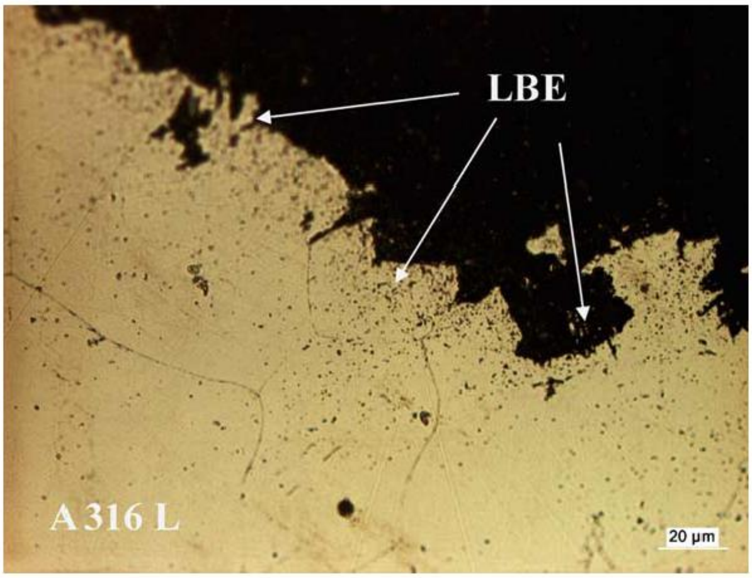

Fig. 1.1 Microscope micrograph of A316L dissolution corrosion mode after exposing to liquid LBE at temperature of 848K for 1250 hours [1-9].

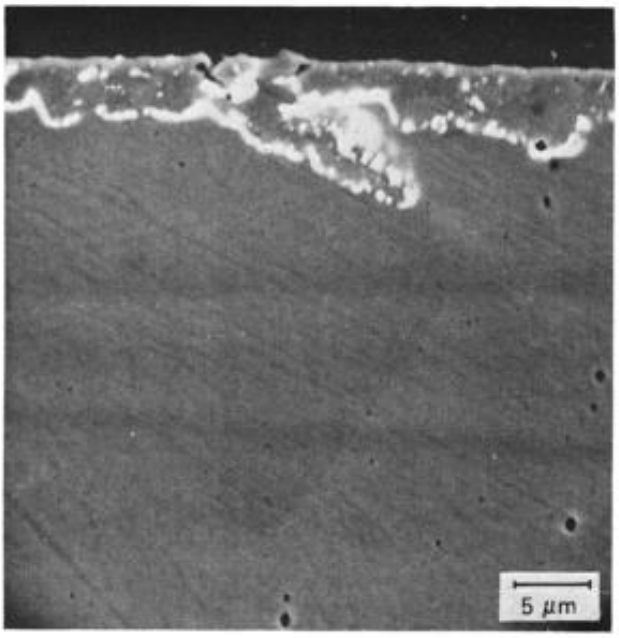

Fig. 1.2 AISI 316L heat-treated at 723K for 3112h in liquid Pb-17Li [1-10].

Comparing to the corrosion in static lead alloy systems, more complicate material corrosion status undergoes in flowing systems. Briefly, the structural materials exposed to flowing lead alloys can undergo corrosion by:

(1) In the hot leg, the components of the solid metal are dissolved into the liquid lead alloy by a surface reaction involving atoms from the solid and the liquid metals or impurities present in the liquid metals as shown in **Fig. 1.3**. In the dissolution process, two stages can be identified. The first stage involves “cleavage" of bonds between atoms in the solid metal and the formation of new bonds with atoms of liquid metal or its impurities, in the boundary layer. In this stage, the liquid metal penetrates into the solid materials in the areas where zones with high density of crystal structure defects reaching the surface. The penetration moves along grain boundaries, the specific crystallographic directions, vacancies and pores, the previously formed defects. Once this occurs, the dissolved atoms diffuse through the boundary layer into the penetrated liquid metals and it is called diffusion penetration—the second stage in the dissolution process.

(2) The dissolved atoms will be transported by the liquid metal bulk when the oxygen concentration in the bulk is very low. Then, those atoms will precipitate on the surface of the steels at low temperature region as seen in **Fig.1.3**. If there is appropriate concentration of oxygen inside the liquid LBE bulk, the surface of the steel will be oxidized and the oxides can become protective films to protect the structural steel from the dissolution. However, those oxide films can be stripped by the highly turbulent flows and moving along the bulk. If the oxygen amount exceed the concentration for protective oxide film formation, the liquid LBE will be oxidized. The oxides of the structural steel metallic atoms will be oxidized and transported in the bulk. The flow path of a loop or a reactor may be blocked by the oxides at low temperature narrow region.

Thus, in order to use lead alloy in nuclear field, an understanding and mitigation of corrosion and degradation of structural materials in flow LBE and Pb-17Li system are essential issues for the demonstration of technical feasibility of critical and subcritical systems.

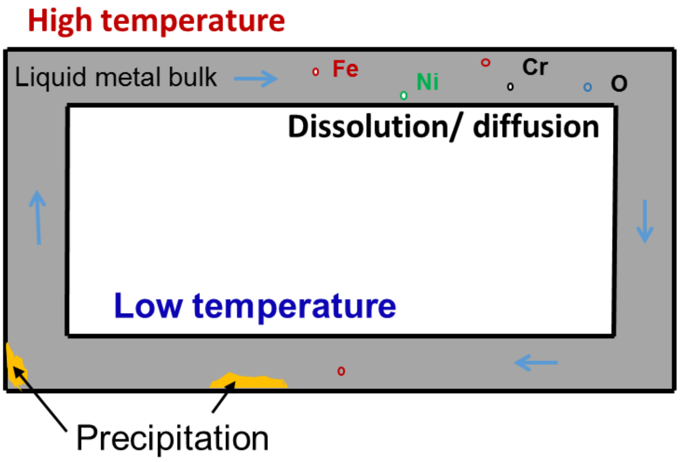

Fig. 1.3 Corrosion in the flowing lead alloy loop.

The quantitatively evolution of Ni, Cr and Fe behavior in both high temperature flowing system is necessary and has been experimentally and analytically studied. In a laboratory scale, several closed loops have been set up to study the laminar flow-affected corrosion mechanisms in case of LBE, although it is difficult and expensive to represent the flowing condition in laboratory. Assuming the corrosion product bulk equaling that in the cold region, Epstein developed a model that could predict the mean corrosion rate of metallic impurities at the hot zone in heat transfer loops in laminar flow condition of Re < 1000 **[1-9]**. Zhang and Li improved the local corrosion models for closed loop systems by including the fact that the amount of the corrosion products at steady state **[1-11]**. However, the mass transport flux in the laminar flow system denoted as following equation:

$$\frac{\partial C_{M/LBE,Pb\text{-}Li}}{\partial t} + \left(u\frac{\partial C_M}{\partial x} + v\frac{\partial C_M}{\partial y} + w\frac{\partial C_M}{\partial z} \right) - \mathrm{D}_{\mathrm{M/LBE,Pb\text{-}Li}} \left(\frac{\partial^2 C_M}{\partial x^2} + \frac{\partial^2 C_M}{\partial y^2} + \frac{\partial^2 C_M}{\partial z^2} \right) = \dot{\mathrm{n}}_{\mathrm{M}} \ , \qquad (1.1)$$

which is a quantitative estimation describing how the elements such as Ni, Cr and Fe transfer in the liquid bulk is still unavailable to clarify, since the diffusion coefficients of the dissolved metals in liquid LBE and also in liquid Pb-17Li are still ambiguous or unknown. Besides, the diffusion coefficient is also an essential parameter to estimate the dissolution flux in viscous sublayer of turbulence flow. In the viscous sublayer shown in

Fig. 1.4, the corrosion of structural materials is controlled by dissolution and the dissolution flux which can be written as **Eq. (1.2)** is influenced by diffusion.

$$J = k(C_s - C_0) = \frac{D}{\delta}(C_s - C_0), \qquad (1.2)$$

The thickness of the viscous sublayer δ can be obtained from the Sherwood number defined as **Eq. 1.3** and the Sherwood number in case of mass transfer along a plane wall can be obtained according to Frossling experimental empirical equation **[1-12]**.

$$\mathrm{Sh} = \frac{k}{D/L} = \frac{D/\delta}{D/L} = \frac{L}{\delta}. \qquad (1.3)$$

Hence, the diffusion coefficient is an important physical property to estimate the mass transport flux together with the dissolution rate in the laminar flow condition. Furthermore, to understand the diffusion phenomena and mechanism of metallic impurity diffusion in both liquid LBE and Pb-17Li are also helpful and important for study the structural material corrosion in flow lead alloy systems.

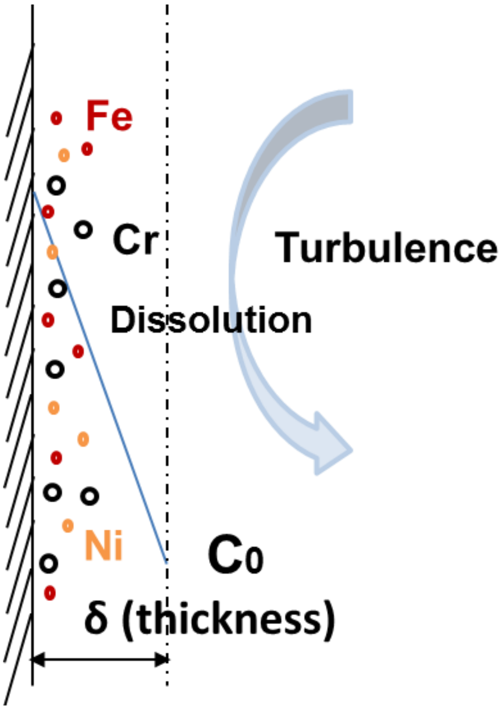

Fig. 1.4 Dissolution in the viscous sublayer of turbulence flow.

1.2. Review of previous studies

1.2.1. Experimental studies of metallic impurity diffusion in liquid metals

The diffusion coefficient of Fe in liquid LBE at temperature of 1023K has been experimentally obtained as 2.27± 0.11×10^{-5}cm^2/s **[1-13]**. A cylindrical specimen is prepared and rotated in liquid LBE, the diffusion coefficient can be calculated by measuring the weight loss and the rotating rate of the cylinder according to the mass transfer coefficient developed by Eisenberg **[1-14]**. By using this experimental method, Simon also obtained the diffusion coefficient of Fe in liquid Pb-17Li at temperature of 873K as 5.09×10^{-14}cm^2/s **[1-15]** and Robertson obtained the diffusion coefficient of Fe in liquid lead as 5.26×10^{-5}cm^2/s at temperature of 773K and as 2.80×10^{-5}cm^2/s at temperature of 1023K **[1-16]**. Since the diffusion coefficients of Fe in liquid LBE and in liquid lead at temperature of 1023K show close results as seen from above values, Balbaud assumed that Fe diffusion coefficient in liquid LBE at temperature of 723K is equal to that in liquid lead and obtained as 5.26×10^{-5}cm^2/s **[1-17]**.

Besides, long capillary method has been used to perform the Ni diffusion in liquid LBE in temperature range of 823-923K by Yamaki et al **[1-18]**. Fick’s second law which explains the diffusion in unsteady state, was used to calculate the diffusion coefficient of Ni in liquid LBE. The Ni powder was put on the top of the liquid LBE and the dissolved Ni atoms diffused into the liquid LBE. The diffused Ni concentration in LBE was measured directly by inductively coupled plasma mass spectrometry (ICP-MS) against distance. Then, according to the concentration distribution and Fick’s second law, Ni diffusion coefficient was obtained as 5.0×10^{-6}cm^2/s at temperature of 823K and 6.50×10^{-6}cm^2/s at temperature of 923K. There is no result of diffusion coefficient at temperature of 873K, since large variation exists in the concentration measurement results. **Figure 1. 5** gives an example of measurement result at temperature of 923K.

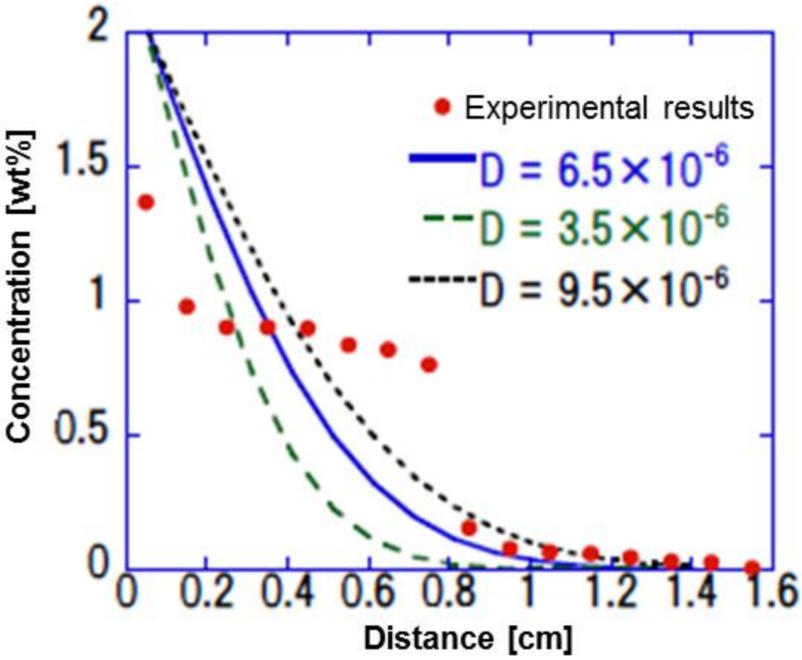

Fig. 1.5 Ni concentration distribution and diffusion coefficient at temperature of 923K **[1-17]**.

However, there are several problems which need to improve. Firstly, it is lack of experimental database on the diffusion coefficient of Fe in liquid LBE at temperature lower than 1023K. Since the temperature range in LBE cooled reactor is designed roughly as 673-923K **[1-19, 1-20]** where the maximum temperature is the allowable temperature of the cladding fuel **[1-21]**, the diffusion coefficient of Fe during this temperature range is required. Secondly, although there is a result of Fe diffusion coefficient at temperature of 723K, it is a prediction result without any experimental and analytical evidence. Thirdly, the diffusion coefficient of Fe in liquid Pb-17Li show 2 orders in magnitude smaller than theoretical result obtained from Sutherland-Einstein equation **[1-17]** so that more experimental study would be necessary to make sure the correctness of the result.

On the other hand, in case of Ni diffusion by long capillary method, the diffusion coefficients at several temperatures are derived and it is found that the diffusion coefficient increases with the temperature, however, as shown in **Fig. 1.5**, the measured concentration are scattered and this must largely influence the results of diffusion coefficient. Since the amount of diffused Fe and Ni in the specimen are very few compared to the base components of solvent, it is difficult to obtain the accurate concentration results by direct measurement by ICP-MS. An effective concentration measurement method is required. Besides, the scattering of the concentration may be involved by the convection during the diffusion. Moreover, the diffusion will also be largely influenced if the particle is oxidized, and this also makes influence on the impurity concentration. However, there is no detailed description of the convection, the condition of the as-received Ni powder and also the oxygen concentration in liquid LBE. Hence to know and control the convection during the experiment, the oxygen concentration in liquid LBE may be another issue to improve the experimental results.

Overall, it is important and required to clarify the diffusion characteristics and diffusion coefficient of Fe and Ni in liquid LBE and Pb-17Li. Then, there is necessity to improve experimental condition, the techniques on performance of diffusion experiment together with concentration measurement, as to obtain the accurate results. Therefore, one of the motivations of present study is to establish a reliable experimental methodology and concentration measurement method to perform the Fe and Ni diffusion in liquid LBE and Pb-17Li and then to investigate the diffusion characteristics of both metals in liquid LBE and Pb-17Li.

1.2.2. Analytical studies of impurity diffusion in liquid LBE and Pb-17Li

Molecular dynamics (MD) simulation has been used to study the physical properties of liquid LBE and Pb-17Li from atomic level of view. For instance, ab-initio MD simulation has been applied to study the structure of liquid LBE by C. Song et al **[1-22]**. The pair correlations within liquid LBE has been calculated against several temperatures and it is found that Pb atom shows strongest interactive tendency with Bi atom to form hetero-coordinated pairs. Then, the self-diffusion coefficient of Pb and Bi in liquid LBE are obtained by using Einstein equation. Besides, Fraile et al. simulated the liquid Pb-Li with different Li compositions by using embedding atom method (EAM) **[1-21]**. In

Fraile's study, a new two-body pair potential within alloy was developed and the validity of this potential was verified by calculating and comparing several physical properties of liquid Pb-Li to the experimental results. However, there is no MD simulation on metallic impurity diffusion in both liquid LBE and Pb-17Li since now. It is because it is complicate to represent the two-body interactions within the liquid metals, and this is also mentioned by Fraile **[1-23]**.

Thus, the second motivation of present study is to successfully represent the two-body interaction within the liquid metals and then to understand the diffusion mechanism form the microscopic level by applying the MD method to simulate Fe and Ni diffusion in liquid LBE and Pb-17Li.

1.3. Objectives

After reviewing the previous study and considering the motivations, the main purpose of present study is to study the Fe and Ni diffusion in liquid LBE and Pb-17Li experimentally and analytically. In more details, the purposes of present study are listed as follows:

(1) To establish an experimental method of Fe and Ni diffusion in liquid LBE and Pb-17Li, where to improve the experimental techniques on diffusion experiment together with the measurement method in case of very low concentration using ICP-MS;

(2) To investigate the diffusion characteristics of Fe and Ni in liquid LBE, in particular, the dependency of Fe and Ni diffusion coefficient on the liquid LBE temperature and on the oxygen concentration in liquid LBE, then to compare them with each other and experimental literature data, and finally to derive the temperature-dependent correlations of diffusion coefficients of Fe and Ni;

(3) To investigate the diffusion characteristics of Fe and Ni in liquid Pb-17Li, in particular, the dependency of Fe and Ni diffusion coefficient on the liquid Pb-17Li temperature, then to compare them with each other and experimental literature data, and finally to derive the temperature-dependent correlations of the diffusion coefficients of Fe and Ni;

(4) To establish the molecular dynamics (MD) simulation of Fe and Ni diffusion in LBE and Pb-17Li, where the liquid LBE and Pb-17Li models are validated by comparing the analytical results of thermal physical properties such as pair distribution function, density, heat capacity, viscosity etc. to the experimental results and then the diffusion simulations are performed in the valid alloy models;
(5) To interpret the diffusion results obtained by experiment through the MD

simulation, where the analytical evaluation results of Fe and Ni diffusion coefficients are compared to experimental results and the theoretical results from Stokes Einstein equation;

(6) To qualitatively clarify the diffusion mechanisms of Fe and Ni in liquid LBE and Pb-17Li from microscopic view by using MD method.

1.4. Outline of thesis

The outline of the dissertation is shown as follows:

Chapter 1 Introduction – This chapter presents the overview of the dissertation. The first part of this chapter mentions the background about the utilization of liquid LBE and Pb-17Li alloys in nuclear energy field and also introduces the challenging issues when use both of the lead alloys. The related studies are reviewed in details in this chapter. Finally, the purpose of present study is list;

Chapter 2 Experimental method – In this chapter, the detailed information of advance preparation for the materials used in diffusion experiment are given. The experimental apparatus together with the procedure are also introduced. Besides, the original concentration measurement method by using ion exchange chromatography is explained in detail. Finally, Fick's second law, also called diffusion equation is introduced and the calculation method of diffusion coefficient according to Fick's second law is explained;

Chapter 3 Experimental study of Fe and Ni diffusion in liquid LBE – This chapter presents the detailed study results of Fe and Ni diffusion in liquid LBE by using the experimental method as explained in chapter 2. The results show that the diffusion coefficient of Fe and Ni are almost the same although Ni is much more soluble in liquid LBE. Meanwhile, it is estimated that Ni atom aggregation happens during the diffusion through SEM analysis;

Chapter 4 Experimental study of Fe and Ni diffusion in liquid Pb-17Li – This chapter presents the detailed study results of Fe and Ni diffusion in liquid Pb-17Li by using the experimental method as mentioned in chapter 2. The results denote that the diffusion coefficient of Fe in liquid Pb-17Li is almost the same as that in liquid LBE as written in Chapter 3. Meanwhile, it is estimated that Ni atom aggregation happens during the diffusion through SEM analysis;

Chapter 5 Analytical method – MD simulation – The EAM potential which is used to represent the many body interaction within the liquid metal is introduced in this chapter. The determination and calibration of the modification factor which is used to normalize the effective electron density is explained. Besides, the detailed information of temperature and pressure condition of MD simulations are also mentioned. Finally, the calculation method of diffusion coefficient by measuring the mean square displacement of the diffusing particle is also introduced;

Chapter 6 MD simulation of Fe and Ni diffusion in liquid LBE – In this chapter, in order to validate the liquid LBE model, several thermal physical property results are presented firstly. Then, the diffusion simulations are performed in the valid liquid LBE model and the qualitative and quantitative evaluation results of Fe and Ni diffusion from the atomic level of view are given. The results show that Fe diffuses faster than Ni at the same temperature, however, the activation energy of Fe shows bigger value than that of Ni. Besides, it is found that Fe and Ni atoms aggregate during the diffusion;

Chapter 7 MD simulation of Fe and Ni diffusion in liquid Pb-17Li – The same as chapter 6, several thermal physical property results are presented firstly as to verify the liquid Pb-17Li model. Then, the diffusion simulations are performed and the quantitative and qualitative evaluation results of Fe and Ni diffusion are given. The results show that there is no aggregation happen during the Ni and Fe diffusion and the simulation results of Fe diffusion coefficients are in good agreement with the experimental results although the simulation results of Ni diffusion coefficient show less than 10% smaller than the experimental results and;

Chapter 8 Conclusions – This chapter summarized overall conclusions obtained in this study.

References

[1-1] IAEA, “Status of Liquid Metal Cooled Fast Breeder Reactor”, Technical reports series No. 246 (1985).

[1-2] D. P. Jackson, R. A. Verrall, P.M. Garvey, W. N. Selander et al., “ A Review of Fusion Breeder Blanket Technology”, Part 1/Review and Findings, Canadian Fusion Fuels Technology Project (CFFTP) (1985).

[1-3] IAEA, “Accelerator Driven Systems: Energy Generation and Transmutation of Nuclear Waste”, status report (1997)

[1-4] A. I. Leypunsky, Fast Neutron Systems. In Selected Papers. Reminiscence; Naukova Dumka: Kiev, Ukaraine, pp62 (1990).

[1-5] G. Toshisky and V. Petrochenko, Sustainability 4, pp2293-2316 (2012)

[1-6] OECD/NEA, “Handbook on Lead-bismuth Eutectic and Lead Properties, Materials Compatibility, Thermal-hydraulics and Technologies” Chap. 6, pp. 231-274 (2007).

[1-7] H. Tas, S. Malang, F. Reiter and J. Sannier, J. Nucl. Mater. 300, pp178-187 (1988).

[1-8] J. Zhang and N. Li, J. Nucl. Mater. 373, pp351-377 (2008).

[1-9] D. Sapundjiev, S. Van Dyck and W. Bogaerts, Corro. Sci. 48, pp577-594 (2006).

[1-10] V. Coen, P. Fenici, H. Kolbe, L. Orecchia and T. Sasaki, J. Nucl. Mater. 110, pp 108-114 (1982)

[1-11] L. F. Epstein, Liquid Metals Technol. 20, pp67 (1957).

[1-12] N. Frossling, “The Evaporation of Falling Drops” pp 107-216 (1938).

[1-13] J. Zhang and N. Li, Nucl. Technol. 144, pp379 (2003).

[1-14] S. Banerjee, Proceedings of the Fifth International Congress on Metallic Corrosion, Tokyo, Japan, May 21-27, NACE, Houston, Texas, 1974.

[1-15] M. Eisenberg, C. W. Tobias, C. R. Wilke, J. Electrochem. Soc. 101, pp306 (1954).

[1-16] N. Simon, T. Flament and A. Terlain, Int. J. Heat Mass Transfer. Vol. 38, No. 16, pp. 3085-3090 (1995).

[1-17] W. M. Robertson, Trans, TMS-AIME 242, pp2139 (1968).

[1-18] F. Balbaud-Celerier and F. Barbier, J. Nucl. Mater. 289, pp227-242 (2001).

[1-19] E. I. Yamaki, S. Numata, M. Takahashi, W. Wu and A. Hino, Proceedings of 9th International Conference on Nuclear Engineering (ICONE-19), Chiba, Japan, May 16-19, 2011.

[1-20] M. Takahashi, S. Uchida, Y. Yamada, K. Koyama, Progress in Nuclear Energy 50, pp269-275 (2008).

[1-21] 研究報告 “鉛ビスマス冷却中型炉の炉心・燃料設計検討”, JNC TN9400 (2004).

[1-22] C. Song, D. Li, Y. Xu, B. C. Pan, C. S. Liu, Z. Wang, Phys. B 429, pp6-11 (2013).

[1-23] A. Fraile, S. Cuesta-Lopez, A. Caro, D. Schwen and J. M. Perlado, J. Nucle. Mater. 448, pp103-108 (2014).

Chapter 2 Experimental method

2.1. Introduction

Diffusion measurements in liquid on earth are heavily disturbed by buoyancy driven convection of different origins. Besides diffusion in liquid metal requires high attentions to handle the liquid metal at high temperature condition in case of its physical and chemical corrosion. Hence, the diffusion experiment in liquid metals is difficult. As explained in chapter 1.2.1, two kinds of experimental methods has been used to obtain the diffusion coefficient of metallic impurity in liquid lead alloys. Rotating cylinder method **[1-14, 1-17]**, which is an indirect measurement method, allow to calculate the diffusion coefficient if the corrosion process is limited by diffusion. In this case, the diffusion coefficient can be derived according to Eisenberg mass transfer equation **[1-14]** by measuring the weight loss of the rotating cylinder and the rotation rate. However, this method may not be completely reliable. Firstly, the underestimation of the weight loss can be obtained due to the imperfect wetting of the rotating cylinder or insufficient purification of the liquid alloy. Secondly, the corrosion process of the steel (the rotating cylinder) may not be controlled by mass transfer or only partially and the diffusion status is limit and difficult to control. Meanwhile, the convection may interfere the measurements. On the other hand, capillary method which is a direct and basic diffusion measurement method. This method is based on the Fick’s second law which is used to describe the dissolved impurity diffuses from a region of high concentration to a region of low concentration in the liquid metals. Through measuring the concentration distribution of the impurity, the diffusion coefficient can be obtained. Note that in order to obtain an accurate result with this method, the natural convection due to the temperature or concentration gradient is required to suppress. Yamaki et al used this method to perform the Ni diffusion in liquid LBE **[1-18]** as mentioned in chapter 1.2.1. The capillary method is a simple and direct measurement way of diffusion coefficient, besides there is no any flow conditional assumption during the experiment, so that the capillary method is considered as more accurate measurement method than the rotating cylinder method. Therefore, the capillary method is adopted to perform the diffusion experiment in present study and several concerns on the convection during the diffusion, the oxygen concentration in the liquid metals and the condition of as received powders are considered.

Then, since the amount of diffused Fe and Ni in liquid LBE and Pb-17Li are very small, in order to have a thorough concentration analyzation by ICP-MS, ion exchange chromatography is used to elute the destination particles — Fe and Ni from the large amount of based components, and then concentration analysis is performed.

Therefore, the purpose of this chapter is denoted as:

(1) To establish an experimental method of Fe and Ni diffusion in liquid LBE and Pb-17Li by using long capillary method where the convection during the diffusion is suppressed. the oxygen concentrations in liquid metals are controlled and the condition of the as-received powder are checked;

(2) To establish a measurement technique for very low Fe and Ni concentration measurement using ICP-MS where the ion exchange chromatography is developed to elute the small amount of Fe and Ni from the specimen and then the ICP-MS analysis is performed;

(3) To explain the calculation method of diffusion coefficient from measured concentration distribution, where Fick’s second law is used.

2.2. Long capillary method

It is proposed that there are two types of long capillary methods that can be used for the diffusion measurement in liquid. One of them is normal long-capillary method and the other one is modified long capillary method, so-called shear cell method **[2-1, 2-2, 2-3]**. Both methods use capillaries to contain the solvent and solute. The shear cell was developed by Nachtrieb **[2-4]** and Broome **[2-5, 2-6]**. It is an advanced long capillary method for avoiding the convection during initial heating and cooling. Diffusion in the liquid solvent starts by shearing two columns together and ends by dividing the liquid column into several slices. In present study, the normal long-capillary method is used.

Then, the aim in transport measurements in the liquid phase is to suppress convection, since the mass transportation by convection can disturb the diffusion or even exceed transport by diffusion. In case of capillary method, relatively minor radial temperature and concentration gradients can lead to density gradients and hence to buoyancy-driven convection. Thus, in order to reduce the convection, the diameter of the capillary tube is require to decrease. However, the decrease of diameter is limited by the sample preparation and by the increased surface tensor of the liquid solvent. In this study, a long capillary tube with 2mm of inner diameter, 3mm of outer diameter and 150mm of length as shown in **figure 2.1**, is used to perform the diffusion experiments. The thickness of tube is 0.5mm and the thermal conduction between the wall of tube and the liquid metals inside the tube can be ignored. Besides, since the tube is very thin, there is no temperature distribution in the r-direction of the tube, as considered.

On the other hand, the liquid lead alloy is very corrosive to the container material if it is stainless steel. Meanwhile the high temperature liquid metal is very easily oxidized by oxygen. Thus, a capillary made from 40wt%SiO_2-56wt%Al_2O_3 is used in the diffusion experiment, as to prevent the container corrosion by liquid LBE and Pb-17Li. Besides, the diffusion experiment is performed under the inert gas atmosphere.

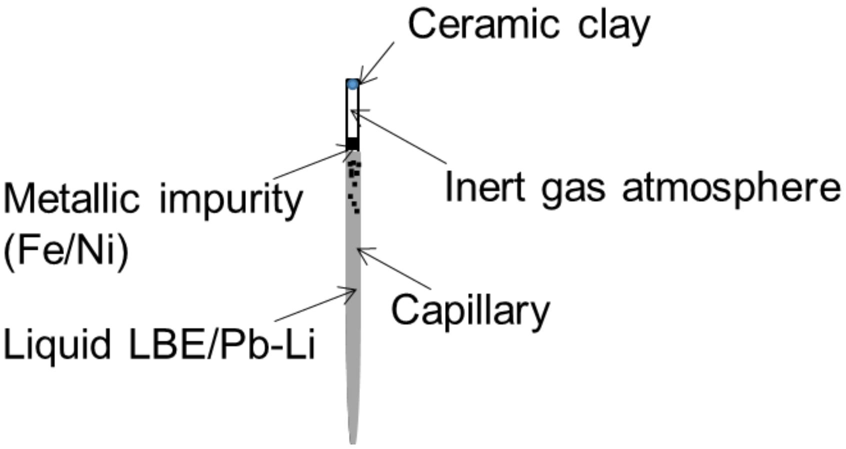

Fig. 2.1 Schematic drawing of the long capillary made from 40wt%SiO_2-56wt%Al_2O_3.

2.3. Experimental apparatus and procedure

2.3.1 Experimental items and advance preparation

The solvents in present study are liquid LBE (Ingot Co.) which is composed of 45%wt of Pb and 55wt% of Bi and liquid Pb-17mol%Li (Ingot Co.). The solutes are Fe atom and Ni atom which are dissolved from the Fe and Ni powders (Nilaco Co.). The impurity of both powders is 99.99%. The radius of Ni powder is 10-20μm and the radius of Fe powder is 325mesh (approximately 44μm). It is considered that the as-received solid LBE, Fe and Ni powders may be oxidized during the manufacture. However, since the component of lithium can be preferentially oxidized if there is oxygen inside the liquid Pb-17Li alloy, it is considered that the oxygen concentration in liquid Pb-17Li is zero. Hence, the oxide reduction reactions of as-received solid LBE, Fe and Ni powders are carried out, respectively.

According to Ellingham diagram as shown in **figure 2.2**, the oxide formation is dependent on the temperature and oxygen potential in the liquid LBE. In case of the same oxide formation, the lower the temperature is, the higher oxygen potential is required according to the diagram. The iron oxide formation can undergo when the oxygen potential in liquid LBE is roughly 10^{-8}wt% at lowest experiment temperature of 773K which will be explained in chapter 3. Therefore, the oxygen concentration in as-received solid LBE is measured by using a solid electrolyte oxygen sensor **[2-7]** before doing the diffusion experiment. The sensor is made of a sintered yttria-stabilized zirconia (YSZ) as show in **figure 2.3**. Oxygen-saturated bismuth (Bi/Bi_2O_3) is used as an internal reference electrode. The percentage of Bi and Bi_2O_3 in the reference electrode is 95:5wt%. The oxygen potential difference between the reference and the liquid LBE induces electromotive force (EMF). The oxygen concentration can be calculated through measuring the EMF by electrometer, since the oxygen concentration has correlation with the output EMF of the sensor as explained in appendix **[A1]**. Thus, the oxygen concentration in as-received LBE is approximately 10^{-3}wt% through the measurement. The dissolved Fe and Ni atoms will be oxidized during the diffusion, in such high oxygen concentration LBE. Therefore, a mixture gas of 20% hydrogen with argon is used to reduce the oxygen concentration in liquid LBE to 10^{-9}wt%.

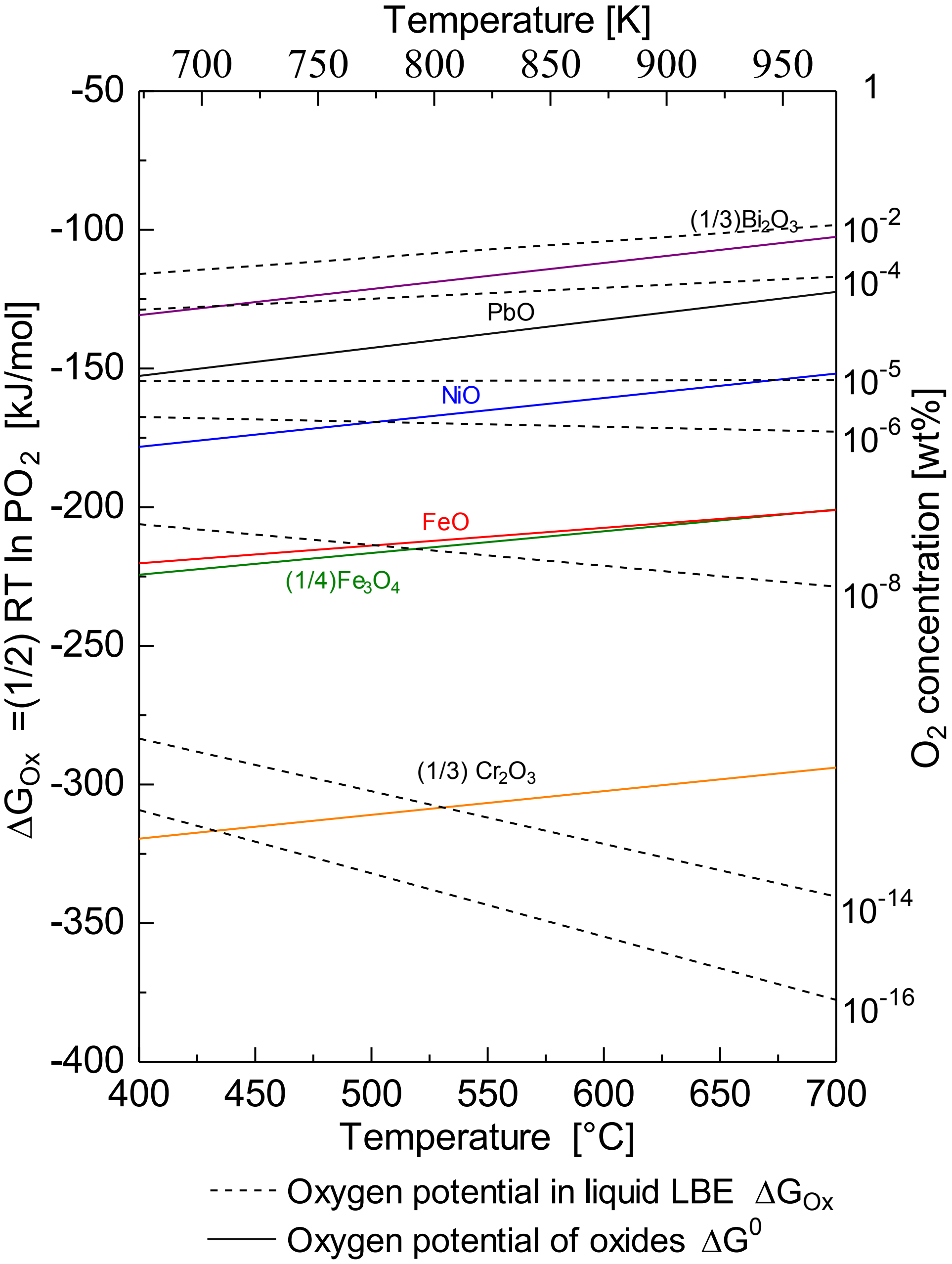

Fig. 2.2 Ellingham diagram on the standard Gibbs free energy of oxide formation.

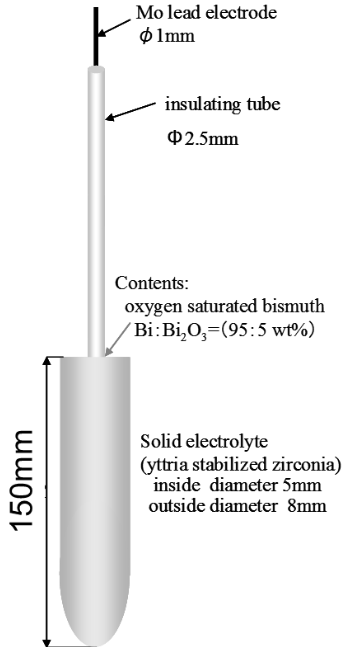

Fig. 2.3 Schematic drawing of the oxygen sensor which the reference electrode is suturated bismuth and the solid electrolyte is made of yttria stabilized zirconia.

Figure 2.4 shows the schematic drawing of the experimental apparatus for oxygen reduction in liquid LBE. 50ml solid LBE per time is sealed inside a ceramic tube, and an oxygen sensor is immersed into the LBE to measure the oxygen concentration. On the other hand, the oxides in the Fe and Ni powders is reduced by using a mixture gas of 3% hydrogen with argon. The reduction temperatures for Fe and Ni are 873K and 773K, respectively and time for reduction is 24 hours. The experimental apparatus and the chemical reactions are shown in **Fig. 2.5**. The powders are placed on a ceramic plate and sealed inside a quartz tube. After supplying the mixture gas for 24 hours, the hot tube containing the pure Fe or Ni powder was moved into the glove box filled of inert gas of argon. The powders were removed from the tube and sealed into a glass container inside the glove box when the quartz tube was cooled down to the room temperature.

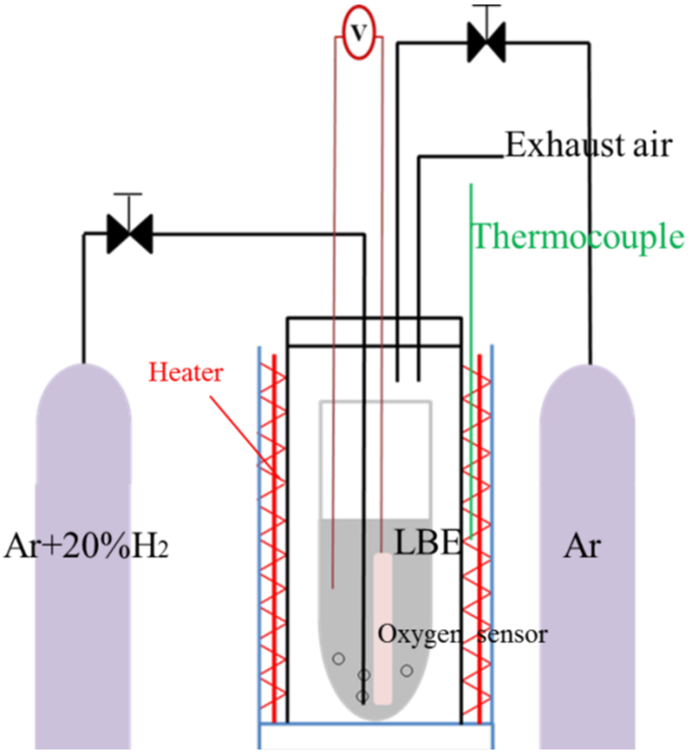

Fig. 2.4 Experimental apparatus for oxygen reduction in liquid LBE at temperature of 773K.

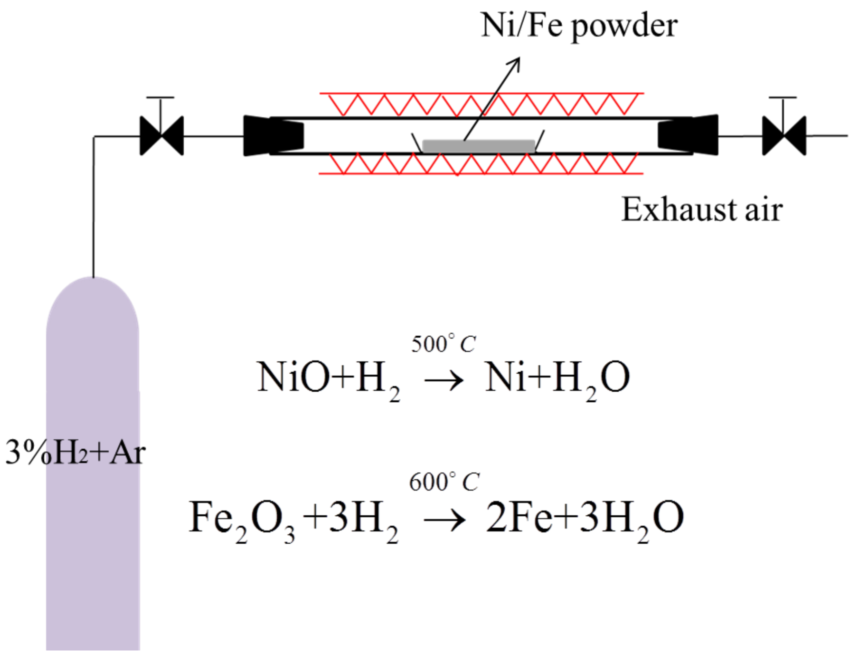

Fig. 2.5 Experimental apparatus for Fe and Ni oxide reduction.

2.3.3 Diffusion experiment apparatus and procedures

The solid LBE after oxygen reducing and Pb-17Li are melt by using an electronic furnace (Electrical Co. of Daika) inside a glove box filled of argon gas. The capability of the furnace is 400℃. **Figure2.6** shows the outside view of the glove box. The temperatures for melting LBE and Pb-17Li solids are roughly 423K and 533K by considering the melting points of both alloys. In case of Pb-17Li, the elimination of lithium oxides after melting is required, since lithium preferentially oxidized if there is oxygen existing inside the liquid metal as mentioned in previous section. As shown in **figure 2.7**, the long capillary tube is vertically immersed into the molten alloy to let the liquid alloy go inside the capillary. However, because of the strong surface tensor of the liquid lead alloys, the liquids cannot flow into the capillary on their own. A long thin stainless steel is used to lead the liquid alloy go inside the capillary and stir the liquid metal inside the capillary in order to make a perfect filling. After the capillary full of roughly 120 mm liquid metal, the capillary is taken out from the liquid pool and 5mg Fe or Ni powders are put on the top of the liquid metal inside the capillary. This capillary is vertically sealed inside a stainless capsule which is pre-heated to the same temperature of the liquid pool by using Swagelok type of tight seal. The capsule is made of a stainless steel 304. Three sheathed thermocouples with 0.5 mm of diameter are inserted into the capsule and fixed on the out surface of the capillary tube to measure its temperature at top, middle and bottom. The capsule is taken out from the glove box and quickly placed inside a high-temperature electronic furnace which has been heated up to the test temperature. The capability of this furnace is 1000℃ and the outside view is shown in **Fig. 2.8**.

Fig. 2.6 Outside view of glove box which is used to melt the solid LBE and Pb-17Li, then manufacturing the liquid lead alloy into a capillary.

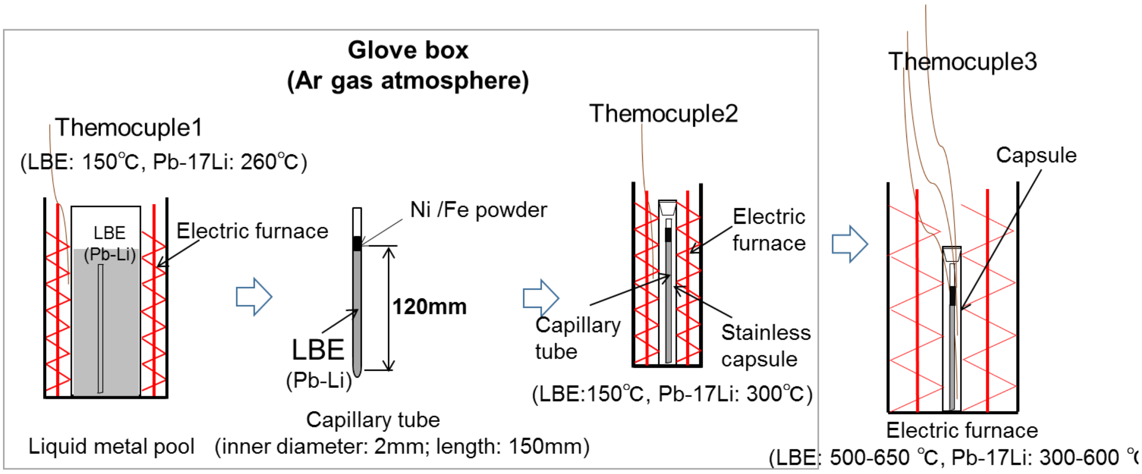

Fig. 2.7 Schematic drawing of experimental apparatus and procedures for Fe and Ni diffusion in liquid LBE and Pb-17Li.

Fig. 2.8 Outside view of high-temperature furnace which is used for diffusion.

Fe and Ni atoms dissolve from the powders and saturated at the top region of the liquid lead alloy firstly, then diffusing downward inside the capillary. After a certain diffusion time, the capsule is taken out from the furnace and cooled down to room temperature by natural air cooling. Because the theoretical diffusion is based on a constant temperature, the diffusion happens during the heating and cooling process introduce some errors into calculations. **Figures 2.9, 2.10** and **2.11** give an example temperature profile including the heating, holding and cooling processes in case of diffusion experiment in liquid Pb-17Li. The black, red and blue lines denote the temperature at the top, middle and bottom of the capillary tube, respectively. Since the temperature at the middle of the capillary tube is the same as that at the bottom, the red line overlapped by the blue line. According to **Fig.2.10**, the temperatures grew to the test temperature within 10 minutes and the temperature increase ratio is roughly 72 K/min. The temperature decreased to the room temperature within 25 minutes which can be known through **Fig.2.11**.

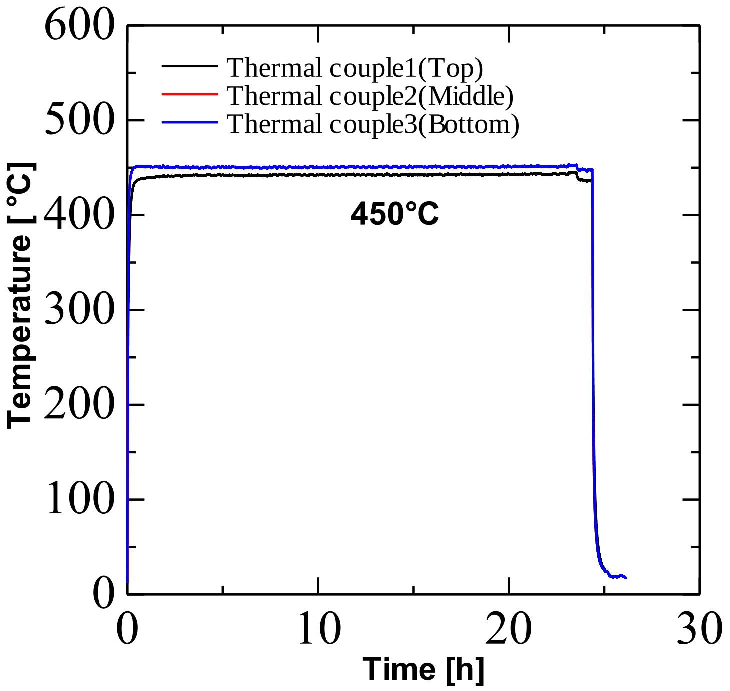

Fig. 2.9 An example of temperature file during the diffusion experiment including the temperature increasing and temperature decreasing periods**.**

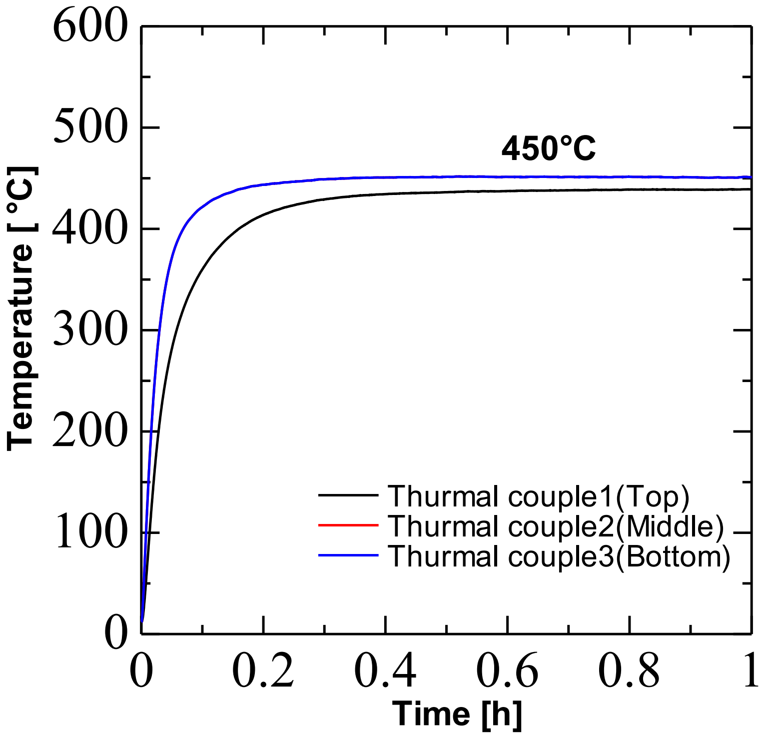

Fig. 2.10 The enlarged view of the temperature during increasing period.

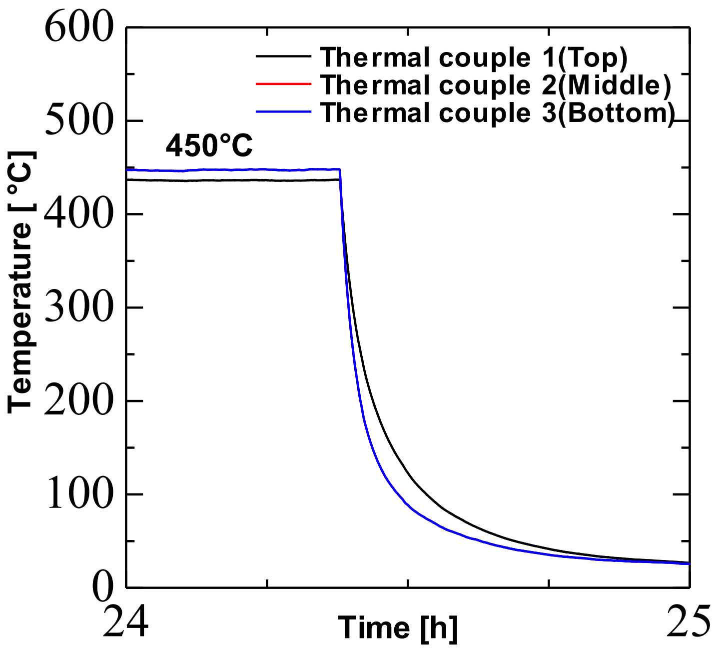

Fig. 2.11 The enlarged view of the temperature during decreasing period.

The average temperature at the top, middle and bottom after the temperatures became constant are shown in **Table 2.1**. It is clearly seen that there is the temperature distribution in the vertical direction of the tube. Thus, in order to make sure whether the convection happened or not, the Rayleigh number by using **Eq. 2.1** was calculated.

$$\mathrm{Ra}_x = \mathrm{Gr}_x \cdot \mathrm{Pr} = \frac{g\beta}{\nu\alpha}(\mathrm{T}_2 - \mathrm{T}_1)x^3, \qquad (2.1)$$

where *x* is the characteristic length, Ra_x is the Rayleigh number for characteristic length *x*, Gr_x is the Grashof number and Pr is Prandtl number, g is the gravity, *v* is the kinematic viscosity, *α* is the thermal diffusivity, *β* is the thermal expansion coefficient and *T* is temperature. The calculated result of Rayleigh number between top and middle position is 0.75, which is very small that there was no convection happened in vertical direction inside the tube. The similar results are obtained in case of other testing temperatures and also in case of diffusion experiments in liquid LBE.

Thus, after cooling and breaking the ceramic tube, a solid specimen shown in **figure 2.12** can be obtained. The solid specimen is cut into small pieces with the axial length approximately 1mm per piece.

Table 2.1 Averaged temperature at top, middle and bottom of the capillary.

Position	Temperature [K]
Top[30mm]	711.7
Middle[75mm]	723.9
Bottom[140mm]	723.9

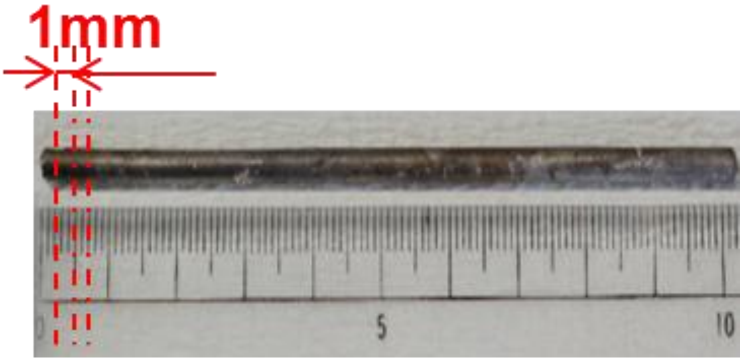

Fig. 2.12 The solid specimen after the diffusion experiment and it is cut into 1mm per piece.

2.3.4 Preparation for measurement sample

The weight of each solid piece m_i (where i is number of the solid piece) is measured after washing by acetone piece by piece and dried. The cleaned solid pieces are chemically dissolved by using nitric acid, respectively. The concentrated aqueous nitric acid is 61% nitric acid base mass and has a density of 1.38 g/ml. Each piece is roughly dissolved with 0.2ml nitric acid, then diluted to 10ml solution by using extra pure water. The concentration of Fe or Ni in each solution sample is measured by using ICP-MS, Agilent 7700 Series from Agilent Technology Company.

2.4. Impurity concentration measurement method

2.4.1 Measurement instrument – ICP-MS

Inductively coupled plasma mass spectrometry, ICP-MS for shorten is an analytical technique used for elemental determinations and elemental concentration measurements. The technique was commercially introduced in 1984 **[2-8, 2-9]** and has gained general acceptance in many types of laboratories. The early adopters of ICP-MS technology was geochemical analysis labs because of its superior detection capabilities, particularly for the rare-earth elements. ICP-MS has many advantages over other elemental analysis techniques such as atomic absorption and optical emission spectrometry, including ICP atomic emission spectroscopy (ICP-AES), including:

(1) Detection limits for most elements are equal to or better than those obtained by graphite furnace atomic absorption spectroscopy (GFAAS).
(2) Ability to handle both simple and complex matrices with a minimum of matrix interferences due to the high temperature of the ICP source.
(3) Superior detection capability to ICP-AES with the same sample throughput.
(4) Analytical working range is nine orders of magnitude.

A high-temperature ICP source with a mass spectrometer is manufactured in an ICP-MS instrument. The ICP source converts the atoms of the elements in the sample to ions. The ions are then separated and detected by the mass spectrometer. **Figure 2.13** shows the cross section of a typical ICP-MS, torch assembly and load coil **[2-8]**, and the schematic representation is shown in **Fig. 2.14**. Argon gas flows inside the concentric channels of the ICP torch. The radio-frequency (FR) load coil is connected to a RF generator. As power is supplied to the load coil from the generator, oscillating electric and magnetic fields are established at the end of the torch. When a spark is applied to the argon flowing through the ICP torch, electrons are stripped of the argon atoms, forming argon ions. These argon ions are caught in the oscillating fields and collide with other argon atoms, forming an argon discharge or plasma.

The sample is typically introduced into the ICP plasma as an aerosol, either by aspirating a liquid or dissolved solid sample into a nebulizer or using a laser to directly convert solid samples into an aerosol. Once the sample aerosol is introduced into the ICP torch, it is completely desolated and the elements in the aerosol are converted firstly into gaseous atoms and then ionized towards the end of the plasma.

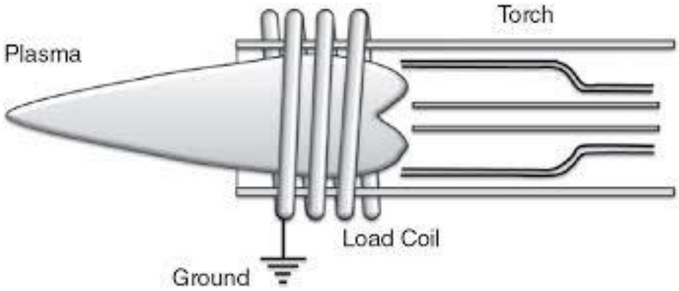

Fig. 2.13 Plasma with torch assembly and load coil **[2-8]**.

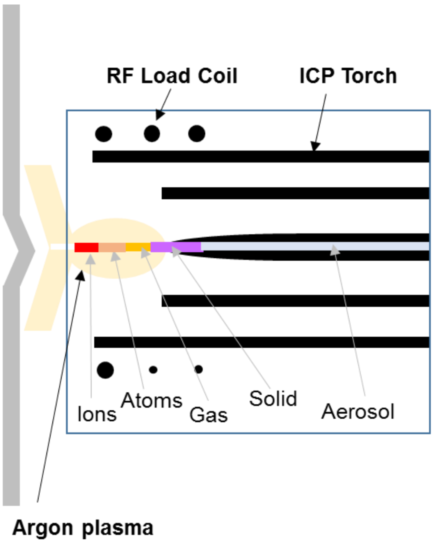

Fig. 2.14 A schematic drawing of ICP torch showing the fate of the sample.

2.4.2 Chromatography of Fe and Ni

The concentrations of target elements of Fe and Ni ions in the sample solution are extremely low compared to the concentrations of Pb and Bi ions. In order to have a thorough analyzation of such low concentration ions, the chromatography is adopted.

Chromatography is an analytical method commonly used for separating a mixture of chemical substances into its individual components according to the differential absorption and elution, so that the individual components can be thoroughly analyzed **[2-10]**. The chromatography was invented by the Russian botanist Mikhail Tsvet in 1906 **[2-11]**. Gas chromatography and solution chromatography are the major subdivisions of chromatography. Column chromatography, thin-layer chromatography, and paper chromatography are subdivisions of solution chromatography based upon the form of the sorption system. These subdivisions may be divided further with respect to the sorption phenomena upon which the separation are based. Examples are adsorption chromatography, partition chromatography, ion exchange chromatography and affinity chromatography. The fundamental principle of chromatography is the separation caused by the different affinity of the different components to stationary phase. In this study the ion chromatography with column is utilized.

Ion exchange chromatography **[2-12]** is the separation of substances by their differential migration on an ion exchange column or on a sheet impregnated ion exchanger. The sample ions are moved down or eluted from the column with an eluent solution as shown in **figure2.15**. This is accomplished through the competition of

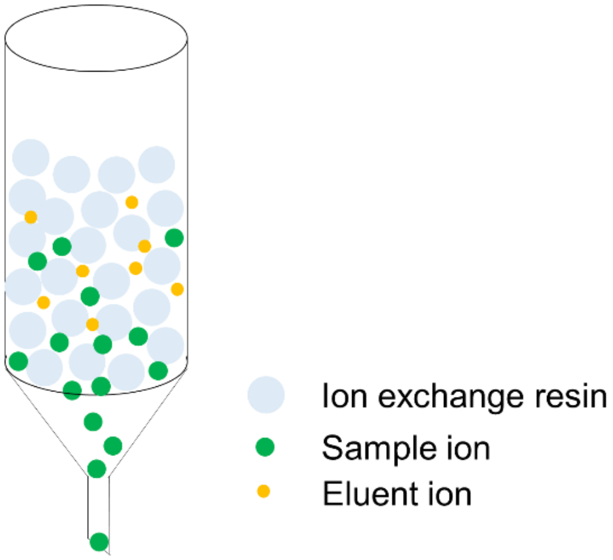

Fig. 2.15 Schematic drawing of ion exchange.

eluent ions and sample ions that react with functional groups on the ion exchanger. The reactions are reversible, so that as a sample ion travels down a column, it will normally "stick" and "unstick" several times. The ability of a sample ion to compete with the eluent ions depends on the characteristics of the ion exchanger and each particular species of sample. The ion exchangers or resigns can be roughly separated by two types—anion resign and cation resign. The schematic illustration of anion resign and cation resign is shown in **figure 2.16**. The stationary phase which is represented as blue area for anion resin consists of a synthetic polymer or resin which contains many positively charged functional groups, usually quaternary ammonium ions. Similarly, the cation resin is an organic polymer with negatively charged sulfonic acid functional groups attached to the benzene rings of the polymer. The positively charged species are attracted to a cation resin's functional groups.

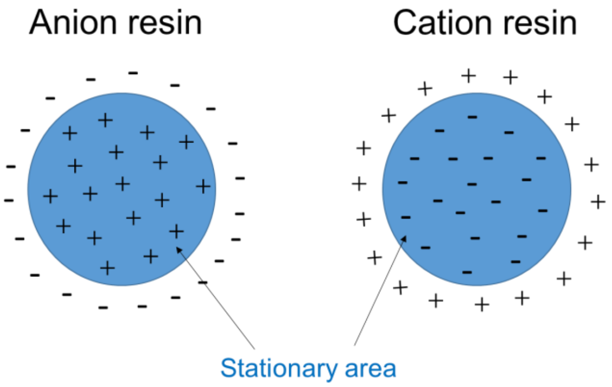

Fig. 2.16 Schematic illustration of anion resin and cation resign.

The cation resin of MP-50 is used to perform the ion exchange since the sample ions are positive metal ions of Pb^{2+}, Bi^{3+}, $Fe^{3+}$and Ni^{2+}. The eluent is a hydrochloric acid for separation of iron and nitric acid for separation of nickel. Both eluents are neutralized in the suppressor and the sample metal ions are converted to a highly-ionized metal hydroxide. Since the affinity of ferric ion in the sample for cation resin is higher than ferrous ion, lead ion and also bismuth ion by considering the relative selectivity of the ion exchange resin, it is difficult to separate Fe^{3+}--Pb^{2+} and Bi^{3+}. **Table 2.1** shows the selectivity of the cation ion exchange resign.

Table 2.2 The selectivity of cation ion exchange resign MP-50 [2-13]

Counterion	**Relative Selectivity**
Li^+	0.85
Fe^{2+}	2.55
Ni^{2+}	3.0
Pb^{2+}	7.5

Thus, Fe^{3+} is reduced to Fe^{2+} by a reducing agent —10w/v% hydroxyl ammonium is mixed to the sample, so that Fe^{3+}can be reduced to Fe^{2+}. $Fe^{2+}$and Ni^{2+}ions can be selectively eluted from the sample solution which contains large matrix of $Pb^{2+}$and Bi^{3+}, the following reactions take place in the ion exchange process.

2M Hydrochloric acid: $H^+ + Cl^- + (Res\text{-}SO_3)_2Fe \rightarrow Res\text{-}SO_3H + FeCl_2$,

2M Nitric acid: $H^+ + NO_3^- + (Res\text{-}SO_3)_2Ni \rightarrow (Res\text{-}SO_3)_2H + Ni(NO_3)_2$,

4M Nitric acid: $H^+ + NO_3^- + (Res\text{-}SO_3)_2Pb \rightarrow (Res\text{-}SO_3)_2H + Pb(NO_3)_2$,

$H^+ + NO_3^- + (Res\text{-}SO_3)_3Bi_2 \rightarrow (Res\text{-}SO_3)_2H + Bi(NO_3)_3$.

These are demonstrated in **figure 2.17** and **figure 2.18**. Fe can be eluted by using 150ml of 2M hydrochloric acid, and Ni can be eluted by using 80ml of 2M nitric acid. The $Pb^{2+}$and Bi^{3+}ions are absorbed by the cation exchange resin since those ions show higher affinity for the resin than $Fe^{2+}$and Ni^{2+}ions when the eluent is dilute hydrochloric acid and nitric acid **[2-14]**. $Pb^{2+}$and Bi^{3+}ions can be removed from the column with a more concentrated eluent of 4M nitric acid. By means of ion chromatography, 99.8% of Fe and Ni ions can be eluted from the origin sample.

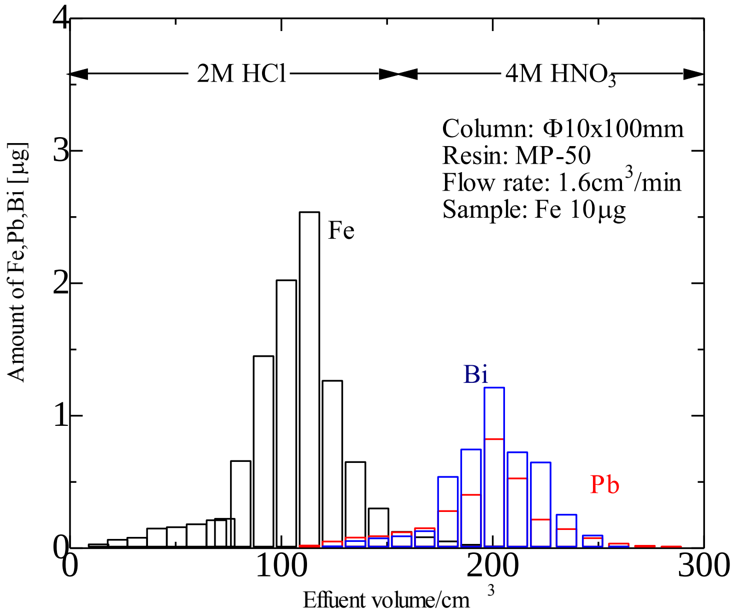

Fig. 2.17 Separation of 10µg Fe, 1µg lead and 1µg bismuth by using cation resin of MP-50. The size of ion exchange column is Φ10×100mm. The flow rate of the eluent is 1.6 cm^3/min.

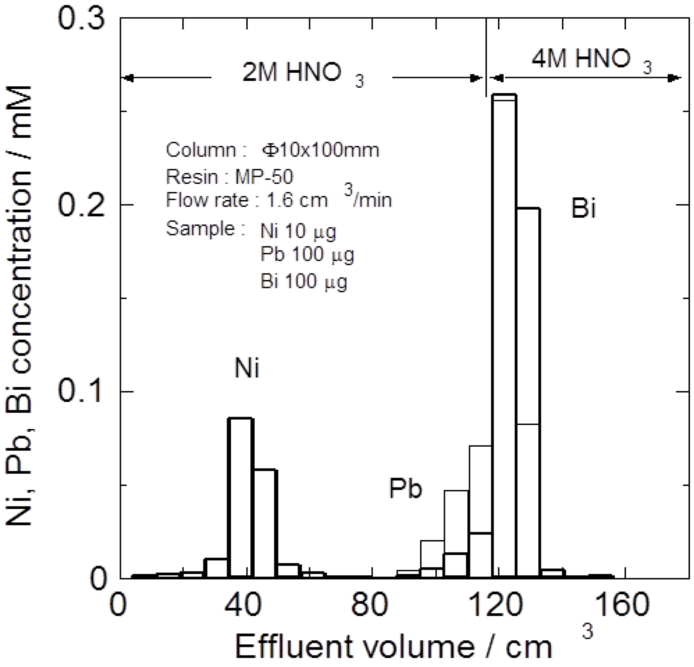

Fig. 2.18 Separation of 10µg nickel, 100µg lead and 100µg bismuth by using cation resin of MP-50. The size of ion exchange column is Φ10×100mm. The flow rate of the eluent is 1.6 cm^3/min.

2.4.3 Measurement procedure

1ml sample solution from each 10ml solution which have been prepared in section 2.3.4 is injected to ion-exchange column to undergo the ion exchange by using the method as explained in section 2.4.2. All the metal ions inside the sample solution are absorbed by the cation resign. The reactions inside the ion exchange resign are shown as follows:

Fe sample: Fe^{2+}+ NO_3^-+ Res-SO_3H→ (Res-SO_3)$_2Fe^2$+ HNO_3,
Ni sample: Ni^{2+}+ NO_3^-+ Res-SO_3H→ (Res-SO_3)$_2Ni^2$+ HNO_3,
Pb sample: Pb^{2+}+ NO_3^-+ Res-SO_3H→ (Res-SO_3)$_2Pb^2$+ HNO_3,
Bi sample: Bi^{3+}+ NO_3^-+ Res-SO_3H→ (Res-SO_3)$_2Bi^3$+ HNO_3.

Then, the Fe^{2+} -- Pb^{2+} and Bi^{3+} separation can be accomplished by using 2M hydrochloric acid and 4M nitric acid. The Ni^{2+} -- Pb^{2+} and Bi^{3+} separation can be accomplished by using 2M nitric acid and 4M nitric acid. The effluent solution is connected every 5 minutes by using fraction collector. The effluent in per collector is almost 8ml and 10 fraction collectors is manufactured and these collected effluent solutions are detected by ICP-MS, respectively. Then, the amount of Fe or Ni in each sample solution $m_{i\,(\mathrm{Fe/Ni})}$, that is the mass of Fe or Ni in each 1mm solid sample, can be calculated as

$$m_{\mathrm{i\,(Fe/Ni)}} = \sum_{j=1}^{8} C_{\mathrm{Fe/Ni}\,,\,j} V \ , \tag{2.2}$$

where V is constant value of 8ml, and $C_{Ew/Ni}$ is measured concentration of Fe and Ni in each collector. The mass percentage of Fe and Ni in each solid piece can be derived from

$$C_{\mathrm{i(Fe/Ni)}}(wt\%) = \frac{m_{\mathrm{i(Fe/Ni)}}}{m_{\mathrm{i}}} \times 100\% \, . \tag{2.3}$$

The m_{i} is the mass of each solid piece as described in section 2.3.4.

Figure 2.19 gave an example measurement result of Ni concentration profile at temperature of 873K in LBE. The plots are corresponded to the diffused Ni concentration in LBE. It is clearly seen that the scattering of the concentration is largely decreased and the measurement accuracy the concentration is less than 0.02wt% compared to the result obtained by Yamaki **[1-18]** as mentioned in chapter 1. Thus, this result presents that the new measurement technique by using ion exchange chromatography can contribute to the reliability of diffusion coefficient result.

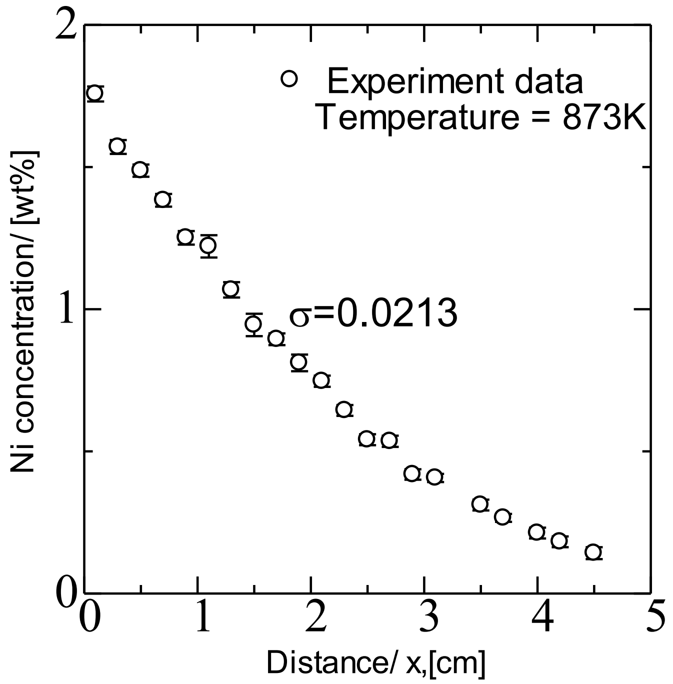

Fig. 2.19 An example measurement result of diffused Ni concentration distribution by using ion exchange chromatography.

2.5. Fick's second law

Fick's second law, also called the diffusion equation, is a partial differential equation and is known as

$$\frac{\partial C}{\partial t} = -\nabla \cdot \mathrm{J} = \mathrm{D}\nabla^{2} C\,, \tag{2.4}$$

where D [cm^2/s] is the diffusion coefficient, J is the flux, C is the concentration. In this study, the diffusion experiment is conducted in a long capillary tube with 2mm inner diameters, so it is probable to think the diffusion happening in one dimension. According to **equation (2.4)**, Fick's second law in one dimension can be written as

$$\frac{\partial C}{\partial t} = \mathrm{D}\frac{\partial^{2} C}{\partial x^{2}}\,. \tag{2.5}$$

One of the solutions by using error function can be expressed as **[2-15]**

$$\frac{C(x,t) - \mathrm{C}_0}{\mathrm{C}_\mathrm{B} - \mathrm{C}_0} = 1 - \mathrm{erf}\left(\frac{x}{2\sqrt{\mathrm{D}t}}\right), \tag{2.6}$$

where $C(x,t)$ [wt%] is the concentration of the solute at distance x [cm] and time t [s]. C_0 is the concentration of solute at the infinity or the background concentration of the solute in the solvent. $\mathrm{C_B}$ is the concentration of the solute at the boundary which is a surface that the solute starts to diffuse. According to equation (5), in order to yield the diffusion coefficient, the solute concentration profile at different time together with the boundary concentration is required though the experiment.

In this study, C_0 is the concentration of Fe and Ni in the liquid LBE or Pb-17Li, which is considered as zero. The concentration at the boundary $\mathrm{C_B}$ is assumed to be equal to the solubility of Fe and Ni in the liquid LBE or Pb-17Li. The solubility of Fe and Ni C_s in liquid LBE **[2-16]** and Pb-17Li **[2-17, 2-18]** versus temperature are denoted as following equations, respectively.

$$\log C_{\mathrm{s(Fe/LBE)}}(wt\%) = 2.1 - 4380 / T(\mathrm{K})\,,\quad (823\mathrm{K} \le T \le 1053\mathrm{K})\,, \tag{2.7}$$

$$\log C_{\mathrm{s(Ni/LBE)}}(wt\%) = 1.53 - 843 / T(\mathrm{K})\,,\quad (673\mathrm{K} \le T \le 1173\mathrm{K})\,, \tag{2.8}$$

$$\log C_{s(Fe/Pb\text{-}17\,Li)}(\mathrm{mol\%}) = 7.236 - 9345 / T(\mathrm{K})\,,\quad (723\mathrm{K} \le T \le 873\mathrm{K})\,, \tag{2.9}$$

$$\log C_{s(Ni/Pb-17Li)}(\mathrm{mol\%}) = 1.3198 - 981.2/T(\mathrm{K}),\quad (520\mathrm{K} \le T \le 728\mathrm{K}). \qquad (2.10)$$

$C(x,t)$ is the Fe or Ni concentration measured by ICP-MS at intermediate distance of each solid piece. The least squares method was used to derive the diffusion coefficient based on Fick’s second law.

2.6. Arrhenius equation

Arrhenius equation **[2-19]** is a simple explanation for the strong temperature dependence of reaction rates. It is proposed by Svante Arrhenius in 1889, based on the van't Hoff equation **[2-20]** for the temperature dependence of equilibrium constant. Currently, the Arrhenius equation is the best seen as an empirical relationship in determining the rate of chemical reaction and activation energy. It can be used to model the temperature variation of diffusion coefficients, population of crystal vacancies etc **[2-21]**. The diffusion coefficient in Arrhenius equation is expressed as

$$\begin{aligned} D &= \exp\left(-\frac{\Delta \mathrm{G}}{\mathrm{R}T}\right) \\ &= \exp\left(\frac{\Delta \mathrm{S}}{\mathrm{R}T}\right)\exp\left(-\frac{\mathrm{H}}{\mathrm{R}T}\right) = \mathrm{D}_0\exp\left(-\frac{\mathrm{E}_a}{\mathrm{RT}}\right), \end{aligned} \tag{2.11}$$

where D_0 is pre-exponential constant, E_a is diffusion activation energy in J/mol, R is gas constant and T is the diffusion temperature in kelvin. This equation can be also written equivalently as

$$\ln D = \ln \mathrm{D}_0 - \frac{E_a}{\mathrm{R}}\left(\frac{1}{T}\right), \tag{2.12}$$

When plotted in the manner expressed above by using semi-logarithmic graph as shown in **figure2.20**, the value of the true y-intercept at x=1/T=0 is correspond to D_0, and the slope of the line is equal to $-E_a/R$. The values of y-intercept and slop can be determined from the experimental points using linear regression. The pre-exponential constant D_0 is an empirical frequency factor of collision. It describes the number of times two particles collide. It is determined by the entropy of diffusing atoms. The entropy describes the disorder or randomness of the diffusion system. Besides, according to the collision theory **[22]**, the frequency of collision is determined by the temperature with respect to the kinetic energy of the particles, the concentration of two particles collide and the surface area of particles collide during the diffusion.

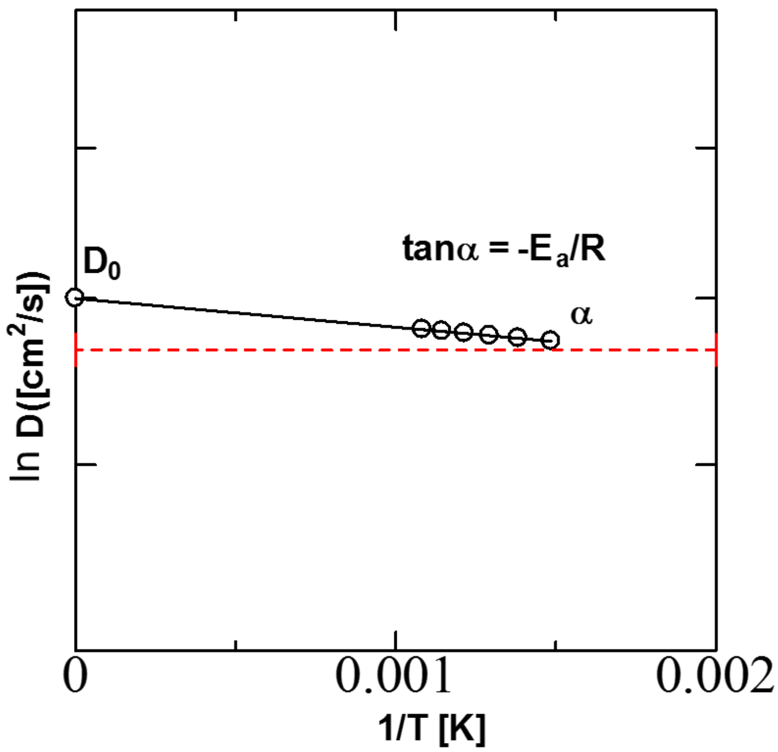

Fig. 2.20 Arrhenius plot of diffusion coefficient. tan*α* is proportional to -E_a/R, where E_a is diffusion activation energy and R is the gas constant. D_0 is the pre-exponential constant.

2.7. Conclusions

The experimental apparatus and procedures of Fe and Ni diffusion in liquid LBE and Pb-17Li are improved and a new concentration measurement method of diffused Fe and Ni by ICP are developed:

(1) Long capillary method has been designed and established to perform the diffusion experiment, where the capillary with 2 mm inner diameter can successfully use to suppress the convection during the diffusion, and the procedures of controlling the oxygen concentration in liquid LBE by using a mixture gas of 20%H_2 with Ar, eliminating lithium oxides in the molten Pb-17Li together with the oxides reduction for as-received Fe and Ni powders make contribution to the reliability of experimental results.

(2) An ion exchange chromatography is developed to elute Fe and Ni from the specimen, and then the concentration analysis is perform by ICP-MS. By using this method, 99.8% of Fe or Ni in the specimen which is obtained in the diffusion experiment can be eluted and the concentration measurement accuracy of Fe and Ni can be improved to 0.002wt%

(3) The least squares method is used to calculate the diffusion coefficient where the non-steady diffusion equation – Fick’s second law by using error function is adopted and the temperature-dependent correlations of Fe and Ni diffusion coefficient are obtained following the Arrhenius equation.

References

[2-1] G. Frohberg, K. H. Kraatz, H. Wever, A. Lodding and H Odelius, Defect Diffusion Forum 66-69 (1989) 295

[2-2] G. Frohberg, “Scientific Results of the German Spacelab Mission D2,” WPF D-2, Cologne (1995) 275

[2-3] Y. Malmejac and G. Frohberg, “Fluid and Material Sciences in Space,” Springer Berlin (1987) pp159

[2-4] H. Nachtrieb and J. Petit, J. Chem. Phys. 24 (1956) 746

[2-5] E. F. Broome and H. A. Walls, Trans. Met. Soc. AIME 242 (1968) 2177.

[2-6] E. F. Broome and H. A. Walls, Trans. Met. Soc. AIME 245 (1969) 739.

[2-7] A. K. Rivai, T. kumagai, and M. Takahashi, Progress in Nucl. Ener. 50 (2008) 575-581.

[2-8] H. E. Taloy, “Inductively Coupled Plasma-Mass Spectrometry practices and Techniques,” Academic Press, California, 2001, pp16-27.

[2-9] 河口　広司，中原　武利，“プラズマイオン源質量分析”，日本分光学会測定法シリーズ　28.

[2-10] E. Heftmann, “Chromatography,” Reinhold Publishing Corp., New York, 2nd Edn. 1967.

[2-11] M. Tswett. *Ber. Deut. Botan. Ges.* **24**, 384 (1906).

[2-12] D. T. Gjerde, and J. S. Fritz, “ Ion Chromatography”, Huting, Heidelberg, New York, 2nd Edn. 1987.

[2-13] 三菱化学, “ダイヤイオン—イオン交換樹脂・合成吸着剤マニュアル基礎編”, 18.

[2-14] Y. Takata, F. Mizuniwa, and C. Maekoya, Anal. Chem. 51 (1979) 2337.

[2-15] 藤田　英一，”金属物理—材料科学の基礎”，アグネ技術センター 第七章 pp193-199.

[2-16] Weeks J. R., ASM Trans. Quart. 58 (1965) p.302

[2-17] H. U. Borgstedt and H. Feuerstein, J. Nucl. Mater. 191-194 (1992) 998-991.

[2-18] M. G. Barker, V. Coen, H. Kolbe, J. A. Lees, L. Orecchia and T. Sample, J. Nucl. Mater. 155-157 (1988) pp732-735.

[2-19] Arrhenius, S.A. (1889). "Über die Dissociationswärme und den Einflusß der Temperatur auf den Dissociationsgrad der Elektrolyte".*Z. Phys. Chem.* 4, pp96–116.

[2-20] A. Peter., D. P. Julio, ”Physical Chemistry” 8th Edn, W.H. Freeman and Company (2006) pp212.

[2-21] K. Connors, Chemical Kinetics, 1990, VCH Publishers

[2-22] M. Trautz, Das Gesetz der Reaktionsgeschwindigkeit und der Gleichgewichte in Gasen. Neue Bestimmung der Integrationskonstanten und der Moleküldurchmesser, Zeitschrift für anorganische und allgemeine Chemie, V. 96, Issue 1 (1916) pp1-28.

Chapter 3 Experimental study of iron and nickel diffusion in liquid LBE

3.1. Introduction

The fundamental study of Fe and Ni diffusion in liquid LBE are experimentally studied by using long capillary method which has been explained in chapter 2. The concentration measurement of diffused Fe and Ni are analyzed by using ICP-MS. The purpose of this chapter is presented as follows:

(1) To derive the diffusion coefficient of Fe and Ni in liquid LBE and clarify the difference of Fe and Ni diffusing in liquid LBE;

(2) To investigate the effect of diffusion time and oxygen concentration in liquid LBE on the diffusion coefficient;

(3) To obtain the temperature-dependent correlation of diffusion coefficient using Arrhenius-type equation and

(4) To clarify and compare the diffusion characteristics of Fe and Ni in liquid LBE by SEM-EDX analysis.

3.2. Experimental condition

The operating temperature of LBE in the practical LBE cooled reactor is from 360℃ to 510℃ **[1-19, 1-20]** and the allowable temperature of the cladding material is 650℃ **[1-19]**. Thus, the diffusion temperature range is determined as 773-923K in order to represent the temperature condition of the reactor. The experiment temperatures are set as 773, 823, 873 and 923K. The diffusion time is 3.5 hours and 7 hours for Ni diffusion and only 7 hours for Fe diffusion. The oxygen reduction experiment for LBE and the oxides reduction experiments for Fe and Ni powders are performed preliminarily.

3.3. Results and discussions

3.3.1. Fe diffusion

One of the example results of diffused Fe concentration distribution in LBE at temperature of 823K is shown in **figure 3.1**. The plots denote the Fe concentration in LBE versus distance. The black plots are corresponded to the results at temperature of 823K, the blue plots are corresponded to the results at temperature of 873K and the red plots show the results at temperature of 923K. The solid lines show the fitting results according to Fick’s second law. In order to verify the validity of the obtained diffusion coefficient of Fe by least squares method, the inverse function method of error function is also adopted to derive the diffusion coefficient of Fe versus temperature and the results are shown in **figure 3.2**.

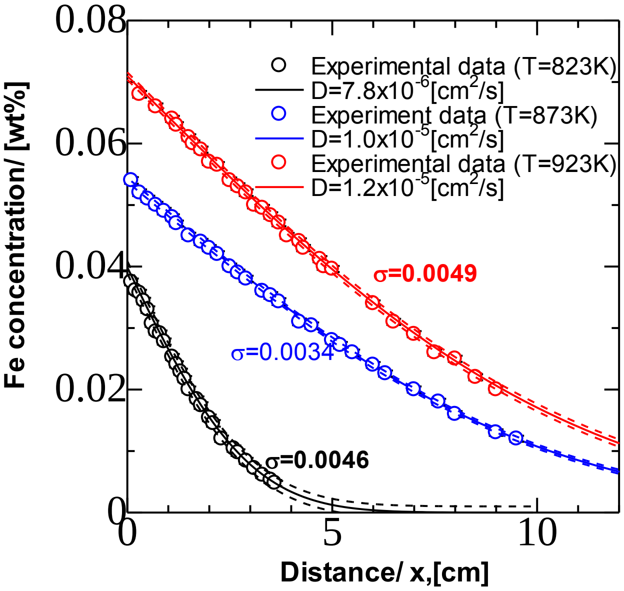

Fig. 3.1 The concentration distribution of diffused Fe in LBE. The black plots denote the results at temperature of 823K, the blue plots denote the results at temperature of 873K and the red plots denote the results at temperature of 923K.

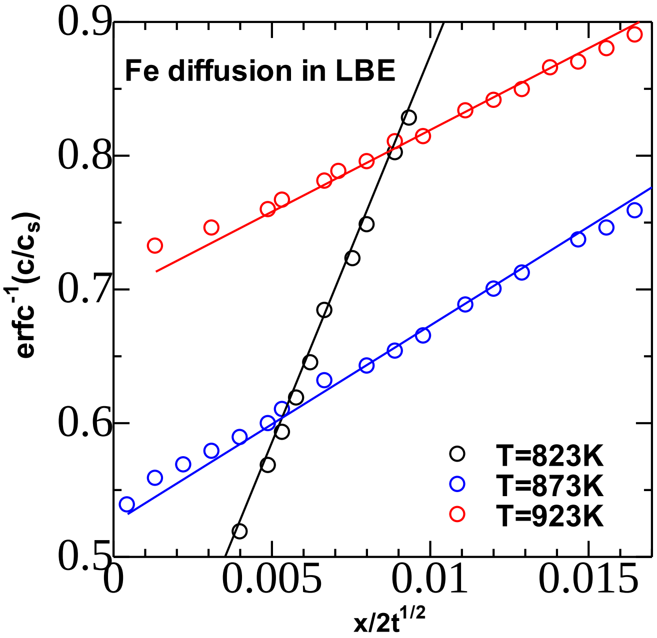

Fig. 3.2 The concentration distribution of diffused Fe in LBE at temperature of 823K, 873K and 923K by using inverse function method of error function.

It is found that the experimental plots are linear and the results of diffusion coefficient versus temperature are obtained and shown in **Table 3.1.** These obtained results show the same values as the results obtained by least squares method. According to the plots, it is denoted that the diffusion coefficient increases with temperature.

Table 3.1 Diffusion coefficients of Fe in liquid LBE

Temperature [K]	**D_{Fe} [cm^2/s]**
823	(7.8±0.01)×10^{-6}
873	(1.0±0.02)×10^{-5}
923	(1.2±0.01)×10^{-5}

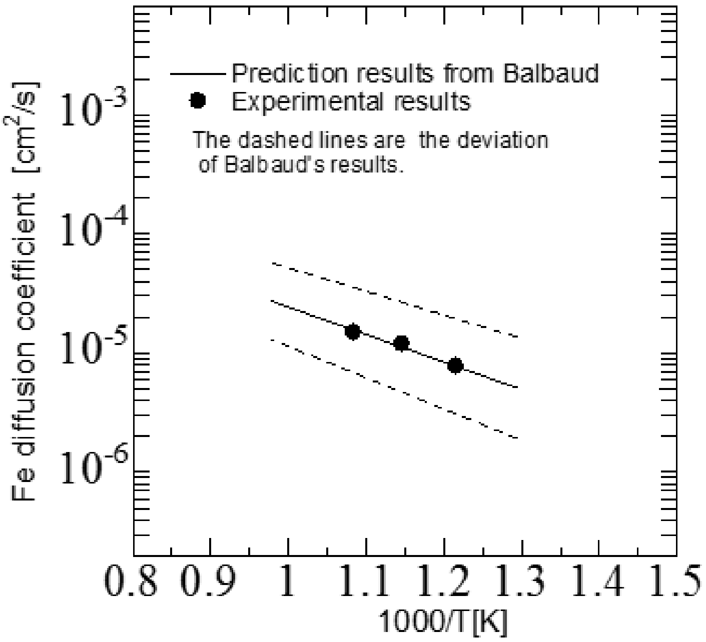

Fig. 3.3 Arrhenius plot of Fe diffusion coefficient in liquid LBE versus 1000/T. The experimental results are compared to the results by Balbaud [1-17].

The experimental results in **figure 3.3** shows in black plots and the solid line is corresponded to the result from Balbaud. The dashed lines are the deviation of Balbaud results. Experimental results of Fe diffusion coefficient are approximately the same as the results predicted by Balbaud, although the latter one shows large deviation. Namely, the speed of Fe transfer in liquid LBE is roughly the same as that in liquid lead, as Balbaud predicted. Thus, the diffusion coefficient of Fe in liquid LBE at temperature from 823K to 923K is obtained as

$$D_{\mathrm{Fe}} = 3.5\times10^{-3}\exp((-4.15\pm0.01)\times10^{4}/\mathrm{R}T)\,. \qquad (3.1)$$

3.3.2. Ni diffusion

The diffused Ni concentration distribution in temperature of 823K LBE at diffusion time of 3.5 hours and 7 hours are given in **figure 3.4** The black plots denote the measurement concentration of Ni at time of 3.5h and the red plots denote the results at time of 7 hours. The solid lines are corresponded to the fitting results based on Fick's second law.

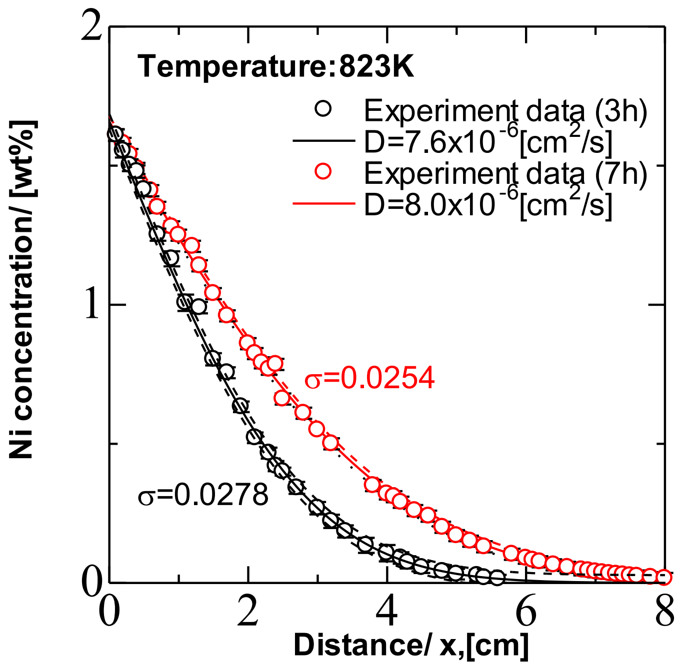

Fig. 3.4 The concentration distribution of diffused Ni in LBE at temperature of 823K.

The diffusion coefficient of Ni at temperature of 823K is obtained as 7.6×10^{-6} cm^2/s when the diffusion time is 3.5 hours, and 8.0×10^{-6} cm^2/s at time of 7.0 hours. The accuracies of the concentration measurement are 0.0278 and 0.0254. The deviations of both diffusion coefficients are $\pm0.25\times10^{-6}$ cm^2/s and $\pm0.01\times10^{-6}$ cm^2/s, respectively. It can be seen that the diffused Ni concentration distribution differed by time, however, the diffusion coefficients are roughly the same. It is presented that the diffusion coefficient is independent on the time. **Table 3.2** shows the obtained diffusion coefficients at all test temperatures.

Table 3.2 Diffusion coefficients of Ni in liquid LBE

Temperature [K]	**D_{Ni} [cm^2/s] (t=3.5h)**	**D_{Ni} [cm^2/s] (t=7.0h)**
773	$(5.6\pm0.02)\times10^{-6}$	$(6.0\pm0.01)\times10^{-6}$
823	$(7.6\pm0.015)\times10^{-6}$	$(8.0\pm0.02)\times10^{-6}$
873	-	$(1.1\pm0.01)\times10^{-5}$
923	$(2.0\pm0.01)\times10^{-5}$	$(1.5\pm0.01)\times10^{-5}$

It is clearly found that the diffusion coefficient of Ni also increases with the temperature and it shows comparable value with the diffusion coefficient of Fe. It is considered that since the radii of Ni and Fe are roughly the same, the diffusion speeds of them show close value. The Ni diffusion coefficient obtained by reducing and without reducing the oxygen concentration in liquid LBE are shown in **Fig 3.5**.

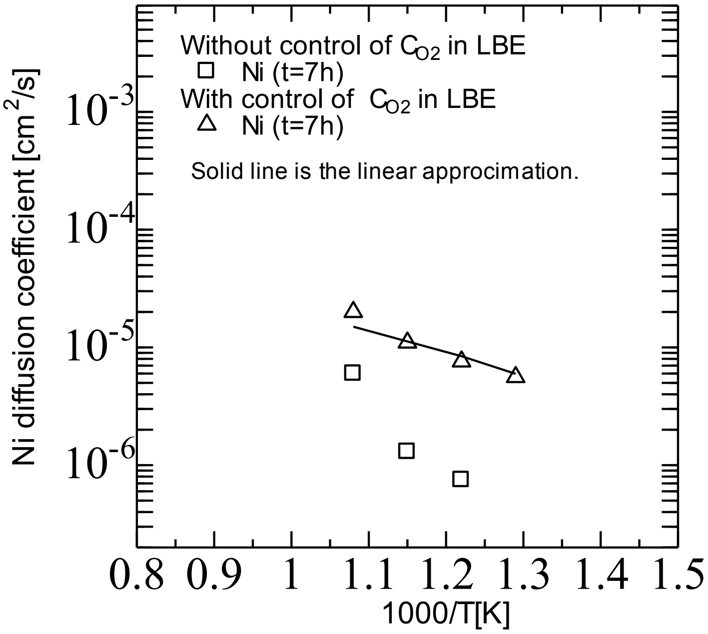

Fig. 3.5 Arrhenius plot of Ni diffusion coefficient versus 1000/T.

The triangle plots are corresponded to the results of Ni diffusing in LBE where the oxygen is eliminated by using a mixture gas of 20%H_2 with argon. The square plots show the results that Ni diffused in LBE where the oxygen concentration is non-reduced preliminarily. The diffusion coefficient becomes one order in magnitude smaller when the oxygen in liquid LBE is without elimination. It is known that the oxygen concentration in as-received LBE is roughly 10^{-3}wt% as described in Chapter 2. At high temperature, the dissolved Ni atoms are oxidized by oxygen in LBE, according to Ellingham diagram shown in **figure 2.2**. Since the diameter of oxide is much larger than Ni atom, the diffusion coefficient becomes smaller. This phenomenon is in consistency with the theory by Stoke Einstein **[A2]**. Ni diffusion coefficient in liquid LBE at temperature from 773K to 923K can be obtained as

$$D_{\mathrm{Ni}} = 1.7 \times 10^{-3} \exp((-3.63 \pm 0.014) \times 10^{4} / \mathrm{R}T)\ . \qquad (3.2)$$

Note that, the value of activation energies of Fe and Ni will be discussed in chapter 6 by comparing to the simulation results.

3.3.3. Results by SEM-EDX analyzation

SEM-EDX [A3] analysis is performed for the solid specimens which obtained from the diffusion experiments. **Figure 3.6** shows the appearance of SEM-EDX instruments which is used for the analysis. The solid specimens which obtained after cooling are cut into10mm per piece. The surface in vertical direction of each solid piece is polished firstly. Then set the polished samples on the sample holder and screw the specimen holder into the chamber of SEM instrument. An example result at diffusion temperature of 823K for Fe and Ni is given in **Fig.3.7 (a)** and **Fig.3.7 (b)**. The analysis spots of Fe and Ni solid pieces are at distance of 11 mm and 10 mm from the top.

Fig. 3.6 Appearance of the SEM-EDX instrument used for microstructure analysis.

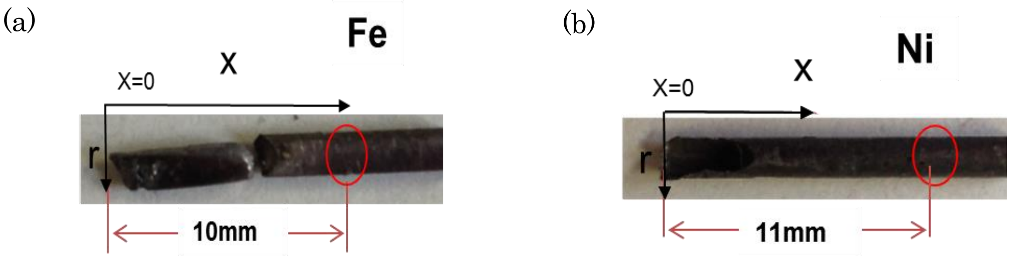

Fig. 3.7 SEM-EDX analysis positions. **(a)** 10mm in x direction from the top for Fe specimen. **(b)** 11mm in x direction from the tope for Ni specimen.

The analysis results are shown in **figure 3.8** and **figure 3.9**, respectively. It is found that there is old and new Ni crystals in case of Ni solid specimen, however, we cannot observe this phenomenon in case of Fe. It is considered that the new Ni crystal is formed during the air cooling procedure after the diffusion and the old Ni crystal is formed during the diffusion. Ni powder dissolved into Ni atom at the contact interface of solid powder and liquid LBE. Then, Ni atom diffused into the liquid LBE. However, it is considered that the aggregation of Ni atoms may happen during the diffusion, since there are several old crystal appeared on the specimen surfaces.

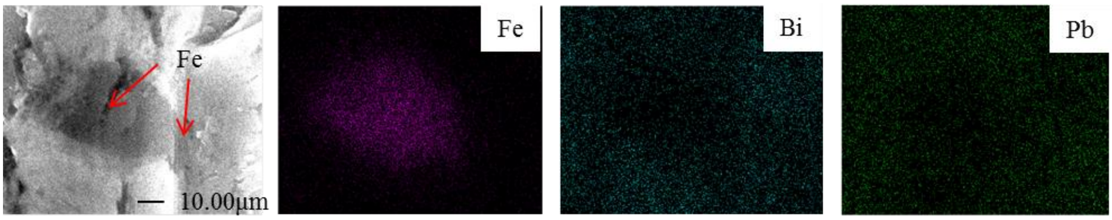

Fig. 3.8 SEM-EDX observation results of Fe diffusion specimen. The first picture is the analysis result by SEM, and others are the analysis results by EDX. The purple area denotes Fe crystals, the blue and green areas denote Bi and Pb crystals.

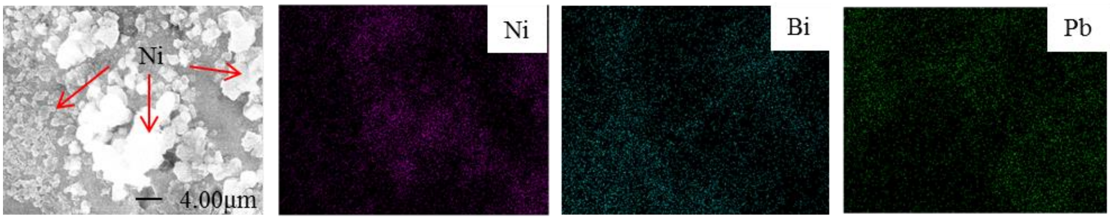

Fig. 3.9 SEM-EDX observation results of Ni diffusion specimen. The first picture is the analysis result by SEM, and others are the analysis results by EDX. The purple area denotes Ni crystals, the blue and green areas denote Bi and Pb crystals.

3.4. Conclusions

The experiments of Fe and Ni diffusion in liquid LBE are carried out by using long capillary method at temperature from 773K to 923K. The diffused Fe and Ni concentrations are measured by ICP-MS and then the diffusion coefficient at each temperature is derived according to Fick's second law. The SEM-EDX analysis are performed for each solid specimen obtained in the diffusion experiment. It is found that:

(1) Fe and Ni diffusion coefficients increase with temperature, however they are independent with the time. Both of the diffusion coefficients show comparable value, although Ni is much more soluble in liquid LBE.

(2) The diffusion coefficient is largely influenced by the oxygen concentration in liquid LBE where the diffusion coefficient becomes one order in magnitude smaller when the oxygen concentration in liquid LBE increases 5 orders in magnitude. This implies that the necessity of controlling the oxygen concentration in liquid LBE.

(3) The diffusion coefficient of Fe shows comparable results with that predicted by Balbaud, that is, the diffusion coefficient of Fe in liquid LBE can be considered as being equal to that of Fe in liquid lead.

(4) The Arrhenius equations of Fe and Ni diffusion coefficient in temperature range of 773-923K are obtained as

$$D_{\mathrm{Fe}} = 3.5\times10^{-3}\exp(-4.15\times10^{4}/\mathrm{R}T),$$
$$D_{\mathrm{Ni}} = 1.7\times10^{-3}\exp(-3.63\times10^{4}/\mathrm{R}T).$$

It is found that the diffusion activation energies of Fe and Ni in liquid LBE, which are the energies for Fe and Ni atoms jump to the vacancy in liquid LBE, are roughly the same, since the radii of both metallic atom are near.

(5) According to the SEM-EDX analysis results, it is considered that Ni atom aggregates during the diffusion. However, this phenomenon cannot be analyzed in case of Fe specimen. In order to make it clear, further studies on this aspect are required.

Chapter 4 Experimental study of iron and nickel diffusion in liquid Pb-17Li

4.1. Introduction

The fundamental study of Fe and Ni diffusion in liquid Pb-17Li are experimentally studied by using long capillary method which has been explained in chapter 2. The concentration measurement of diffused Fe and Ni are analyzed by using ICP-MS. The purpose of this chapter is presented as follows:

(1) To derive the diffusion coefficient of Fe and Ni and clarify the difference of both metals diffusing in liquid Pb-17Li.

(2) To investigate the diffusion characteristics of both metals in liquid Pb-17Li meanwhile, make comparison to those in liquid LBE.

(3) To obtain the temperature-dependent formula of diffusion coefficient using Arrhenius type equation.

4.2. Experimental condition

The temperatures for Fe diffusion are chosen as 573K, 623K, 673K and 723K and the temperatures for Ni diffusion are chosen as 723K, 773K, 823K and 873K by considering the temperature range of practical fusion reactor **[4-1]** and the known temperature range for Fe and Ni solubility as written in chapter 2. The diffusion time is determined as 24 hours.

4.3. Experimental results and discussions

4.3.1. Fe diffusion coefficient

An example result of concentration distribution of Fe at temperature of 723K is shown in **figure 4.1** and the concentration distributions at other temperatures are shown in **appendix 7**. The black plots in the figure denote the Fe concentration at each distance. The solid line is the fitting result according to Fick's second law. The diffusion coefficient is derived as 3.65×10^{-6} cm^2/s, according to Fick's second law. The diffusion coefficients at other temperatures are summarized in **table 4.1**. It is obviously found that the diffusion coefficient increases with temperature. Then, compared to the Fe diffusion coefficient at temperature of 773K obtained by using dissolution flux by Simon **[1-13]**, it can easily predicted that our result will be four orders in magnitude bigger, although we have not performed Fe diffusion in Pb-17Li at temperature of 773K. It is considered that since Simon calculated the diffusion coefficient in forced convection systems and several empirical equations were used to estimate the dissolution flux and thickness of boundary

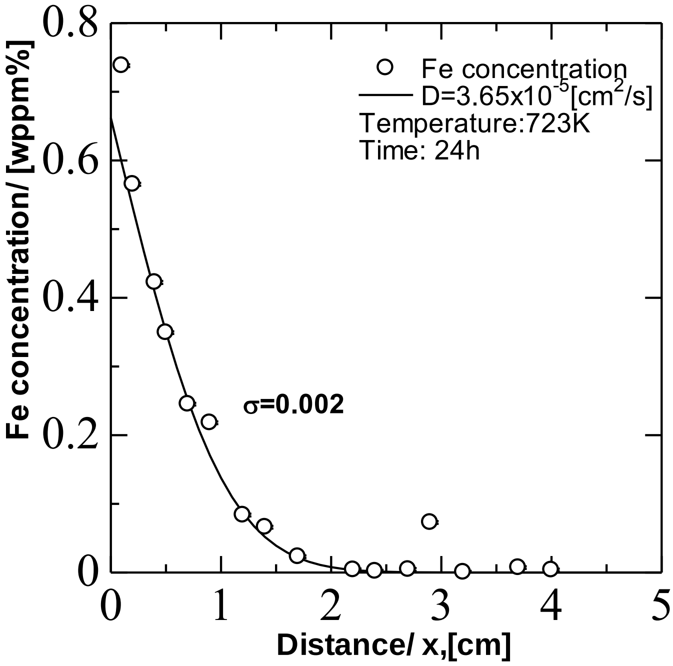

Fig. 4.1 Concentration distribution of diffused Fe in Pb-17Li at temperature of 723K measured by ICP-MS.

layer during the experiment, these may bring large error to the calculation results of diffusion coefficient.

Table 4.1 Diffusion coefficients of Fe in liquid Pb-17Li.

(Diffusion time = 24 hours)

Temperature [K]	**Diffusion coefficient [cm^2/s]**
723	$(3.65\pm0.01)\times10^{-5}$
773	$(4.60\pm0.01)\times10^{-5}$
823	$(6.23\pm0.02)\times10^{-5}$
873	$(7.8\pm0.01)\times10^{-5}$

Arrhenius plot of the obtained Fe diffusion coefficient versus 1000/T is shown in **figure 4.2**. The circle plots in the figure denote the experimental results and the solid red line is the linear approximation. The triangle plots are corresponded to the experimental results Fe diffusion coefficient in liquid LBE, and the solid and dashed black lines show Fe diffusion coefficient in liquid lead **[4-2]**. It is found that Fe diffusion coefficient in liquid lead, LBE and Pb-17Li are close to each other. Arrhenius equation of Fe diffusion coefficient in liquid Pb-17Li in temperature range of 573-723K can be obtained as

$$D_{\mathrm{Fe}} = 4.5\times10^{-5}\exp((-1.58\pm0.021)\times10^{4}/\mathrm{R}T)\ . \qquad (4.1)$$

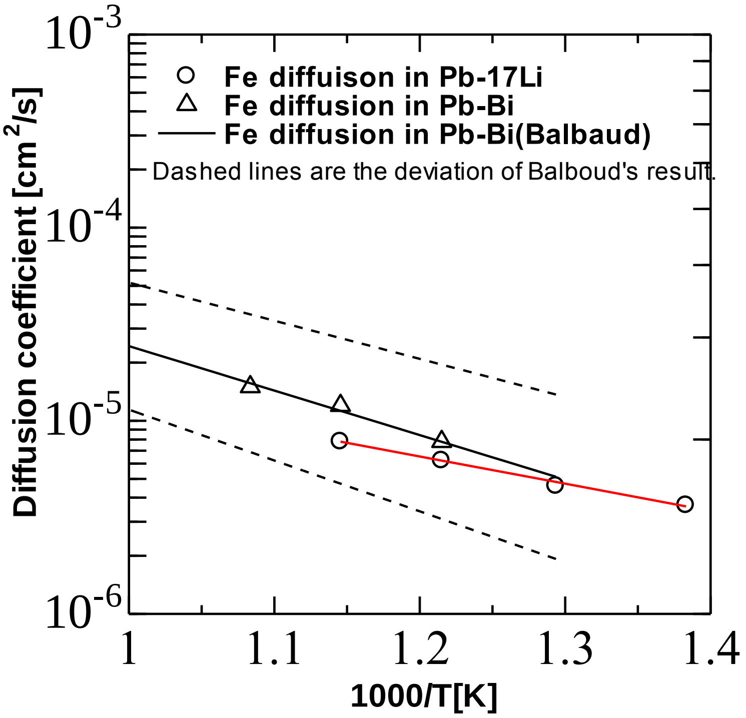

Fig. 4.2 Arrhenius plots of Fe diffusion coefficient in liquid Pb-17Li versus 1000/T. The results are compared to the experimental results of Fe diffusion coefficients in liquid lead by Balbaud **[1-15]** and those in liquid LBE described in Chapter 3.

4.3.2. Ni diffusion coefficient

The concentration distribution of Ni in Pb-17Li at temperature of 723K measured by ICP-MS shows in **figure 4.3**. The measurement deviation is 0.005 and the concentrations of Ni at distance less than 1mm show extremely large values. It is because the Ni powders haven’t completely dissolved into the liquid Pb-17Li during the experiment and there are some powders left on the top of the solid specimen, as considered. The diffusion coefficient is derived without those large values, and it is obtained as $3.20 \pm 0.1 \times 10^{-5}$ cm^2/s. **Table 4.2** summarizes all the diffusion coefficients at different temperatures.

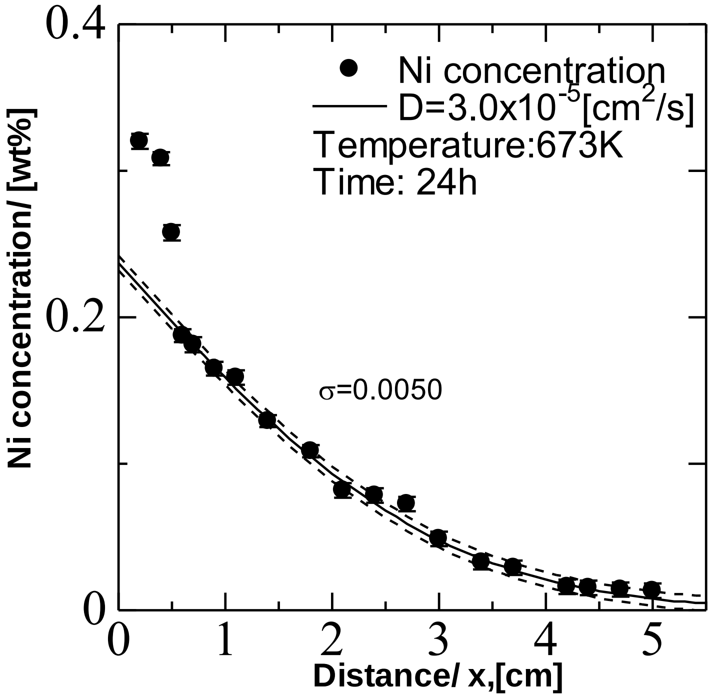

Fig. 4.3 Concentration distribution of diffused Ni in Pb-17Li measured by ICP-MS. The diffusion temperature is 673K.

Table 4.2 Diffusion coefficients of Ni in liquid Pb-17Li.
(Diffusion time = 24 hours)

Temperature [K]	Diffusion coefficient [cm^2/s]
573	$(2.70\pm0.015)\times10^{-5}$
623	$(2.85\pm0.01)\times10^{-5}$
673	$(3.0\pm0.01)\times10^{-5}$
823	$(3.39\pm0.02)\times10^{-5}$

Figure 4.4 shows the Arrhenius plot of Ni diffusion coefficient versus 1000/T. The triangle plots in the figure denote Ni diffusion coefficients. The solid line shows the linear approximation. The function of the linear approximation can be written following Arrhenius equation as:

$$D_{\mathrm{Ni}} = 7.37 \times 10^{-5} \exp((-1.06 \pm 0.013) \times 10^{4} / \mathrm{R}T).$$

It is found the Fe and Ni diffusion coefficients show roughly the same value at temperature of 723K. According to **Fig. 4.4**, it is supposed that the diffusion coefficient of Fe is smaller than that of Ni at temperature lower than 723K and the diffusion coefficient of Ni is higher than that of Fe at temperature higher than 723K.

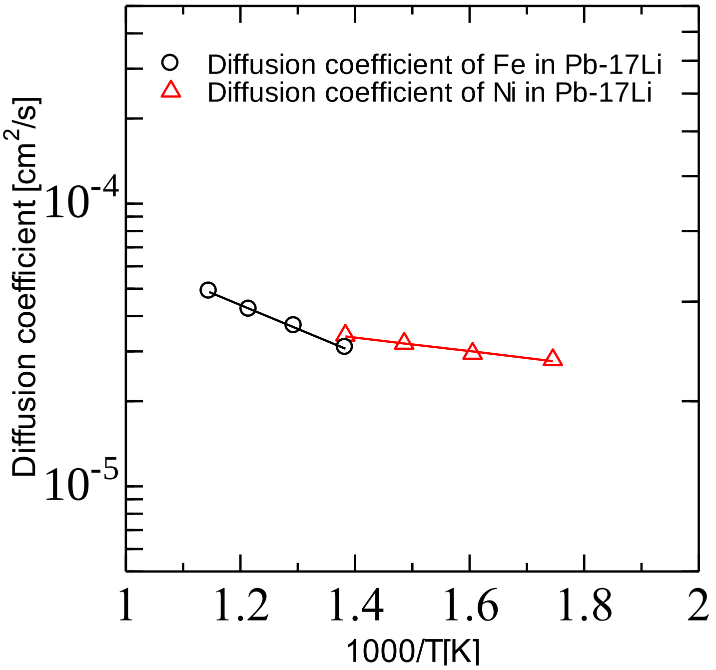

Fig. 4.4 Arrhenius plots of Ni diffusion in liquid Pb-17Li. The results are compared to Fe diffusion coefficients in liquid Pb-17Li.

4.4. Conclusions

The experiments of Fe and Ni diffusion in liquid Pb-17Li are carried out by using long capillary method. The diffused Fe and Ni concentrations are measured by ICP-MS and then the diffusion coefficient at each temperature is derived according to Fick’s second law. It is found that:

(1) Fe and Ni diffusion coefficients increase with temperature, and Fe and Ni diffusion coefficients at temperature of 723K show roughly the same value. It is assumed that the diffusion coefficient of Fe is smaller than that of Ni at temperature lower than 723K and the diffusion coefficient of Ni is smaller than that of Fe at temperature higher than 723K

(2) The diffusion coefficient Fe in liquid Pb-17Li is close to that in liquid lead and LBE. It is considered that the diffusion speed may be largely dependent on the lead.

(3) The Arrhenius equations of Fe diffusion coefficient in temperature range of 573-723K and that of at temperature of 773K to 923K are obtained as:

$$D_{\mathrm{Fe}} = 4.5\times10^{-5}\exp(-1.58\times10^{4} / \mathrm{R}T),$$

$$D_{\mathrm{Ni}} = 7.37\times10^{-5}\exp(-4.66\times10^{3} / \mathrm{R}T).$$

References

[4-1] B. A. Pint, K. A. Unocic, J. Nucl. Mater. 442 (2013) 5572-5575.

Chapter 5 Computational method —Molecular dynamics simulation

5.1. Introduction

Molecular dynamics (MD) simulation act as a bridge between microscopic length and time scales and the macroscopic world of the laboratory. It is a useful tool that can provide insights into the atomic-scale interactions and mechanism which control the physical phenomena. There are two main kinds of molecular dynamics (MD) simulations – classical MD simulation **[5-1]** and quantum mechanical MD simulation so-called ab-initio MD simulation, AIMD for short **[5-2]**. The classical MD simulation follow the laws of classical mechanism and most notably Newton’s law. The forces working on the atomic nuclei are obtained from empirical potential energy expressions and the electrons are implicit. On the other hand, ab-initio MD (AIMD) simulation uses a quantum mechanical description of the electrons which is called density functional theory (DFT) to calculate the forces working on the atomic nuclei. Due to the time-cost of treating the electronic degrees of freedom during the calculation, the AIMD is more computational costly than the classical MD simulation although it has higher accuracy. This implies that AIMD simulation is limited to use for a small system and short time, although it can simulate the bond forming and breaking among atoms. In present study, Fe and Ni diffusion in liquid lead alloys will be performed and the accurate value of diffusion coefficients are hoped to obtained, so that a large simulation system with long simulation time is required. Therefore, the classical MD simulation is chosen in present study.

The classical MD simulation consists of the numerical, step-by-step, solution of the classical equations of motion, which for a simple atomic system constituted by N atoms can be written as **[5-3]**

$$f_i = m_i \boldsymbol{a_i} . \tag{5.1}$$

m_i is the atom mass, $\boldsymbol{a_i}$ is its acceleration which can be obtained as

$$\boldsymbol{a_i} = \frac{d^2 r_i}{dt^2} , \tag{5.2}$$

and f_i is the force acting upon i atom due to the interactions with other atoms. The force

f_i can be derived from a potential energy E (r^N), where $r^N = (r_1, r_2, \ldots r_N)$ represents the complete set of 3N atomic coordinates, as following equation.

$$f_i = -\frac{\partial}{\partial r_i} E(r^N)\,. \tag{5.3}$$

The simplest expression of E is to write it as a sum of pairwise interactions:

$$E(r^N) = \sum_i \sum_{j>i} \phi(\left|r_i - r_j\right|)\,. \tag{5.4}$$

The clause $j > i$ in the second summation has the purpose of considering each atom pair only once. In the past, most potentials were constituted by pairwise interactions, but it is no longer that case now. It has been realized that the two-body approximation, i.g. Lennard-Jones potential [**A4**], is very poor for many relevant systems, such as metals and semiconductors **[5-4]**. Various kinds of many-body potentials are now commonly used in condensed matter simulation and the embedded atom model (EAM) **[5-5, 5-6]** is one of the methods that can be used to represent the many-body interaction with the liquid metal.Thus, in present study, the EAM is used to represent the many body interaction within the liquid LBE and Pb-17Li and the purposes of this chapter are presented as follows:

(1) To validate the EAM models of liquid LBE and Pb-17Li by computing the density, volumetric thermal expansion, heat capacity and viscosity of them by classical MD simulation and then comparing the simulation results to the experimental results;

(2) To represent and develop the cross pair interactions of Fe-Pb, Ni-Pb, Fe-Bi, Ni-Bi, Fe-Li and Ni-Li within the liquid alloys, where since the imposed density function of Pb and Bi differs from that of Fe and Ni, the ab-initio molecular dynamics is used to calibrate the validity of the pair interaction

5.2. Embedded atom model

The EAM is a semi-empirical model rooted in density-functional theory using concepts given by Stott and Zaremba **[5-7]**. It is a commonly used representation for the energy that overcomes the volume dependent limitation of pair-potentials by adding a term for the energy to embed an atom in the background electron density of its neighbors. The basic function of total potential energy *E* of a system consisting of N atoms can be written as **[5-5, 5-6]**

$$E = \sum_{i=1}^{N} \left[F\left(\rho_i\right) + \frac{1}{2} \sum_{j \neq i} \Phi\left(r_{ij}\right) \right], \qquad (5.5)$$

$$\rho_i = \sum_{j} f\left(r_{ij}\right) \qquad (5.6)$$

where ρ_i is the effective electron density at atom *i* due to all other atoms, $f(r_{ij})$ is the electron density at atom *i* due to atom *j* as a function of a distance r_{ij} between them, $F(\rho_i)$ is the energy required to embed atom *i* in an electron density ρ_i, and $\Phi(r_{ij})$ is a two-body potential between atoms *i* and *j*. According to the **Eq 5.5**, it is obviously known that the embedding potential is not simply like the summation of pairwise interaction between two bodies.

For an alloy model, an embedding function $F(\rho_i)$ and an atomic electron-density function $f(r_{ij})$ must be specified for each atomic species, and a two-body potential $\Phi(r)$ specified for each possible combination of atomic species. Since the electron density at any location is taken as a linear superposition of atomic electron densities, and since the embedding energy is assumed to be independent of the source of the electron density, both $F(\rho_i)$ and $f(r_{ij})$ functions can be taken directly from monatomic models. For a binary alloy with a- and b-type atoms, the two-body potential $\Phi^{ab}(r)$ can be calculated as **[5-8]**

$$\Phi^{ab}(r) = \frac{1}{2}\left(\frac{f^{b}(r)}{f^{a}(r)} \Phi^{aa}(r) + \frac{f^{a}(r)}{f^{b}(r)} \Phi^{bb}(r) \right), \qquad (5.7)$$

where Φ^{aa} and Φ^{bb} are given by the monatomic models. The two-body potential, so-called combination rule, is obtained by average the potentials of two different monatomic models using electron density functions as a relative ratio. The two-body potentials of Φ^{ab} and Φ^{ba} are equal.

Meanwhile, the simulation of binary or many body systems sometimes requires the modification of the EAM scheme **[5-9]**. If pure components possess different average effective electron densities, it is desirable to preliminarily normalize the parameter $f(r_{ij})$, so as to equalize the density of both components **[5-10, 5-11]**. The modification functions are shown as following equations and s is the modification factor.

$$f^*\left(r_{ij}\right) = sf\left(r_{ij}\right), \tag{5.8}$$

$$\rho_i^* = \sum f^*\left(r_{ij}\right), \tag{5.9}$$

$$F^*\left(\rho^*_i\right) = F^*\left(\frac{\rho^*_i}{s}\right). \tag{5.10}$$

Besides, there is another modification method that a term linear in the electron density is added to or subtracted from the embedding function **[5-11, 5-8]**.

$$F^*\left(\rho_{ij}\right) \rightarrow F\left(\rho_{ij}\right) + s\rho, \tag{5.11}$$

$$\Phi^*(r_{ij}) \rightarrow \Phi(r_{ij}) - 2s\rho, \tag{5.12}$$

It is noted that the total potential energy E of the monatomic EAM model is invariant after the modification for either case. There is no physical requirement for this invariance, but it yields better results in the calculation and this methodology has been successfully applied in Si-Ge alloy calculations **[5-12]**.

5.2.1. Parameterization of Pb, Bi and Li

The parametrizations for pure liquid Pb, Bi and Li are developed by Belashchenko **[5-10, 5-13, 5-14]** and the embedding energy function, density function and pair potential function are denoted as following equations. The embedding energy functions are written as

$$F(\rho) = \mathrm{a}_0 + \mathrm{c}_0(\rho - \rho_0)^2 , \quad (\rho_5 \le \rho \le \rho_6) , \tag{5.13}$$

$$F(\rho) = \mathrm{a}_i + \mathrm{b}_i(\rho - \rho_{i+1}) + \mathrm{c}_i(\rho - \rho_{i+1})^2 , \quad (\rho_i \le \rho \le \rho_{i+1}, \mathrm{i} = 1, 2, 3, 4) , \tag{5.14}$$

$$F(\rho) = \mathrm{a}_5 + \mathrm{b}_5(\rho - \rho_1) + \mathrm{c}_5(\rho - \rho_1)^2 , \quad (\rho \le \rho_1) . \tag{5.15}$$

The parameters of a_0- a_5, b_1-b_5, c_0-c_5, ρ_0-ρ_6 are determined by matching the properties of models with the experimental data. **Table 5.1**, **5.2** and **5.3** show the detailed values of those parameters for embedding energy calculation of Pb, Bi and Li, respectively.

Table 5.1. Parameters for embedding energy calculation of Pb

Subscript	**a [eV]**	**b [eV]**	**c [eV]**	**P**
0	-1.57509	-	1.7622	1.00
1	-1.563872	-0.224360	0.402	0.90
2	-1.537416	-0.304760	0.475	0.81
3	-1.502190	-0.399760	3.407	0.77
4	-1.428144	-1.081160	0.28	0.71
5	-1.053501	-1.260360	0.0	0.46
6	-	-	-	1.40

Table 5.2 Parameters for embedding energy calculation of Bi

Subscript	**a [eV]**	**b [eV]**	**c [eV]**	**P**
0	-1.57509	-	1.7622	1.00
1	-1.563872	-0.224360	0.402	0.90
2	-1.537416	-0.304760	0.475	0.80
3	-1.502190	-0.399760	3.407	0.70
4	-1.428144	-1.081160	0.28	0.60
5	-1.053501	-1.260360	0.0	0.28
6	-	-	-	1.40

Table 5.3 Parameters for embedding energy calculation of Li

Subscript	a [eV]	b [eV]	c [eV]	P
0	-0.8948	-	0.0326	1.00
1	-0.894474	-0.006520	1.700	0.900
2	-0.887963	-0.210520	-1.020	0.840
3	-0.878482	0.075080	1.750	0.700
4	-0.850369	-0.449920	-1.000	0.550
5	-0.800385	-0.049920	11.0	0.350
6	-	-	-	1.10

Figure 5.1, **5.2** and **5.3** show the calculation results of the embedding energies of Pb, Bi and Li, respectively.

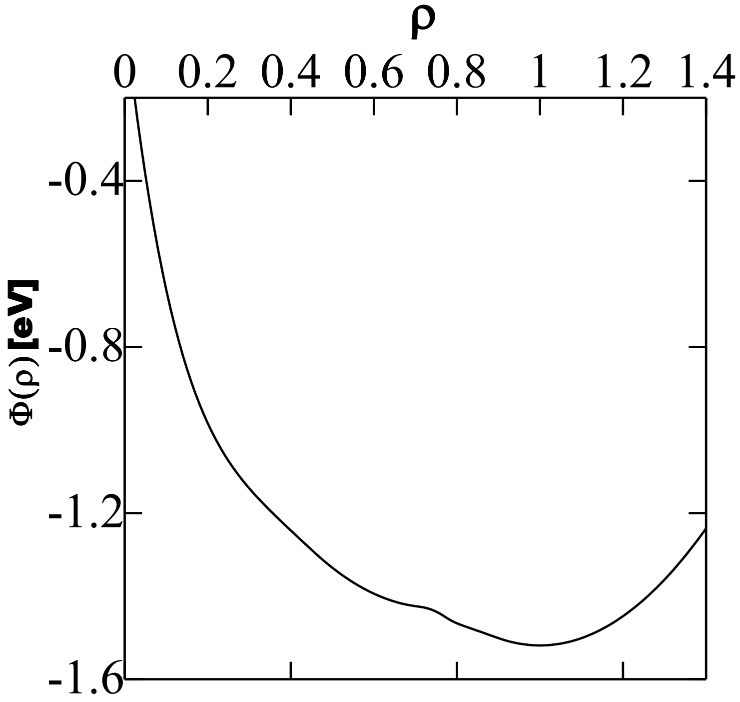

Fig. 5.1. Embedding energy of Pb calculated by using Belashchenko’s parameters.

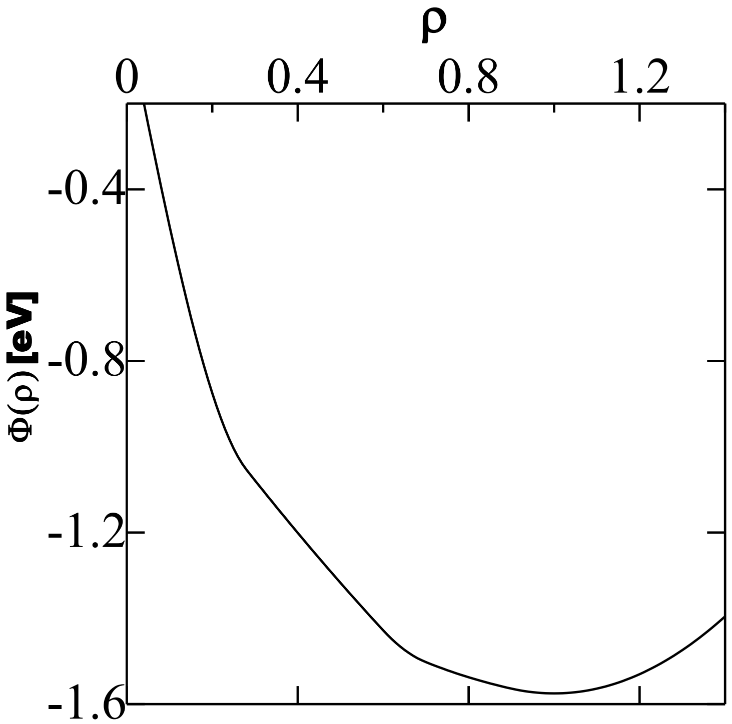

Fig. 5.2 Embedding energy of Bi calculated by using Belashchenko's parameters.

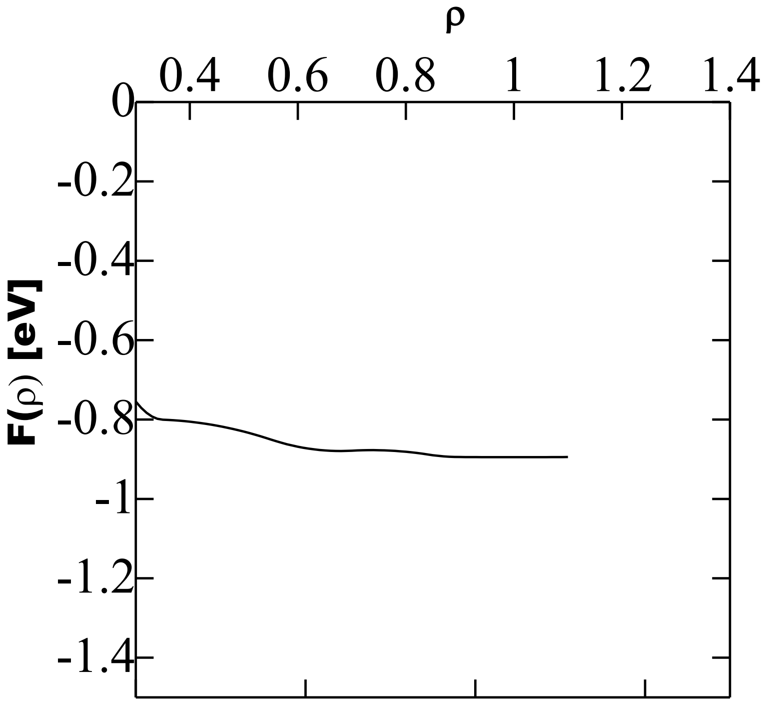

Fig. 5.3. Embedding energy of Li calculated by using Belashchenko's parameters.

The electron density function f is expressed as

$$f(r) = p_1 \exp\left(-p_2 r\right), \tag{5.16}$$

and the values of p_1, p_2 for Pb, Bi and Li are shown in **Table 5.4**. The plots of calculation results are represented in **figures 5.4**, **5.5** and **5.6**, respectively.

Table 5.4 p_1, p_2 for electron density calculation of Pb, Bi and Li

	p_1 [Å^{-1}]	p_2 [Å^{-1}]
Pb	5.1531	1.2200
Bi	5.28909	1.200
Li	3.0511	1.2200

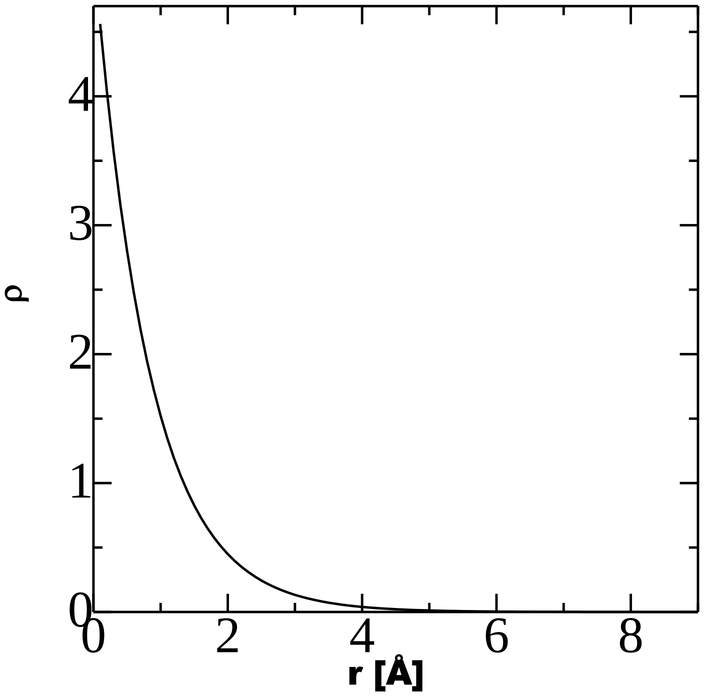

Fig. 5.4 Electron density of Pb by using Belashchenko's parameters.

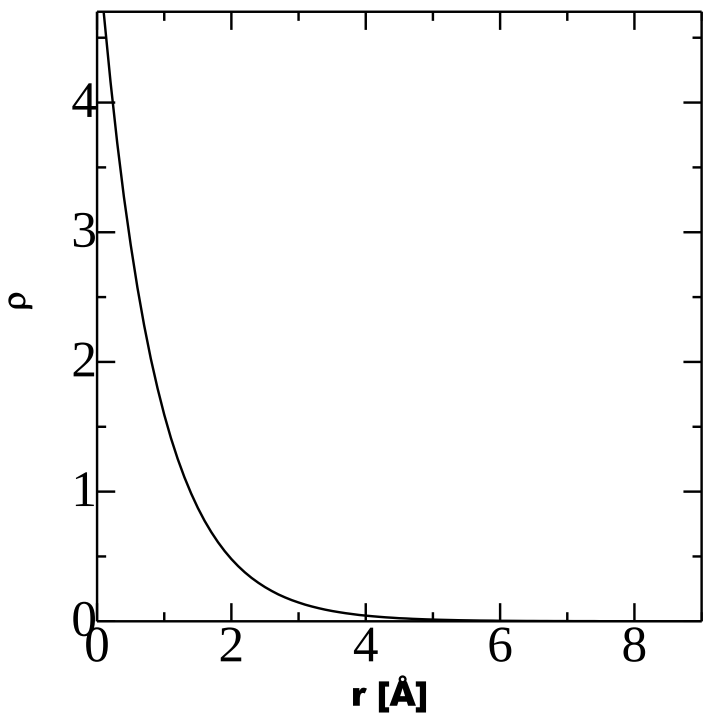

Fig. 5.5 Electron density of Bi by using Belashchenko's parameters.

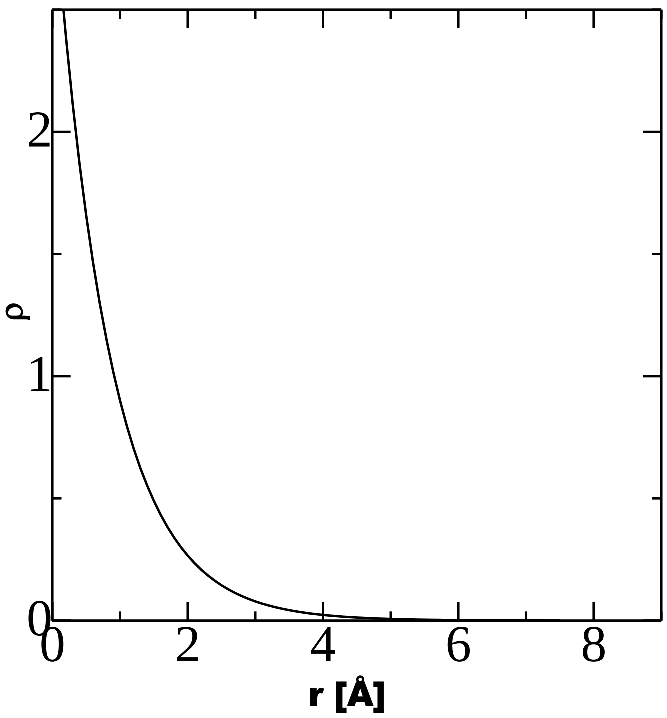

Fig. 5.6 Electron density of Li by using Belashchenko's parameters.

Accordingly, the cut off distance for liquid Pb and Bi simulations were 9.01 Å and 9.05 Å in Belashchenko's original research work. However, by considering the consistency and reproducibility of the liquid binary models, the bigger cut off distance of 9.05 Å is chosen as a global cut off distance not only for Pb, Bi and Li simulations, but also for Fe and Ni simulations which are explained as below. The Schommers algorithm **[5-15, 5-16]** was used to calculate the pair potential for Pb, Bi and Li, however, the functions for Pb and Bi differ from those for Li. The segment on the $0<r<9.05$ Å was divided into four intervals with division points at $r_i=2.60$, 4.60, 7.60 and 9.05 Å ($i=0$, 1, 2, 3) for modeling Pb. The segment in distance was divided into six intervals with division points at $r_i=2.50$, 3.00, 3.50, 4.00, 6.50 and 9.05 Å ($i=0$, 1, 2, 3, 4, 5) for modeling Bi. The pair potential function Φ [eV] at distance of $r > r_0$ is given by equation:

$$\Phi(r) = \sum_{i=1}^{n}\sum_{m=0}^{k} a_{m\ i}(r - r_{i+1})^{m} H(r_i, r_{i+1}),\ (r > r_0)\,. \qquad (5.17)$$

where r is the distance between two particles, i is the interval number along the axis of distance, a_{mi} which are shown in **table 5.5** and **table 5.6** are the coefficients of the expansion into a series and the $H(r_i, r_{i+1})$ function is 1 in the $r_i \le r \le r_{i+1}$ interval and zero otherwise.

Table 5.5 Coefficient of expansion into a series for calculation of Pb pair potential

a_{mi}	1	2	3
0	-0.60930526815355E-02	-0.4415144212544E-02	0.00000000000000
1	-0.13621575199068E-01	-0.61437641270459E-02	0.00000000000000
2	-0.45660788997838E-01	-0.10177246335680	0.16082816702565
3	0.11230757774433	-0.25452335322626	0.13772915239242E+01
4	0.36172101010484	-0.32596219577719	0.46100352215597E+01
5	0.23710940431335	-0.23344635267770	0.77406092052939E+01
6	-0.14300929222822	-0.92940354296357E-01	0.69328765962609E+01
7	-0.18657853386373	-0.19153257528366E-01	0.31673915035111E+01
8	-0.44652604375371E-01	-0.15905291914747E-02	0.58055948305632

Table 5.6 Coefficient of expansion into a series for calculation of Bi pair potential

a_{mi}	1	2	3	4	5
0	0.23032123222947E-01	-0.58089114725590E-01	-0.38583852350712E-01	-0.63335783779621E-02	0.00000000000000
1	-0.26618006825447	0.45752499252558E-01	0.78495843335986E-02	0.10303066810593E-02	0.00000000000000
2	-0.62050552158296E+01	0.68828017622705	-0.10112647441308E+01	0.42480747246449E-01	-0.91599761109836E-02
3	-0.92775522451735E+02	0.22976325825531E+01	-0.10668364762145E+02	0.81690273704111E-01	-0.29685481254410E-01
4	-0.44789947487489E+03	0.49502135238428E+01	-0.43008987321300E+02	0.40740331582690E-01	-0.29950729803211E-01
5	-0.87044414901813E+03	-0.72236788574834	-0.73991049540494E+02	0.59046334275219E-02	-0.11676661892341E-01
6	-0.55341290239556E+03	-0.72211727467775E+01	-0.46109980129960E+02	-0.13747612449246E-03	-0.15697393361539E-02

The pair potential function for Li at distance of 2.45 Å $<r<$7.50 Å is given by

$$\phi(r) = a_0 \times 10^1 + \frac{a_1 \times 10^2}{r} + \frac{a_2 \times 10^3}{r^2} + \frac{a_3 \times 10^3}{r^3} + \frac{a_4 \times 10^4}{r^4} + \frac{a_5 \times 10^3}{r^5}, \qquad (5.18)$$

and the values of a_i are denoted in table 5.7. At $r \leq 2.45$ Å , the potential is expressed as

$$\phi(r) = 0.252868 + 0.15252(2.45 - r) + 0.38\{\exp[1.96(2.45 - r)] - 1\}. \qquad (5.19)$$

Table 5.7 Parameters for the calculation of Li pair potential

a_i	a_0	a_1	a_2	a_3	a_4	a_5
	-0.161539351212	0.329193195820	-0.245830404172	0.840217873656	-0.136938125679	0.905623694715

The calculation results of the pair potential of Pb, Bi and Li are shown in **figure 5.7**, **5.8** and **5.9**.

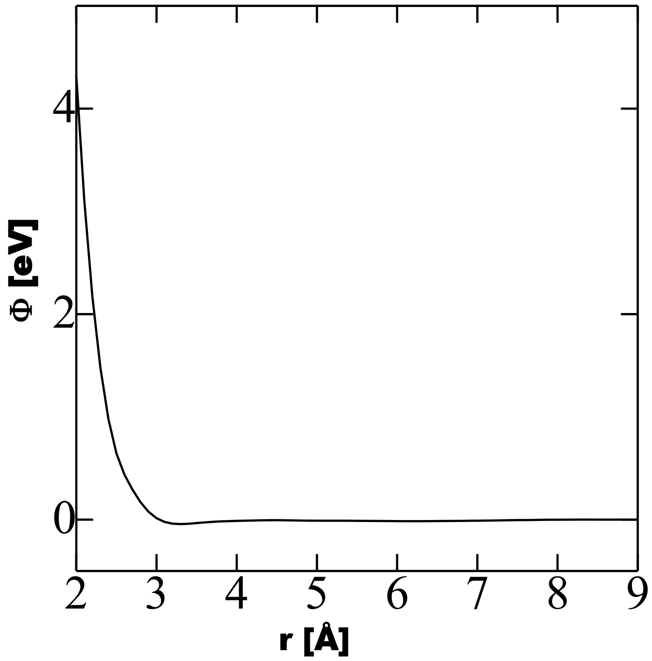

Fig. 5.7 Pair potential of Pb by using Belashchenko’s parameters**.**

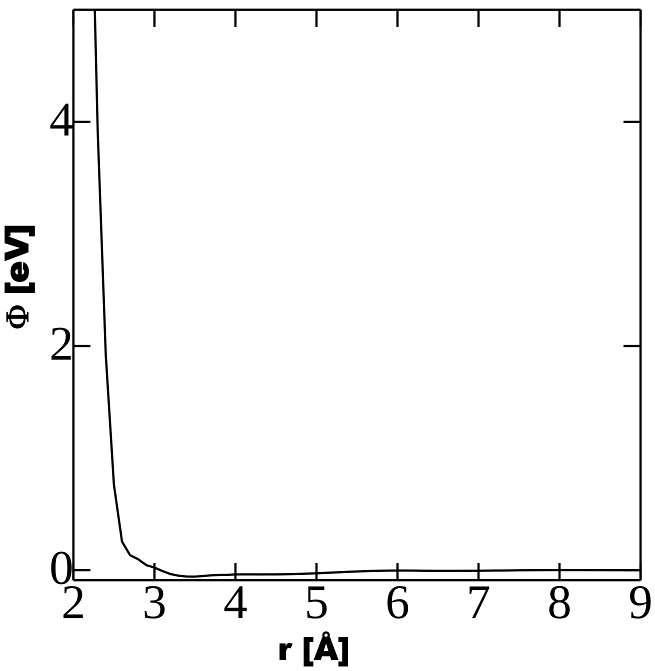

Fig. 5.8 Pair potential of Bi by using Belashchenko's parameters.

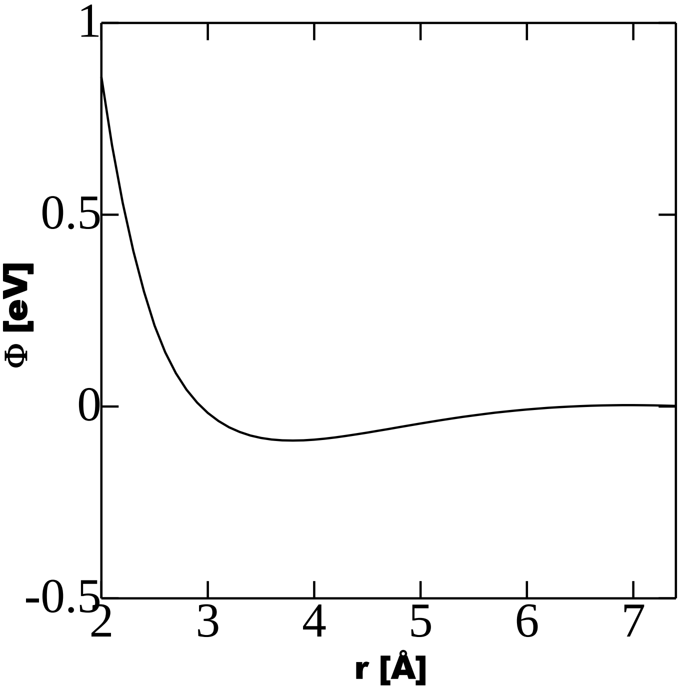

Fig. 5.9 Pair potential of Li by using Belashchenko's parameters.

5.2.2. Parameterization of Ni and Fe

The embedding energy function, the electron density function and the pair potential function of Fe and Ni which are used in this study are developed by Zhou and Johnson et al **[5-17]**. The embedding energy functions are given by:

$$F(\rho) = \sum_{i=0}^{3} F_{ni} \left(\frac{\rho}{\rho_n} \right)^i , \quad (\rho \le \rho_n, \rho_n = 0.85\rho_e), \tag{5.20}$$

$$F(\rho) = \sum_{i=0}^{3} F_i \left(\frac{\rho}{\rho_e} - 1 \right)^i , \quad (\rho_n \le \rho \le \rho_0, \rho_0 = 1.15\rho_e), \tag{5.21}$$

$$F(\rho) = F_e \left[1 - \ln \left(\frac{\rho}{\rho_s} \right)^\eta \right] \left(\frac{\rho}{\rho_s} \right)^\eta , \quad (\rho_0 \le \rho). \tag{5.22}$$

The electron density function *f* is given as:

$$f(r) = \frac{f_e \exp\left[-\beta (r / r_e - 1) \right]}{1 + (r / r_e - \lambda)^{20}} . \tag{5.23}$$

The pair potential function φ is written as:

$$\phi(r) = \frac{A \exp\left[-\alpha (r / r_e - 1) \right]}{1 + (r / r_e - \kappa)^{20}} - \frac{B \exp\left[-\beta (r / r_e - 1) \right]}{1 + (r / r_e - \lambda)^{20}} . \tag{5.24}$$

The detailed parameters in those functions for Fe and Ni are shown in **Table 5.8**.

Table 5.8 Parameters for calculation of Fe and Ni EAM potential

	r_e	f_e	ρ_e	ρ_s	α	B	A
Fe	2.481987	1.885957	20.041463	20.041463	9.818270	5.236411	0.392811
Ni	2.488746	2.007018	27.562015	27.930410	8.383453	4.471175	0.429046
	B	K	λ	F_{n0}	F_{n1}	F_{n2}	F_{n3}
Fe	0.646243	0.170306	0.340613	-2.534992	-0.05960	0.193065	-2.28232
Ni	0.633531	0.443599	0.820658	-2.693513	-0.07644	0.241442	-2.37562
	F_0	F_1	F_2	F_3	η	F_e	-
Fe	-2.54	0	0.200269	-0.148770	0.391750	-2.53994	-
Ni	-2.70	0	0.265390	-0.152856	0.469000	-2.69948	-

However, it is found that the average effective electron density developed by Zhou et al. is significantly different from that by Belashchenko, according to the comparison of electron density and embedding energy plots of Pb developed by both groups as shown in **Figure 5.10** and **5.11**. The black solid lines in both figures denote the calculation results by using Belashchenko's parameters and the red solid lines are corresponded to the results by using the parameters from Zhou et al. Thus, according to **Eq**. **5.8, 5.9** and **5.10**, the modification of the electron density by Zhou et al is performed, as to keep the modeling system consistent. Then, validity of the modification factor is verified with ab-initio MD (AIMD) simulation.

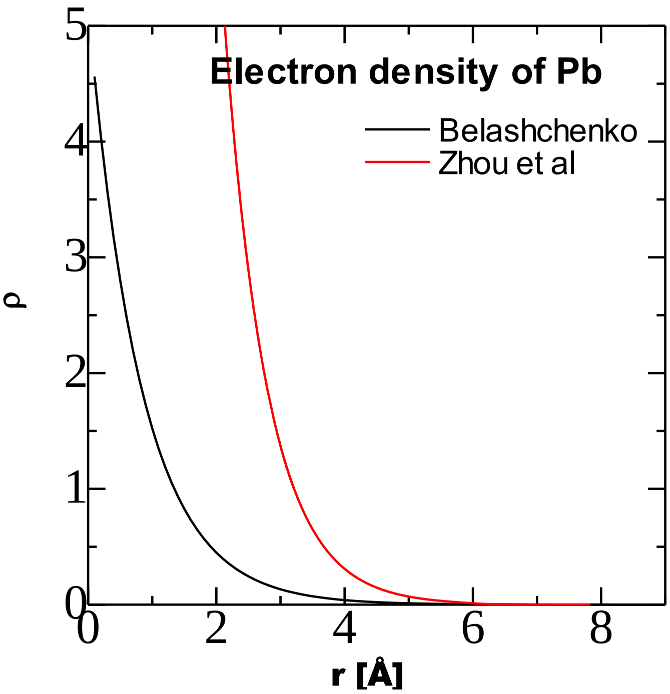

Fig. 5.10 Electron density of Pb calculated by using Belashchenko's parameters compared to the result calculated by using the parameters from Zhou et al.

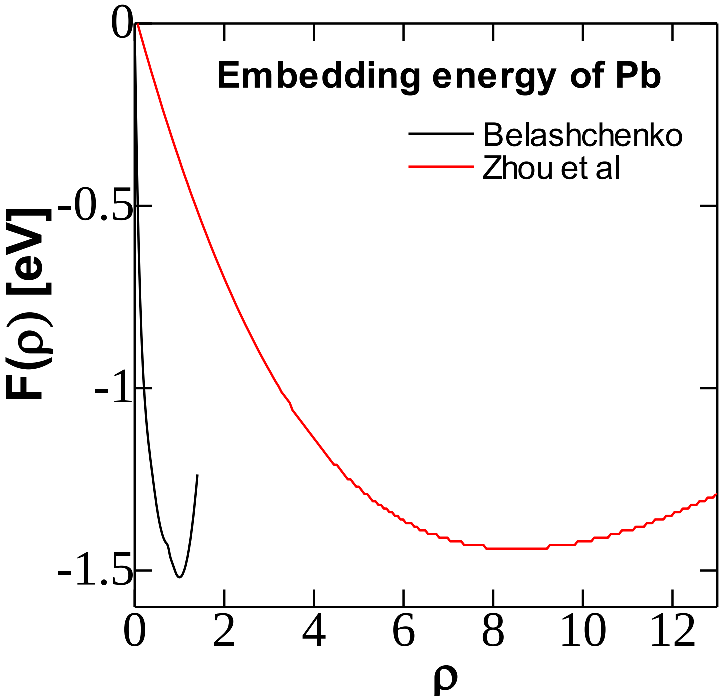

Fig. 5.11 Embedding energy of Pb calculated by using Belashchenko's parameters compared to the result calculated by using the parameters from Zhou et al.

5.2.3. Modification factor calibrated by AIMD simulation

Firstly, the modification factor is determined by considering the pair distribution function **[A5]** of pure Pb computed by Belashchenko **[5-16]** as shown in **figure 5.12**. The simulation result of the pair distribution function is shown as solid line and the plots are corresponded to the diffraction experimental results **[5-18]**. Due to no pair interaction within the distance of 3 angstrom, it implies that the electron density beyond 3 angstrom largely influences the atomic pair interaction. Thus, the electron density of Pb developed by Zhou as shown in **figure 5.10** is normalized to the same value developed by Belashchenko at distance of 3 angstrom. The modification factor is 0.097 and **Fig 5.13** and **Fig. 5.14** show the electron density and embedding energy of Pb by Zhou after modification.

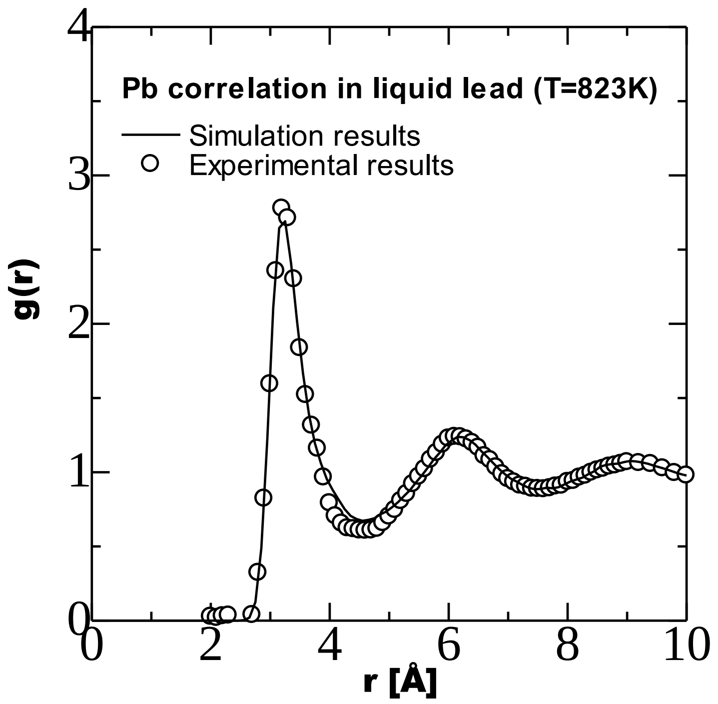

Fig. 5.12 The pair distribution function of liquid lead at temperature of 823K compared to the diffraction data.

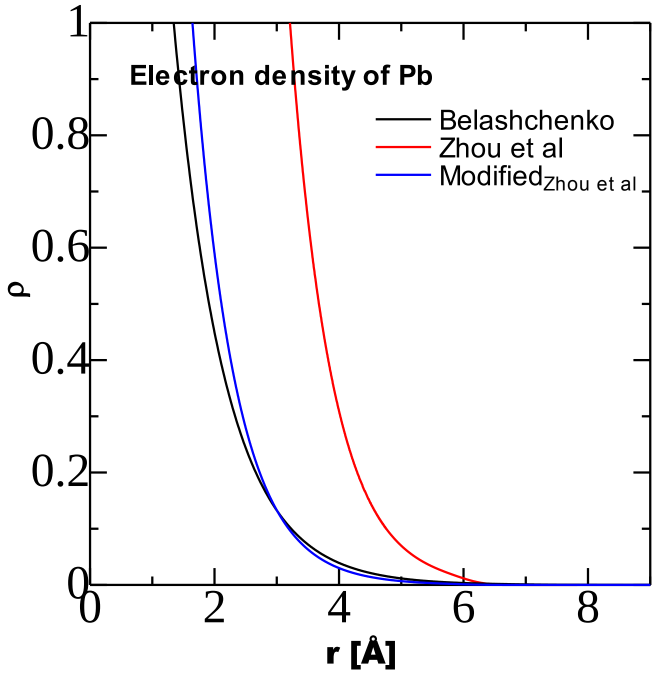

Fig. 5.13 Electron density of Pb by Zhou after modification compares to that by Belashchenko.

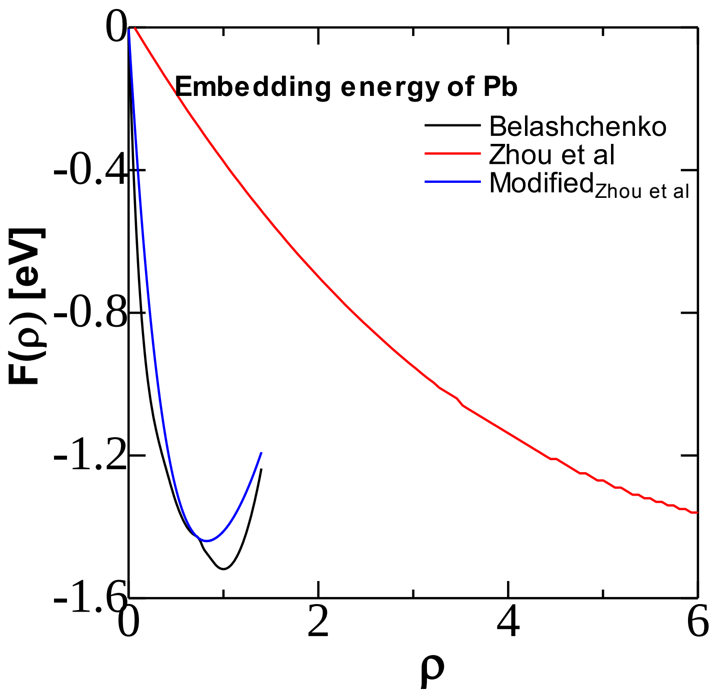

Fig. 5.14 Embedding energy of Pb by Zhou after modification compares to that by Belashchenko.

The black lines in both figures denote the results calculated by using Belashchenko's parameters and the red lines and blue lines show the results calculated by Zhou's parameters before and after modification. It is easily found that the electron density and embedding energy are comparable to the results obtained by using Belashchenko's parameters. Meanwhile, the summation of total potential energy of 2 Pb atoms before and after modification show the same results as plotted in **figure 5.15**.

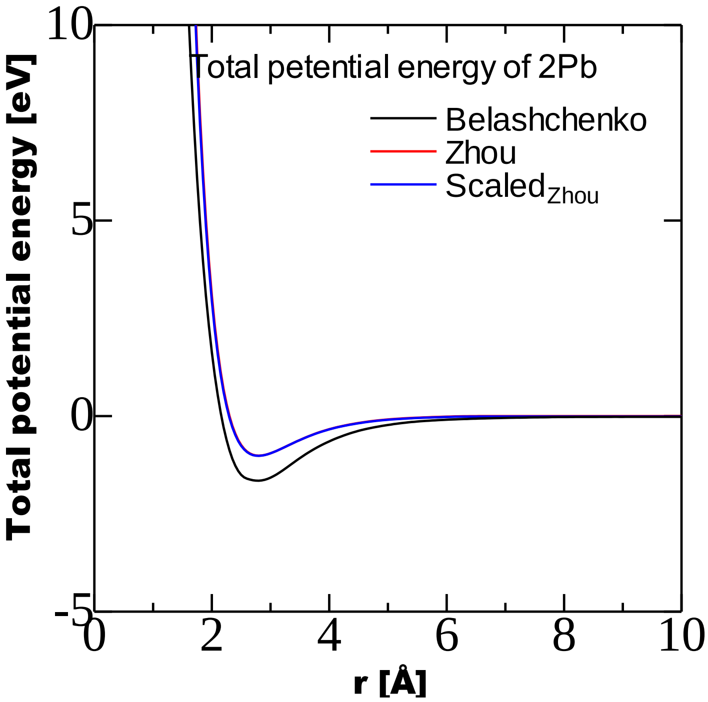

Fig. 5.15 Comparison of total potential energy of 2Pb atoms calculated by using parameters of Zhou before and after modification. Meanwhile the results are also compared to that calculated by using Belashchenko's parameters.

Therefore, modification factor 0.097, named sfac1, is used to modify Fe and Ni parameters developed by Zhou firstly. Then, the substitution energies of Fe and Ni for Pb and Bi are computed by using AIMD and EAM simulations. The modification factor is calibrated by fitting the substitution energies obtained by classical MD simulation using EAM potential to those obtained by AIMD. In the classical MD simulation, by considering the composition of LBE, a simulation box with 59 Pb atoms and 69 Bi atoms is prepared. The replacement of 1 Fe or 1 Ni atom is performed for each Pb and Bi atom after the simulation system equilibrates. Then, the weighted average of Fe and Ni substitution energy are calculated and compared to the results obtained by AIMD, respectively. The modification factors sfac1-sfac8 are chosen as 20%, 40%, 60%, 80%, 100%, 120%, 130% and 150% bigger than 0.097. **Table 5.9** and **table 5.10** show the detailed value of the modification factors and the weighted average value of Fe and Ni substitution energies against the modification factor.

On the other hand, the AIMD simulation is performed in a cubic cell which contains 59 Pb atoms and 69 Bi atoms. The simulation is done in an NVT ensemble using Nose-Hoover algorithm **[5-19]**. The initial coordination of atoms is from a geometry determined with a LAMMPS NPT simulation performed at the same temperature using the cell volume also determined by LAMMPS. The time step of AIMD simulation is 3.0 fs and the energy cutoff is 105 eV. The AIMD simulation is performed using ultrasoft pseudopotentials for Pb and Bi considering explicitly only the valence electrons. The energy is computed using the generalized gradient approximation with the PBE exchange-correlation functional. A 2×2×2 K-point mesh constructed using the Monkhost-Pack scheme **[5-20]** is used to sample the Brillouim zone. The calculation results of Fe and Ni substitution energy for Pb and Bi are also included in **Table 5.9** and **Table 5.10**. It is clearly seen that the weighted average of substitution energy calculated by classical MD simulation increases from negative to positive value by increasing the modification factor.

Table 5.9 The average of Fe substitution energy by Pb / Bi atom

Modification factor (Shorten as sfac)	Averaged replacement energy of Pb by Fe [Kcal/mol]	Averaged replacement energy of Bi by Fe [Kcal/mol]	Weighted average [Kcal/mol]
sfac1=0.0974586	-38.90	-35.04	-36.82
sfac2=0.11695	-29.38	-24.95	-26.99
sfac3=0.13644204	-20.89	-16.55	-18.55
sfac4=0.15593376	-14.41	-10.15	-12.11
sfac5=0.17542548	-8.561	-4.273	-6.25
sfac6=0.1949172	-3.664	0.1059	-1.632
sfac7=0.21440892	0.545	4.122	2.473
sfac8=0.22415478	2.050	6.922	4.676
sfac9=0.2436465	5.330	8.835	7.219
AIMD calculation	-21.55	-12.19	-16.50

Table 5.10 The average of Ni substitution energy by Pb / Bi atom

Modification factor (Shorten as sfac)	Replacement energy of Pb by Fe [Kcal/mol]	Replacement energy of Bi by Fe [Kcal/mol]	Weighted average [Kcal/mol]
sfac1=0.0974586	-30.83	-26.01	-28.23
sfac2=0.11695	-20.76	-16.36	-18.39
sfac3=0.13644204	-13.59	-9.027	-11.13
sfac4=0.15593376	-9.180	-3.574	-6.158
sfac5=0.17542548	-3.055	1.669	-0.509
sfac6=0.1949172	2.158	5.578	4.002
sfac7=0.21440892	5.375	8.560	7.092
sfac8=0.22415478	6.766	10.15	8.592
sfac9=0.2436465	9.697	12.88	11.42
AIMD calculation	-2.97	6.07	1.904

The plots of Fe and Ni substitution energy against modification factor are shown in **figure 5.16**. The black plots denote the Fe substitution energy and the red plots denote the Ni substitution energy versus modification factor. The solid lines show the linear approximation. It is shown that the substitution energy of Fe and Ni show linearity with the scaling factor. The classical MD calculation result of Fe substitution energy is mostly near to the result obtained by AIMD calculation when the modification factor is 0.15. However, in case of Ni substitution energy, the result obtained by classical MD simulation is comparable to the AIMD calculation result when the modification factor is chosen roughly as 0.19. Thus, the modification factor for Fe and Ni is determined as 0.17 by taking the average of 0.15 and 0.19, eventually. The electron density and EAM potential of Fe and Ni are modified by this factor.

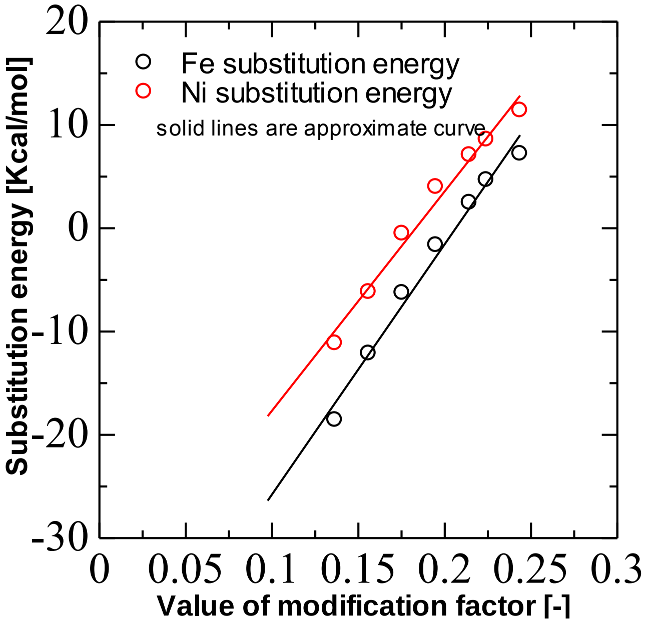

Fig. 5.16 Fe and Ni substitution energy against the modification factor.

5.3. Validation of the liquid alloy models

In order to validate the liquid models of LBE and Pb-17Li, dynamics simulations are performed to calculate the density, volumetric heat capacity, heat capacity and viscosity of both liquid alloys. Then, the simulation results are compared to the experimental results **[5-21]**.

5.3.1. Simulation detail

The MD simulations are performed in a cubic box which the initial side length is 70 angstrom. The simulation box contains 8000 atoms. By considering the composition of liquid lead alloys, the simulation box contains 3584 Pb atoms and 4416 Bi atoms in case of LBE and there are 6656 Pb atoms and 1344 Li contained in the simulation box. Thus, the composition percentage of LBE model is 44.6wt% Pb together with 55.4wt% Bi and the composition percentage of lithium is 16.8mol%. The size of the initial Verlet algorithm **[5-22]** with a time step of 0.5 fs is used to integrate the equation of motion. Simulations in isothermal-isobaric ensemble (NPT) and canonical ensemble (NVT) were performed using Nose-Hoover algorithm **[5-19]** with a time constant of 0.05 ps and 0.5 ps for thermostat and barostat, respectively. The global cut-off distance is set as 9.05 Å and the periodic boundary conditions are imposed to the simulation systems. The systems are equilibrated for 100,000 time steps and after equilibration, the results are extracted by performing time average of 500,000 time steps. All the simulations including the diffusion simulations which is described in chapter 6 are performed using the open-source package Large-scale Atomic/Molecular Massively Parallel Simulator (LAMMPS) **[5-23]** and are carried out in serial mode on a desktop workstation.

5.3.2. Data analysis

Data analysis is generally performed by dividing the production run into m=1000 equally sized blocks of time. Average values for a given property A are calculated for each block of time using every time steps within that block. Average values are calculated by averaging the block averages. The uncertainty ΔA for the simulation is then taken to be $\sqrt{\sigma_A^2 / m}$, where σ_A^2 is the variance of the population of block averages. The data analysis method can be also used for diffusion coefficient calculations which are described in chapter 6 and 7.

5.3.2. Thermal physical properties of liquid LBE

(1) Pair distribution function

The pair distribution functions of Pb-Bi, Pb-Pb and Bi-Bi within the liquid LBE at temperature of 573K are computed and denoted in black, blue and red solid lines in **figure 5.17**. The pair correlation of Pb-Bi is between that of Pb-Pb and that of Bi-Bi. It is simply because the mixing rule for calculating the two-body interaction within the alloy which is a pair potential average of two pure composed metals by considering the electron density ratio of those two composed elements. Then, the present result of Pb-Bi correlation are comparable to the result obtained by AIMD simulation **[1-21]** which is presented in green line in **Fig. 5.17** and the diffraction experiment results denoted in plot **[5-24]**. Thus, it is assumed that the LBE model by using EAM potential has been represented.

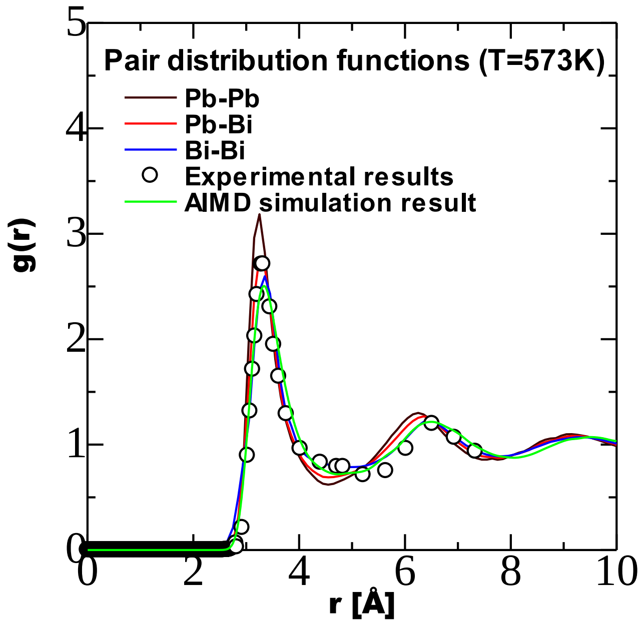

Fig. 5.17 Present simulation results of pair distribution within liquid LBE at temperature of 573K compared to AIMD simulation result [1-21] and experimental results [5-24].

(2) Density and volumetric thermal expansion

The density of modeled liquid LBE is computed by using isothermal isobaric ensemble with Nose barostat for pressure control. The simulation results are plotted and compared to the experimental empirical correlation **[5-22]** as shown in **figure 5.17**. The standard deviation of density obtained by simulation increases with the temperature and it is roughly 0.013 g/cm^3. The simulation results are less than 2% bigger than the experimental result. The linear approximation of the simulation results can be expressed as

$$\rho_{\mathrm{LBE}}[\mathrm{kg/m^3}] = 11218 - 1.385T\ . \tag{5.25}$$

It is known that the density of liquid metals changes with temperature due to thermal expansion related to anharmonicity of interaction forces. The density and coefficient of volumetric thermal expansion at constant pressure p are related as:

$$\beta_{\mathrm{p}}(T) = \frac{1}{\mathrm{V}}\left(\frac{\partial V}{\partial T}\right)_{\mathrm{p}} = -\frac{1}{\rho}\left(\frac{\partial \rho}{\partial T}\right)_{\mathrm{p}}\ . \tag{5.26}$$

According to this formula, the coefficient of thermal expansion of LBE can be calculated from **Eq.6.1.** The resulting value is

$$\beta_{\mathrm{LBE}}(T) = \frac{1}{8090 - 1.385T} \qquad [\mathrm{K}^{-1}], \tag{5.27}$$

The thermal expansion of PbBi at 800K is $1.28\times10^{-4}[\mathrm{K}^{-1}]$, which is roughly the same as the experimental result $1.32\times10^{-4}[\mathrm{K}^{-1}]$ **[5-25]**.

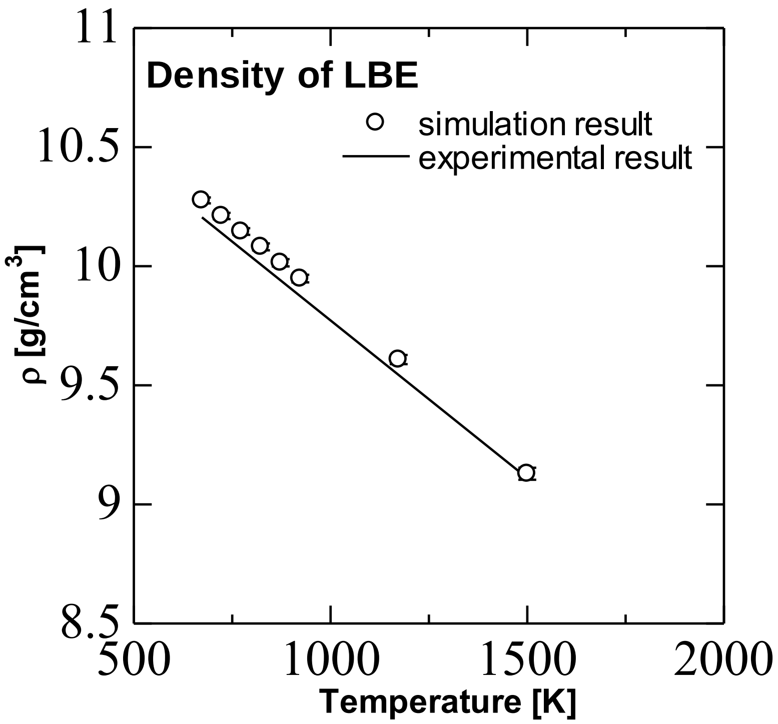

Fig. 5.18 Simulation results of density compared to experimental results.

(3) Isobaric heat capacity

Isobaric heat capacity can be obtained by isothermal isobaric ensemble with Nose barostat for pressure control. The heat capacity C_p measured at constant pressure is expressed as

$$C_p = \left(\frac{\delta q}{dT}\right)_p = \left(\frac{\partial H}{\partial T}\right)_p = T\left(\frac{\partial S}{\partial T}\right)_p . \tag{5.28}$$

The enthalpy H is expressed as $H=U+pV$, where U is the total energy, p is the pressure and V is the volume of the system. The isobaric heat capacity C_p is proportional to the enthalpy against temperature. The calculation results are shown in **figure 5.18**. The plots in the figure denote the calculated heat capacity against temperature, and the dashed line is corresponded to the empirical correlation by experiment.

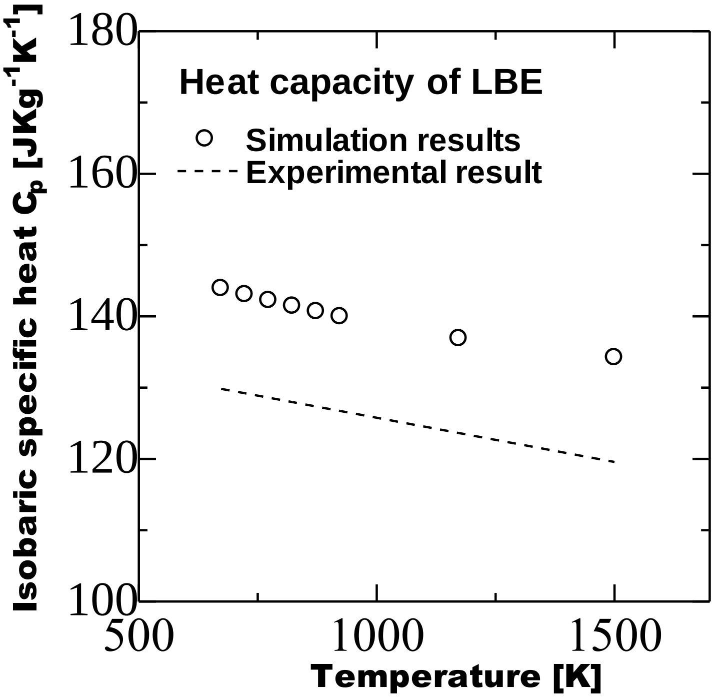

Fig. 5.19 Temperature dependency of isobaric heat capacity.

The plots show the simulation results and the dashed line is corresponded to the empirical experimental result.

It is shown that the simulation results are roughly 10% bigger than the experimental results **[5-24]**. However, Martynov et al. obtained the heat capacity at temperature of 800K experimentally as 146 J・Kg^{-1}・K^{-1} **[5-26]** which is closer to present result. The heat capacity is influenced by the vibration of atoms and this vibration energy cannot been accurately calculated by classical MD simulations **[5-27]**. Thus, in order to obtain the accurate heat capacity, AIMD simulation is required. One the other hand, since the empirical experimental formula is obtained by fitting the experimental results to Kopp's law **[5-28]**, although there is large difference between the experimental results **[5-24]** and the theoretical results especially at high temperature. Therefore, there is unreliability exists in the empirical experimental formula. It is suggested that further experimental and analytical work is required to obtain a reliable result of heat capacity.

(4) Viscosity

The shear viscosity of liquid can be derived from equilibrium or non-equilibrium methods. Typical equilibrium molecular dynamics (EMD) methods use either Green-Kubo integral **[5-29]** or Einstein relation **[5-30]** to relate fluctuations of off-diagonal components of the pressure tensor to viscosity. However, these expressions are only exact in the limit of infinite simulation time and infinite simulation box length, so that extrapolation to the zero frequency and zero wave vector limits may be required. Because of the low signal to thermal noise ratio, EMD simulations generally require many simulation steps to acquire sufficiently good statistics.

Compared with EMD, non-equilibrium MD (NEMD) methods can potentially avoid some of the high computational cost associated with EMD simulations by including a signal significantly larger than the background thermal noise. There are two types – transient and steady state NEMD methods developed. Transient methods generally involve either setting an initial velocity profile and tracking its decay or applying a field and tracking the growth of the resulting perturbation. As the steady state NEMD methods for viscosity calculation, the SOLLD **[5-31, 5-32]** and related methods involving sliding-brick boundary conditions or a deforming simulation boundaries and measure viscosity via the appropriate off-diagonal component of the pressure or stress tensor. A thermostat is required to remove energy injected via viscous heating. The same as EMD, measurement of viscosity at low shear rates with NEMD may require long simulations due to relatively large fluctuations in the pressure tensor.

Unlike normal NEMD methods as explained as above, which set the strain or shear field and measure the response of stress or momentum flux of the system, the reverse-NEMD (RNEMD) method, which was developed by Muller Plathe **[5-33]** is used to calculate the viscosity of liquid LBE together with liquid Pb-17Li as written in next chapter. The RNEMD imposes the hard-to measure flux and computes the resulting easy-to measure shear filed. Since energy and momentum are both conserved, RNEMD does not require thermostatting.

The shear viscosity connects a shear field with a flux of transverse linear momentum. The shear field is a gradient of one component of the fluid velocity, i. e. x direction, with respect to another direction say z direction, $\partial v_x / \partial z$. It is also denoted as the shear rate. The momentum flux $j_z(p_x)$ is collinear: it is the x component of the momentum flux p_x transported in z direction per given time and per unit area, as shown in **figure 5.19**. It can also be regarded as an off-diagonal (xz) component of the stress tensor. The proportionality coefficient is the shear viscosity η, according to **Eq** (5.29).

$$j(\mathrm{p}_x) = -\eta \frac{\partial v_x}{\partial z} . \qquad (5.29)$$

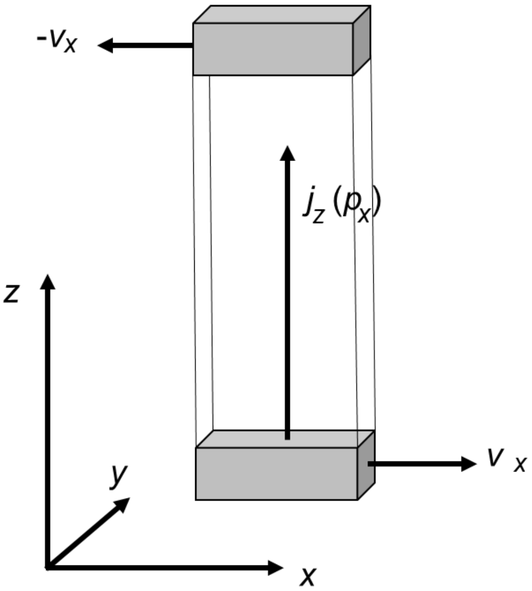

Fig. 5.20 Geometry of the non-equilibrium situation.

The simulation box is divided into 40 bins along z axis after the system becomes equilibrium. The momentum swaps are performed between particles in the first layer (bin=1) and middle layer (bin=21). **Figure 5.20** shows one of the velocity profiles at

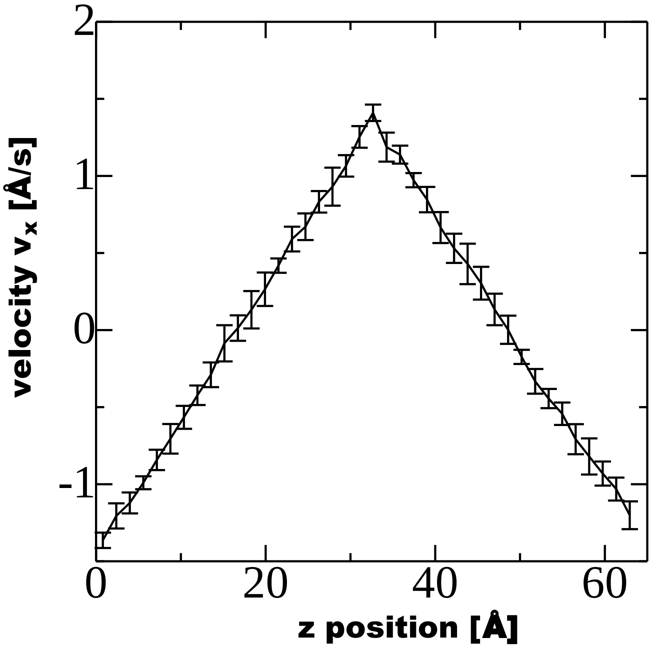

Fig. 5.21 Velocity profile in the simulation box.

temperature of 823K. The calculation uncertainties in the value of v_x for any given bin, are represented in the figure by vertical error bars. The uncertainties of the velocity are appropriate. The velocity profile are symmetric and shows a good linearity against distance. The slop of half of the velocity profile is corresponded to the shear rate $\partial v_x / \partial z$. Then, the viscosity versus temperature can be obtained and the results are represented in **Fig. 5.21** and compared to the experimental empirical correlation **[5-24]**. The solid line denotes the experimental result and the plots are corresponded to the simulation results. The simulation results are less than 4% smaller than experimental results. The linear approximation of the simulation results which is denoted in dashed line can be expressed following the Arrhenius-type equation

$$\eta\,[\mathrm{Pa}\cdot\mathrm{s}] = 4.84\times10^{-4}\exp(5.02\times10^{3} / \mathrm{R}T)\,. \qquad (5.30)$$

where R is the molar gas constant and T is the temperature in kelvin. The slope of the curve denotes the viscous activation energy of liquid LBE and it is obtained as 5.02×10^{3} J/mol as shown in **Eq. 6.6**. It is roughly the same as the experimental result.

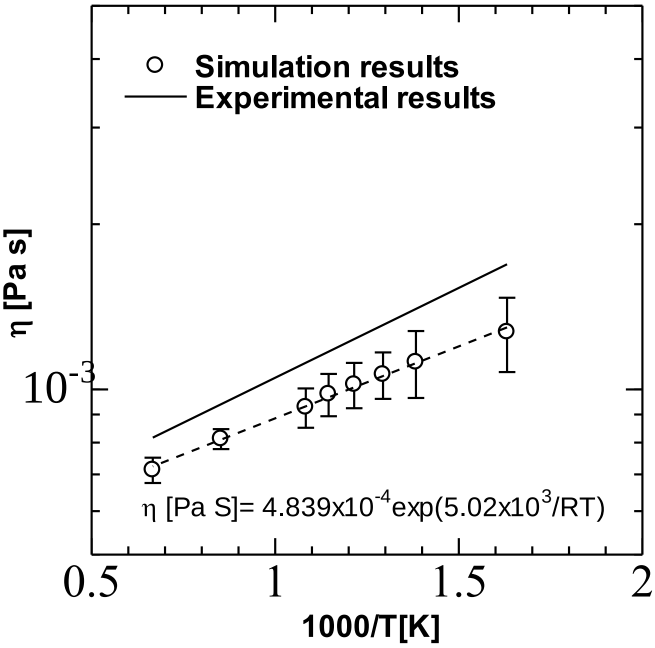

Fig. 5.22 Simulation results of viscosity compared to the experimental result.

Overall, it is seen that the current simulation results of pair distribution function, density, heat capacity and viscosity show comparable results with the experimental results or the AIMD simulation results. Therefore, it is indicated that the EAM model of liquid LBE model is valid.

5.3.3. Thermal physical properties of liquid Pb-17Li

(1) Pair distribution function

The pair distributions of Pb-Pb, Pb-Li and Li-Li within the liquid Pb-17Li at temperature of 723K are shown in **figure 7.1**. The pair distribution of Pb-Li shows the intermediate value between that of Pb-Pb and Li-Li. Since there is no diffraction database of the pair correlation within the liquid Pb-17Li, the comparison and further discussion cannot be done. It is suggested that the experimental study of the pair correlation in liquid Pb-17Li is required.

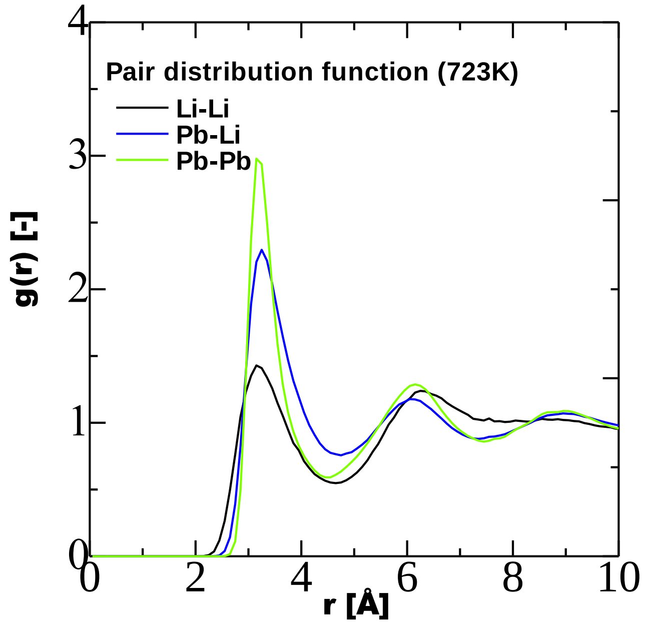

Fig. 5.23 Pair distributions within the liquid Pb-17Li at temperature of 723K.

(2) Density and volumetric thermal expansion

The density is computed by using isothermal isobaric ensemble with Nose barostat for pressure control. The simulation results are plotted and compared to the empirical correlation by experiment **[5-34]** as shown in **Fig. 5.23**.

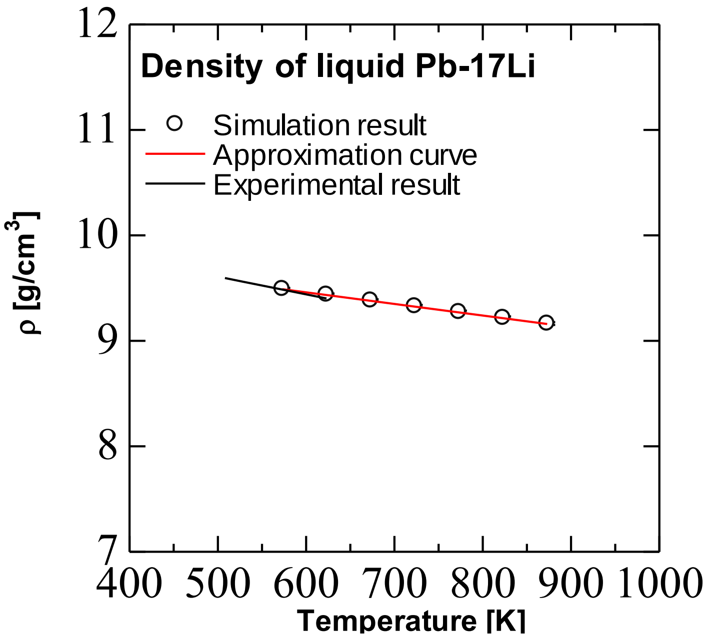

Fig. 5.24 Density of Pb-17Li compared to the experimental result.

The standard derivation of density obtained by simulation increases with the temperature and it is roughly 0.012 g/cm^3. The simulation results are 0.7% bigger than the available experimental results in temperature range of 508K-625K. The density of Pb-17Li at melting temperature of 508K is obtained as 9.56 g/cm^3 by simulation and it is extremely smaller than the experimental result of 9.94 g/cm^3 **[5-35]**. Then, the empirical formula of Pb-17Li density in temperature range of 573-873K is analytically obtained as

$$\rho_{\text{Pb-17Li}}[\text{kg}/\text{m}^3] = 10138 - 1.3T\,. \tag{5.31}$$

From this formula, the volumetric thermal expansion coefficient temperature can be obtained following the definition which has been explained in previous chapter and the obtained formula is shown as:

$$\beta_{\text{Pb-17Li}}[\text{K}^{-1}] = \frac{1}{7798 - 1.3T}\,. \tag{5.32}$$

It is know that in temperature range RT<T<450K which is lower than melting point, the relative thermal expansion is a linear function of the temperature and the thermal expansion coefficient is (41±4) ×10^{-6} K^{-1}**[5-34]**. However, the thermal expansion coefficient becomes 10^{-4} K^{-1} after Pb-17Li melt, which is two orders in magnitude bigger than that in solid phase. It is illustrated that the expansion of liquid Pb-17Li is much more largely than that in solid phase.

(3) Isobaric heat capacity

The isobaric heat capacity of liquid Pb-17Li is obtained by isothermal isobaric ensemble with Nose barostat for pressure control. The empirical formula of heat capacity of Pb-17Li at temperature from 573K to 873K can be obtained as

$$\text{C}_\text{p}[\text{J}/\text{Kg}\cdot\text{K}] = -0.03T + 190.24\,. \tag{5.33}$$

Figure 5.24 shows the comparison between the simulation and experimental results. The plots denote the simulation results and the linear approximation is shown in black solid line. The experimental result **[5-34]** is represented in red solid line. It is found that the simulation results are roughly 10% smaller than the experimental results. The standard deviation of the simulation results decreases with increasing the temperature, and it is approximately between 6 and 7J・$Kg^{-1}K^{-1}$. However, the heat capacity of Pb-17Li at melting point of 508K is obtained as 192 J・$Kg^{-1}K^{-1}$ by simulation and 196 J・$Kg^{-1}K^{-1}$ by experiment. The difference between experimental simulation results are allowable, because it is difficult to calculate the vibration energy accurately by classical MD simulation as explained in section 5.3.2. Besides there also exists uncertainties in the experimental results. Further study on heat capacity by both experiment and simulation are required.

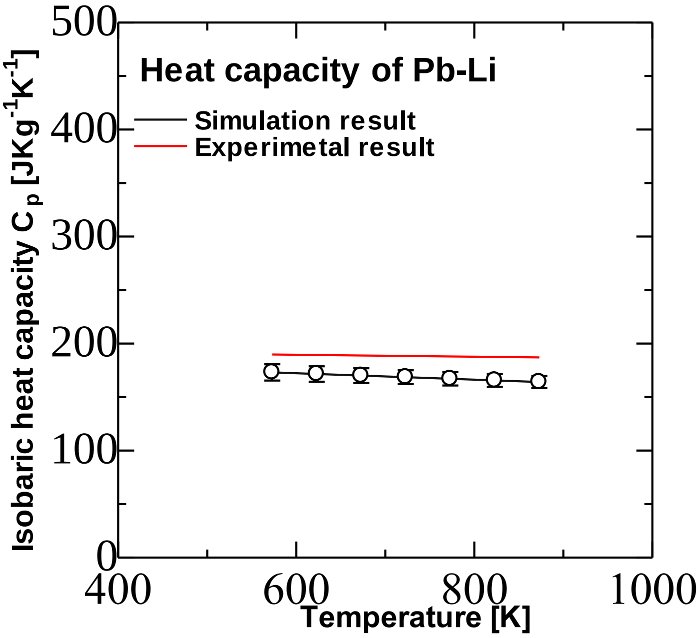

Fig. 5.25 Heat capacity of liquid Pb-17Li. The plots show the simulation results and the linear approximation is shown in black line. The red line denotes the results calculated from the experimental empirical correlation.

(4) Viscosity

The viscosity is computed by using RNEMD method as described in previous section.

The simulation results are shown in plots in **Fig.5.25** and the linear approximation is shown in solid line. The red solid line denotes the calculation result by using the experimental empirical correlation. The simulation results show good agreements with the experimental results **[5-34]** at low temperature and less than 4% bigger than the experimental results at high temperature. The deviations of the simulation results are very small and empirical formula of viscosity can be obtained following Arrhenius equation:

$$\eta_{\text{Pb-Li}}[\text{Pa}\cdot\text{s}] = 3.826\times10^{-4}\exp\left(\frac{924}{\text{T}}\right). \tag{5.34}$$

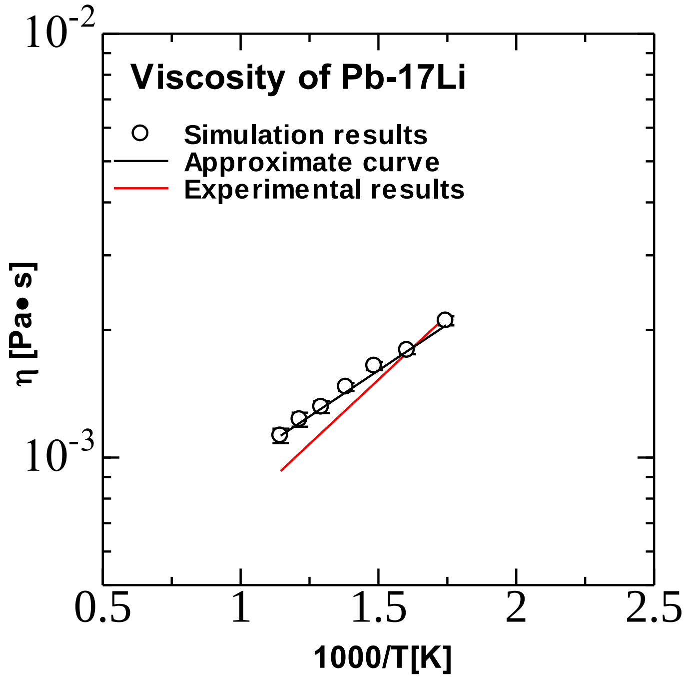

Fig. 5.26 Viscosity of liquid Pb-17Li. The plots show the simulation results and the linear approximation is shown in black line. The red line denotes the results calculated from the experimental empirical correlation.

Overall, it is seen that the current simulation results of density, heat capacity and viscosity are in comparable agreement with the experimental results, although further studies are required in the field of pair distribution within liquid Pb-17Li and the heat capacity. Therefore, it can be indicated that the EAM model of liquid Pb-17Li model is also valid.

Therefore, the EAM model of liquid Pb-17Li is valid since although the simulation results show some differences with the results obtained by experimental empirical formula in heat capacity and viscosity. However, the differences are small and there are also several uncertainties in the experimental database.

5.4. Conclusions

The embedded atom model is used to represent the many-body interactions within the liquid LBE and Pb-17Li and the pair distributions, density, volumetric thermal expansion, heat capacity and viscosity of them are calculated and compared to the experimental results and also the AIMD results. The simulation results of those thermal physical properties are comparable with the literature database. Besides, in order to simulate the Fe and Ni diffusion in liquid LBE and Pb-17Li, the atomic pair interactions of Fe-Pb, Ni-Pb, Fe-Bi, Ni-Bi, Fe-Li and Ni-Li are developed and the validity of the developed pair interactions is verified by calculating the substitution energy with AIMD simulation. It is concluded that:

(1) The EAM models of liquid LBE and Pb-17Li are valid and they can be used to perform the Fe and Ni diffusion simulations ;

(2) The cross pair interactions of Fe-Pb, Ni-Pb, Fe-Bi and Ni-Bi within the liquid alloys has been successfully represented.

References

[5-1] A. Rahman, Phys. Rev. 136, 2A, pp405-411(1964).

[5-2] D. Marx and J. Hutter, “Ab initio molecular dynamics: basic theory and implementation”, Cambridge University Press, 2009.

[5-3] F. Ercolessi, “A molecular dynamics primer”, Spring College in Computational Physics, ICTP, Trieste, 1997.

[5-4] F. Ercolessi, M. Parrinello and E. Tosatti, Philos. Mag. A 58, 213 (1988).

[5-5] M. S. Daw and M. I. Baskes, phys. Rev. B 29, 6443 (1984).

[5-6] S. M. Foiles, M. I. Baskes, and M. S. Daw, Phys. Rev. B 33, 7983 (1986).

[5-7] M. J. Stott and E. Zaremba, Phys. Rev. B 21, 2131 (1980).

[5-8] R. A. Johnson, Phys. Rev. B 39, 12554 (1989)

[5-9] M. I. Baskes, Phys. Rev. B 46, 2727 (1992)

[5-10] D. K. Belashchenko, Uspekhi Fizicheskikh Nauk 183 (12) 1281-1322 (2013)

[5-11] R. R. Zope and Y. Mishin, Phys. Rev. B 68, 024102 (2003)

[5-12] M. I. Baskes, J. S. Nelson and A. F. Wright, Phys. Rev. B 40, 6085 (1989)

[5-13] D. K. Belashchenko, Russ. J. Phys. Chem. A, Vol. 86, No. 5, pp. 779-790

[5-14] D. K. Belashchenko, Inorg. Mater. 48, 79 (2012) [Teplofiz. Vys. Temp. 50 354 (2012)]

[5-15] W. Schommers, Phys. Lett. A 49, 197 (1973)

[5-16] W. Schommers, Phys. Rev. A 28 3599 (1983)

[5-17] X. W. Zhou, R. A. Johnson and H. N. Wadley, Phys Rev. B 69, 144113 (2004)

[5-18] http://res.tagen.tohoku.ac.jp/~waseda/scm/ AXS/index.html

[5-19] N. Hoover, J. Chem. Phys. 81, pp. 511-519 (1984)

[5-20] H. J. Monkhorst and J. D. Park, Phys. Rev. B 13. 5188 (1976)

[5-21] V. Loup, Phys. Rev. 159, pp. 98-103 (1967)

[5-22] OECD/NEA, “Handbook on Lead-bismuth Eutectic and Lead Properties, Materials Compatibility, Thermal-hydraulics and Technologies” Chap. 2, pp. 25-99 (2007).

[5-23] http://lammps.sandia.gov/

[5-24] W. Gudowski, A. Mellergard, M. Dzugutov, W. S. Howells and P. Zetterstrom, J. Non-Cryst. Solids 156-158 (1993)

[5-25] H. J. Monkhorst and J. D. Pack, Phys. Rev. B13, 5188 (1976)

[5-26] P. N. Martynov and K. D. Ivanov, IAEA Technical Document IAEA-TECDOC 1056, p177

[5-27] A. Rahman, Phys. Rev. 136, 2A, pp405-411(1964).

[5-28] E. B. Millard, "Physical Chemistry for Colleges", New York, McGraw-Hill, pp96 (1921)

[5-29] R. Kubo, M. Toda, and N. Hashitsume, "Statistical Physical II", New York, Harper Collins (1985)

[5-30] B. Hess, the Journal of Chemical Physics 116, 209 (2002).

[5-31] M. P. Allen and D. J. Tildesley, "Computer Simulation of Liquids", Clarendon, Oxford (1987)

[5-32] D. J. Evans and G. P. Morriss, "Statistical Mechanics of Nonequilibrium Liquids", London (1990)

[5-33] F. Muller-Plathe, Phys. Rev. E 59, 4894 (1999)

[5-34] B. Schulz, Fusion Eng. Design, 14, 199 (1991)

[5-35] P. Nikolopoulos, B. Schulz, J. Nucl. Mater. 82 pp172-178 (1979).

Chapter 6 Molecular dynamics simulation of iron and nickel diffusion in liquid LBE

6.1. Introduction

The classical MD simulation is applied to simulate Fe and Ni diffusion in the valid liquid LBE model and the developed two-body interactions of Fe-Pb, Fe-Bi, Ni-Pb and Ni-Bi are used to represent the potential energies during the diffusion. The purpose of this chapter are denoted that:

(1) To interpret the experimental results of Fe and Ni diffusion in liquid LBE through MD simulations where the diffusion coefficient of Fe and Ni are derived according to Einstein relationship and compared to the experimental results and theoretical results from Stokes-Einstein equation;

(2) To investigate the diffusion mechanism of Fe and Ni in liquid LBE from the atomic level of view and compare the results to each other

The simulation method, results and discussions will be open around September.

Chapter 7 Molecular dynamics simulation of iron and nickel diffusion in liquid Pb-17Li

7.1. Introduction

The classical MD simulation is applied to simulate Fe and Ni diffusion in the valid liquid Pb-17Li model and the developed two-body interactions of Fe-Pb, Fe-Li, Ni-Pb and Ni-Li are used to represent the potential energies during the diffusion. The purpose of this chapter are denoted that:

(1) To interpret the experimental results of Fe and Ni diffusion in liquid Pb-17Li through MD simulations where the diffusion coefficient of Fe and Ni are derived according to Einstein relationship and compared to the experimental results and theoretical results from Stokes-Einstein equation;

(2) To investigate the diffusion mechanism of Fe and Ni in liquid Pb-17Li from the atomic level of view and compare the results to each other.

The simulation method, results and discussions will be open around September.

Chapter 8 Conclusions

As a fundamental study on metallic impurity diffusion in liquid LBE and Pb-17Li, long capillary method and molecular dynamics method are adopted to clarify the diffusion characteristics of Fe and Ni in liquid LBE and liquid Pb-17Li experimentally and analytically.

In ***Chapter 2***, the long capillary method has been designed and established to perform the diffusion experiment, where the capillary with 2 mm inner diameter can successfully use to suppress the convection during the diffusion, and the procedures of controlling the oxygen concentration in liquid LBE by using a mixture gas of 20%H_2 with Ar, eliminating lithium oxides in the molten Pb-17Li together with the oxides reduction for as-received Fe and Ni powders make contribution to the reliability of experimental results. Then, an ion exchange chromatography is developed to elute Fe and Ni from the specimen, and then the concentration analysis is perform by ICP-MS. By using this method, 99.8% of Fe or Ni in the specimen which is obtained in the diffusion experiment can be eluted and the concentration measurement accuracy of Fe and Ni can be improved to 0.002wt%. Finally, the diffusion coefficient is obtained by using least squares method according to Fick's second law.

In ***Chapter 3***, Fe and Ni diffusion in liquid LBE are performed experimentally. It is found that the diffusion coefficients of them increase with temperature, however they are independent with the time. Besides both of the diffusion coefficients show comparable value, although Ni is much more soluble in liquid LBE. The diffusion coefficient becomes one order in magnitude smaller when the oxygen concentration in liquid LBE increases 5 orders in magnitude. Thus, it is illustrated that it is very important to control the oxygen concentration in liquid LBE. Furthermore, through the SEM-EDX analysis of the diffusion specimens, it is found that Ni atoms aggregate during the diffusion, however, there is no such phenomenon observed in case of Fe. Further studies are required in this aspect.

In ***Chapter 4***, the experiments of Fe and Ni diffusion in liquid Pb-17Li are performed. It is found that both of the diffusion coefficients in Pb-17Li shows comparable values. Besides, the diffusion coefficients of Fe in both lead alloys are almost the same.

In ***Chapter 5***, in order to apply the classical MD simulation to study the Fe and Ni diffusion in liquid LBE and Pb-17Li from microscopic view, the embedded atom model is developed and adopted to represent the many body interaction within the liquid metals. The validity of the liquid LBE and Pb-17Li models are verified since the simulation results of density, volumetric thermal expansion coefficient, heat capacity and viscosity of them show comparable with the experimental results. Meanwhile, the two-body interaction potential of Fe-Pb, Fe-Bi, Ni-Fe, Ni-Bi, Fe-Li and Ni-Li are also successfully developed by means of ab-initio MD simulation.

In ***Chapter 6***, the classical MD simulation of Fe and Ni diffusion in the valid liquid LBE are performed. **(The detailed conclusion will be open around September)**

In ***chapter 7***, Fe and Ni diffusion in the valid liquid Pb-17Li are performed by using classical MD simulation. **(The detailed conclusion will be open around September)**

Appendix

[A1] Electrochemical oxygen sensors

Electrochemical oxygen sensors can measure the difference in the chemical potential of oxygen, μ_{O2}, on both sides of a solid electrolyte via the electric potential difference arising between two electric leads that transport the electrons generated or consumed at the opposite electrolyte surfaces. If the oxygen chemical potential on one side of the electrolyte is known (reference electrode), the chemical potential and therefore the oxygen activity and concentration on the other side can be calculated from the sensor output which is corresponded to the electromotive force (EMF) of the galvanic cell formed by the sensor and the measured system.

For example, a simple galvanic cell that describes the oxygen sensor and the measured system is

$$\text{Lead 1, } O_2(g)\ (\mu_{O2})\ |\ \text{Electrolyte}\ |\ O_2(g)\ (\mu_{O2;Ref}),$$

where the right hand side represents the reference electrode with the fixed and known oxygen potential $\mu_{O2;Ref}$. The half-cell reaction proceeding on both sides of the electrolyte is

$$O_2\,(g) + 4e^-\,(\text{electric lead}) \rightleftharpoons 2O^{2-}\,(\text{electrolyte})\ , \qquad \text{(A1.1)}$$

that is, on the side exhibiting the higher oxygen potential, gaseous oxygen and electrons from the electric lead are consumed and the produced O^{2-}ions are transferred onto the electrolyte which is called cathode. On the opposite side of the electrolyte which is called anode, the reverse processes take place so that the overall cell reaction is the transition of gaseous oxygen from the cathode to the anode, as shown in **Fig. A1.1**. Higher oxygen concentration (potential) prevails at the reference electrode.

According to Nernst equation which is derived from the Gibbs free energy under standard conditions, the cell potential can be determined as:

$$\Delta G_{\text{Cell(l)}} = \mu_{O_2} - \mu_{O_2,\text{Ref}_2}\ . \qquad \text{(A1.2)}$$

ΔG_{cell} is related to the EMF of the cell, $E_{\text{Cell (l)}}$, under general conditions via

$$\Delta G_{\text{cell}} = -n\text{FE}_{\text{cell(l)}}\ , \qquad \text{(A1.3)}$$

with n is the number of electrons transferred in the reaction or from balanced reaction, F

is the Faraday constant of 9.65×10^4 C/mol. There are 4 electron transited according to the chemical reaction written in A1.1, so that $E_{Cell\ (l)}$ follows as

$$E_{Cell(l)} = -\frac{\Delta G_{cell}}{4F} = -\frac{\mu_{O_2} - \mu_{O_2,Ref_2}}{4F}, \tag{A1.4}$$

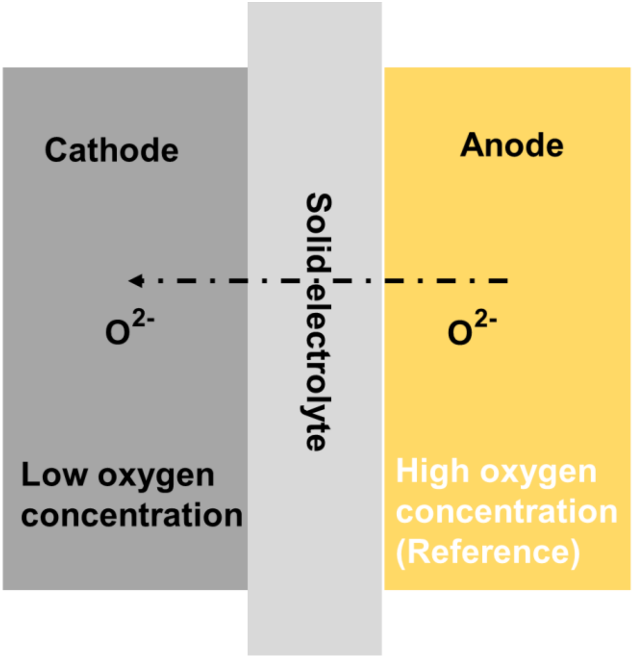

Fig.A1. 1. The oxygen transformation between the electrolytes. The low oxygen concentration side is cathode and the high concentration side is anode. The oxygen in anode is transformed through the solid electrolyte to cathode side.

Substituting the chemical potential of oxygen with respective partial pressures using

$$\mu_{O_2} = \mu_{O_2,Ref} + RT\ln\frac{P_{O_2}}{P_{O_2,Ref}}. \tag{A1.5}$$

yields

$$E_{Cell(l)} = \frac{RT}{4F}\ln\frac{P_{O_2,Ref}}{P_{O_2}}. \tag{A1.6}$$

This equation can be used to calculate the oxygen concentration in liquid LBE.

[A2] Stokes-Einstein equation

Langevin used the stochastic theory to describe the Brownian motion of a large and massive particle in a bath of particles that are much smaller and lighter than itself **[A2-1]**. The problem is characterized by two different time scales, one associated with the slow relaxation of initial velocity of the Brownian particle and another linked to the frequent collisions that the Brownian particle suffers with particles of the bath. Langevin assumed that the forces acting on the Brownian particle consisted two parts: a systematic, frictional force proportional to the velocity **u(t)**, but acting in the opposite sense, and a randomly fluctuating force, **R(t)**, which arises from collisions with surrounding particles. The equation of motion of a Brownian particle of mass *m* is therefore written as

$$m\dot{\mathbf{u}}(t) = -m\xi\mathbf{u}(t) + \mathbf{R}(t) \qquad \text{(A2.1)}$$

where ζ is the friction coefficient. The random force is assumed to vanish in the mean:

$$\langle \mathbf{R}(t) \rangle = 0 \qquad \text{(A2.2)}$$

to be uncorrelated with the velocity at any earlier time:

$$\langle \mathbf{R}(t)\cdot\mathbf{u} \rangle = 0, \quad t > 0 \qquad \text{(A2.3)}$$

and to have an infinitesimally short correlation time, i.e.

$$\langle \mathbf{R}(t+s)\cdot\mathbf{R}(\mathrm{s}) \rangle = 2\pi R_0 \delta(t) \qquad \text{(A2.4)}$$

which in turn means that the power spectrum of the random force is a constant, R_0:

$$\frac{1}{2\pi} = \int_{-\infty}^{\infty} \langle \mathbf{R}(t)\cdot\mathbf{R} \rangle \exp(iwt)dt = R_0 \qquad \text{(A2.5)}$$

These are reasonable assumptions when the Brownian particle is much larger than its neighbors, because even on a short timescale its motion will be determined by a very large number of essentially uncorrelated collisions. When all particles are of the same size, the assumptions less well justified, and a generalization of a type to be described later is required.

The two terms on the right-hand side of the Langevin **equation (A2.1)** are not independent. To see the connection between them, the solution to **Eq. (A2.1)** can be written in the form of

$$m\mathbf{u}(t) = -m\mathbf{u}(0)\exp(-\xi t) + \exp(-\xi t)\int_0^t \exp(\xi s)\mathbf{R}(s)\mathrm{d}s \qquad \text{(A2.6)}$$

On squaring and taking the statistical average by using **equation (A2.3)** and **(A2.4)**, it is obtained that

$$\begin{aligned} m^2\left\langle |\mathbf{u}(t)|^2 \right\rangle &= m^2\left\langle |\mathbf{u}(0)|^2 \right\rangle \exp(-2\xi t) \\ &\quad + \exp(-2\xi t)\int_0^t \mathrm{d}s \quad \int_0^t \mathrm{d}s' \exp[\xi(s+s')]2\pi R_0\delta(s-s')\,. \\ &= m^2\left\langle |\mathrm{u}(0)|^2 \right\rangle \exp(-2\xi t) + \frac{\pi R_0}{\xi}[1-\exp(-2\xi t)] \end{aligned} \qquad \text{(A2.7)}$$

Then, when take the limitation of $t \to \infty$; the Brownian particle will be in thermal equilibrium with the bath regardless of the initial condition. Hence $\left\langle |\mathrm{u}(\infty)|^2 \right\rangle = 3k_{\mathrm{B}}T/m$ and (A2.7) can be rearranged to give an expression for the friction coefficient:

$$\xi = \frac{\pi\beta R_0}{3m} = \frac{\beta}{3m}\int_0^\infty \langle \mathbf{R}(\mathrm{t})\cdot\mathbf{R}\rangle \mathrm{d}t \qquad \text{(A2.8)}$$

and the Brownian particles are to be drawn through the bath by an external field, random collisions suffered by the particle would give rise to a systematic retarding force proportional to the particle velocity. This follows the fluctuation-dissipation theorem. The friction coefficient is also related to the diffusion coefficient. Consider the case when the Brownian particle is initially (*t*=0) situated at the origin (r=0). By multiplying through (A2.1) by **r**(t) and using the results

$$\mathrm{r}\cdot\mathrm{u} = \mathrm{r}\cdot\dot{\mathrm{r}} = \frac{1}{2}\frac{\mathrm{d}}{\mathrm{d}t}r^2 \qquad \text{(A2.9)}$$

$$\mathrm{r}\cdot\dot{\mathrm{u}} = \mathrm{r}\cdot\ddot{\mathrm{r}} = \frac{1}{2}\frac{\mathrm{d}^2}{\mathrm{d}t^2}r^2 - u^2 \qquad \text{(A2.10)}$$

it can obtain that

$$\frac{1}{2}m\frac{\mathrm{d}^2}{\mathrm{d}t^2}|\mathrm{r}(t)|^2 + \frac{1}{2}\xi m\frac{\mathrm{d}^2}{\mathrm{d}t^2}|\mathrm{r}(t)|^2 = m|\mathrm{u}(t)|^2 + \mathrm{r}(t)\cdot\mathrm{R}(t) \qquad \text{(A2.11)}$$

In the statistical mean, equation A2.11 becomes

$$\frac{\mathrm{d}^2}{\mathrm{d}t^2}|\mathrm{r}(t)|^2 + \xi \frac{\mathrm{d}}{\mathrm{d}t}|\mathrm{r}(t)|^2 = \frac{6k_\mathrm{B}T}{m} \tag{A2.12}$$

The solution to equation (A2.12) that satisfies the boundary conditions $\left\langle |\mathrm{r}(0)|^2 \right\rangle = 0$ and

$$\frac{\mathrm{d}}{\mathrm{d}t}\left\langle |\mathrm{r}(t)|^2 \right\rangle\Big|_{t=0} = 2\left\langle \mathrm{r}(0)\cdot\mathrm{u}(0)\right\rangle = 0 \tag{A2.13}$$

$$\left\langle |\mathrm{r}(t)|^2 \right\rangle = \frac{6k_BT}{\xi m}\left(t - \frac{1}{\xi} + \frac{1}{\xi}\exp(-\xi t)\right) \tag{A2.14}$$

At very short times, such $\xi t \ll 1$, the solution becomes

$$\left\langle |\mathrm{r}(t)|^2 \right\rangle \approx \left(\frac{3k_BT}{m} \right) t^2 = \left\langle u^2 \right\rangle t^2 \tag{A2.15}$$

which corresponds to free-particle motion. At very large times ($\xi t \gg 1$), equation (A2.14) reduces

$$\left\langle |\mathrm{r}(t)|^2 \right\rangle \approx \left(\frac{6k_BT}{\xi m} \right) t \tag{A2.16}$$

and comparison with Einstein's relationship for diffusion coefficient [A2-2]

$$D = \lim_{t\to\infty} \frac{\left\langle |\mathrm{r}_i(t) - \mathrm{r}_i(0)|^2 \right\rangle}{6t}, \tag{A2.17}$$

the diffusion coefficient can be obtained as

$$D = \frac{k_\mathrm{B}T}{\xi m}. \tag{A2.18}$$

An estimation of ζ can be obtained from a hydrodynamic calculation of the frictional force on a sphere of diameter of *d* moving with constant velocity **u** in a fluid of shear viscosity η. This leads to the famous results due to Stokes, the precise form of which depends on the assumptions made about the behavior at the surface of the sphere of the velocity field created by the fluid. If the stick boundary condition is used, the fluid velocity at the surface is everywhere taken equal to **u**; in the slip approximation, the normal component of the fluid velocity is set equal to the normal component of **u**, thereby ensuring that no fluid can enter or leave the sphere, and the tangential force acting on the sphere is assumed to vanish. The stress tensor at the surface is then obtained by solving the linearized Navier-Stokes equation **[A2-3]** subject to one of these boundary conditions, supplemented by the requirement that the fluid velocity must vanish at infinite distance from the sphere. When the stress tensor is known, the total frictional force **F** can be calculated by integration over the surface. The final results has the form $\mathbf{F} = -\xi \mathbf{u}$, with

$$\xi = \frac{3\pi\eta d}{m}(\text{stick}), \xi = \frac{2\pi\eta d}{m}(\text{slip}). \qquad \text{(A2.19)}$$

Combination of (A2.18) with (A2.19) leads to the two familiar forms of Stokes-Einstein equation

$$D\eta = \frac{k_{\mathrm{B}}T}{3\pi d}(\text{stick}), D\eta = \frac{k_{\mathrm{B}}T}{2\pi d}(\text{slip}). \qquad \text{(A2.19)}$$

It is a remarkable feature of Stokes-Einstein equation that although it is derived from purely microscopic considerations, and is apparently limited to Brownian particles, it also provides a good, empirical correlation of experimental data on simple liquids, use of the slip boundary condition generally leading to more reasonable values of the effective diameter *d*.

[A3] SEMEXD equipment

Scanning electron microscope (SEM)

The scanning electron microscope, shorten as SEM is an instrument used for the imaging and analysis of a wide range of materials in a wide range of applications **[A3-1]**. It is invented some 50 years ago, but now it has been widely used in metallurgy, geology, biology and medicine. A high-resolution SEM image can show detail down to 25 Angstroms, or better. When used in conjunction with the closely-related technique of energy dispersive X-ray microanalysis (EDX, EDS, EDAX), the composition of individual crystals or features can be determined.

SEMs use an electron beam instead of a beam of light, which is directed towards the specimen under examination. An electron gun located at the top of the device, shoots out a beam of highly concentrated electrons. There are two main types of electron guns used by SEMs. One of them is thermionic guns which can heat a filament until electrons stream away. The other one is field emission guns, the popular choice, which can rip electrons away from their atoms by generating a strong electrical field. The microscope is composed of a series of lensed within a vacuum chamber. The lenses direct the electrons towards the specimen in order to maximize efficiency. The more electrons that are used, the more powerful the magnification is. The SEM usually requires a vacuum chamber to function, as the electron beam must not be obstructed as it passes through the body of the microscope. Small particles could deflect the electrons onto the specimen itself, obscuring the results.

When a specimen is hit with a beam of the electrons known as the incident beam, it emits X-rays and three kinds of electrons: primary backscattered electrons, secondary electrons and Auger electrons. The SEM uses primary backscatter electrons and secondary electrons. The backscattered electron image is used typically to image a polished section and the brightness of this image is dependent on the atomic number of the specimen. For instance, lead will appear brighter than iron. The secondary electron image is used mainly to image fracture surfaces and gives a high resolution image.

A development of the normal high-vacuum SEM is the Environmental SEM, so called ESEM. The ESEM can operate with air in the specimen chamber where the pressure is lower than atmospheric pressure but higher than the high vacuum of a normal SEM. ESEM has the advantage that wet specimens can be examined without dehydrating. It is especially useful for biological specimens and other specimens containing water, such as freshly mixed cement paste.

Energy-dispersive X-ray microanalysis (EDX)

Energy-dispersive X-ray microanalysis, EDX for brevity, is complementary to SEM. It enables the operator to determine the composition of the features in the SEM image **[A3-2]**.

The principle of EDX is that the electron beam generates X-tray within the specimen. Many of these X-rays have energies characteristic of the elements that emitted them. So that the elements presented in the specimen can be known by measuring the energy of the X-rays. Furthermore, the concentration of the element can be also determined when the instrumental conditions are carefully controlled.

There are three principal components to a basic EDX system: the X-ray detector, a bod of electronics called pulse processor which can measure the voltage pulses corresponding to the X-ray energies, and a computer. The X-ray detector is positioned to intercept X-rays emitted from the specimen. When entering the detector, an X-ray generates a small current, which is then converted into a voltage pulse. The size of the voltage pulse is proportional to the energy of the X-ray. A computer measures the voltage pulses over a period of time, say seconds and plots them as a histogram. The histogram shows a spectrum of the X-ray energies that are measured. The elements can be determined by examining the spectrum.

The EDX system may also be able to take control of the SEM scanning system in order to collect elemental distribution maps or elemental line profiles.

[A4] Lennard-Jones potential

Lennard-Jones potential **[A4-1]** is a function of the distance between the centers of two particles. The standard and common Lennard-Jones potential function is written as

$$E = 4\varepsilon\left[\left(\frac{\sigma}{r}\right)^{12} - \left(\frac{\sigma}{r}\right)^{6}\right], \qquad \text{A4.1}$$

where E is the intermolecular potential between two atoms or molecules; ε is the depth of the potential well; σ is the distance where the intermolecular potential between the two particles is zero; *r* is the distance of separation between both particles. The values of ε and σ are measurements of how strongly the two particles attract each other and how close two nonbonding particles can get, respectively. The value of σ is referred to the van der Waals radius and it is equal to one-half of the inter-nuclear distance between nonbonding particles.

The potential curve is shown in **figure A4.1**. When two non-bonding particles apart infinite distance, the possibility of them coming together and interacting is minimal. For simplicity's sake, their bonding potential energy is considered zero. However, the

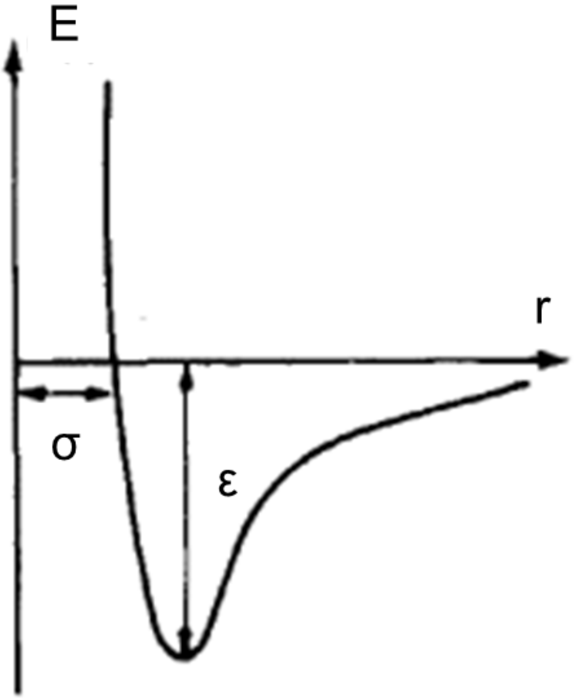

Fig.A4. 1. Lennard Jones potential curve.

probability of interaction increases when the separation distance decreases. The particles come closer together until they reach a region of separation where the two particles become bound; as shown in **Fig.A4.1**, their bonding potential energy decreases from zero to a negative quantity. While the particles are bound, the distance between their centers continue to decrease until the particles reach an equilibrium, specified by the separation distance where the minimum potential energy is reached. Note that the deeper the well depth, the stronger the interaction between the two particles. If the two bound particles are further pressed together, past their equilibrium distance, repulsion begins to occur. It is because the particles are so close that their electrons are forced to occupy each other's orbitals. Repulsion occurs as each particle attempts to retain the space in their respective orbitals. Despite the repulsive force between both particles, their bonding potential energy increases rapidly as the distance of separation decreases.

The value of ε and σ can be fitted to reproduce experimental data or accurate quantum chemistry calculations. Due to its computational simplicity, Lennard-Jones potential is used extensively in computer simulations. However, using Lennard-Jones potential, the number of atoms bonded to an atom does not affect bond strength and the bond energy per atom thus rises linearly with the number of bonds per atom. Instead, the experiments show that bond energy per atom rises quadratically with the number of bonds.

[A5] Radial pair distribution function

The true density of a substance can be expressed in the shell at radius r from a test particle as $\rho g(r)$, where ρ=N/V is the average density and g(r) is called the radial pair distribution function or sometimes the pair correlation function **[A5-1]**. As shown in **figure A5.1**, g(r) is the ratio of the actual density of particles at distance of r to the mean density ρ. The pair distribution function g(r) equals 1 when the local density in a shell is the same as the mean density averaged over the whole volume. Where g(r) > 1, this means the density of particles in that shell is higher than mean density ρ. g(r) can be measured in experiments.

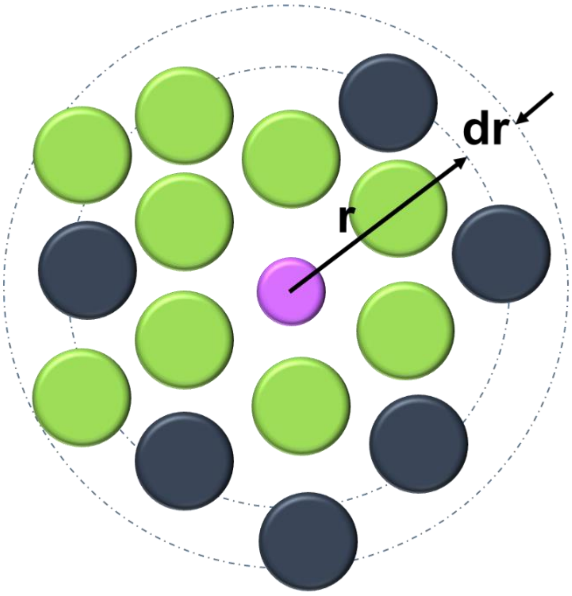

Fig.A5. 1. The pair distribution function g(r).

Figure A5.2 shows three examples of correlation functions. **Fig. A5.2 (a)** shows the correlation function that it is assumed for the van der Waals gas: particles cannot be closer together than a distance r^*, and they are randomly distributed otherwise. **Fig. A5.2 (b)** shows a correlation function for a typical liquid: there is a depletion $g(r) = 0$ for small r because particles cannot overlap, then a peak indicates there is an excess of particles that make up a first neighbor shell, then a slight depletion, followed by a second-neighbor shell, etc. Beyond the third or fourth shell, there is little correlation and $g(r) = 1$. Figure A5.2 (c) illustrates the long-ranged order in crystalline solids.

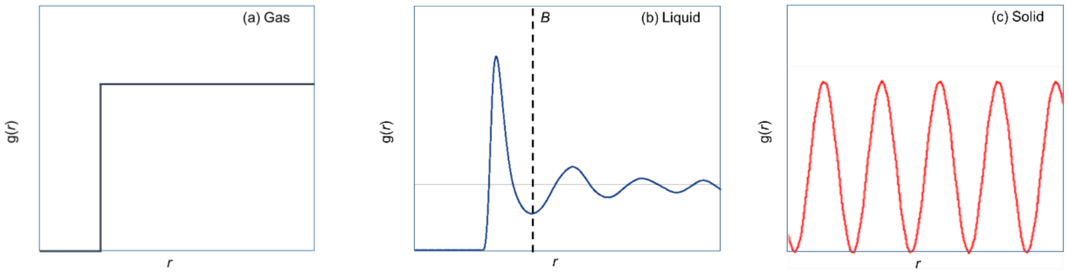

Fig.A5. 2. Examples of pair distribution functions: (a) the model used for the van der Waals gas — hard-core repulsions, and uniform distributions otherwise; (b) typical liquids (B is the limit used to define the first shell of neighbors); (c) solids have long-range order.

A pair distribution function $g(r)$ can be found from experiments using the scattering of electromagnetic radiation. Besides, from this function, we can get other quantities, such as the average number of nearest neighbors of any molecule. Because the volume of a spherical shell at radius r is $4\pi r^2 dr$, the number of molecules in the first-neighbor shell is density× (volume of the shell) = $\rho\ g(r)4\pi r^2 dr$. The total number of molecules in the first shell of a molecule is the integral number of nearest neighbors = $\int_0^B \rho g(r) 4\pi r^2 \mathrm{d}r$, where B is the location shown in **Fig.5.2(b)**. The total number of particles can be obtained by integrating over all the shells:

$$\int_0^\infty \rho g(r) 4\pi r^2 \mathrm{d}r = n - 1 = n\ .$$

[A6] Visualization molecular dynamics

Visualization molecular dynamics, VMD for short, is a molecular graphics program designed for the display, animation and analysis of molecular assemblies **[A6-1]**, in particular biopolymers such as proteins and nucleic acids. VMD can simultaneously display any number of structures using a wide variety of rendering styles and coloring methods. Molecules are displayed as one or more representations, in which each representation embodies a particular rendering method and coloring scheme for a selected subset of atoms. The atoms displayed in each representation are chosen using an extensive atom selection syntax, which includes Boolean operators and regular expressions. VMD provides a complete graphical user interface for program control, as well as a text interface using the Tcl embeddable parser to allow for complex scripts with variable substitution, control loops and function calls. Full session logging is supported, which produces a VMD command script for later playback. High-resolution raster images of displayed molecules mat be produced by generating input scripts for use by a number of photorealistic image-rendering applications. VMD has also been expressly designed with the ability to animate MD simulation trajectories, imported either from files or from a direct connection to a running MD simulation. VMD is the visualization component of MS scope, a set of tools for interactive problem solving in structural biology, which also includes the parallel MD program NAMD, and the MDCOMM software used to connect the visualization and simulation programs. VMD is written in C++, using an object-oriented design. The program includes source code and extensive documentation.

[A7] Experimental results of concentration distribution

1. Concentration distribution of Ni in liquid LBE

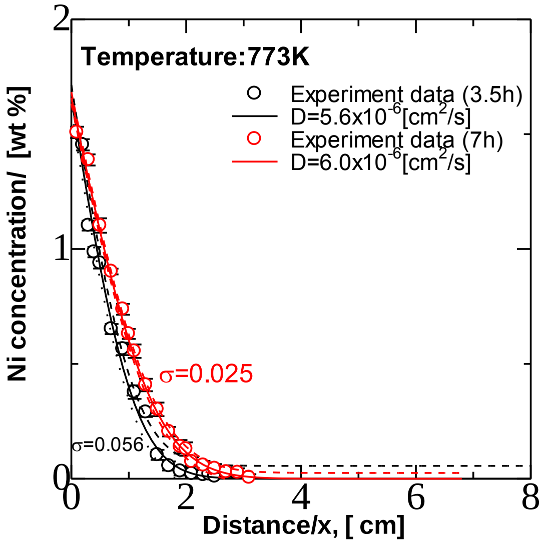

Fig.A7-1 The concentration distribution of diffused Ni in LBE at temperature of 773K**.** The black plots denote the results at time of 3.5 h and the red plots show the results at time of 7 h.

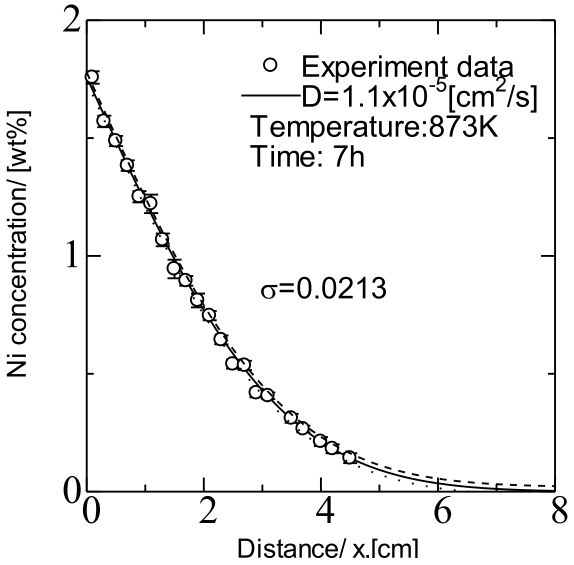

Fig.A7-2 The concentration distribution of Ni in LBE at temperature of 873K

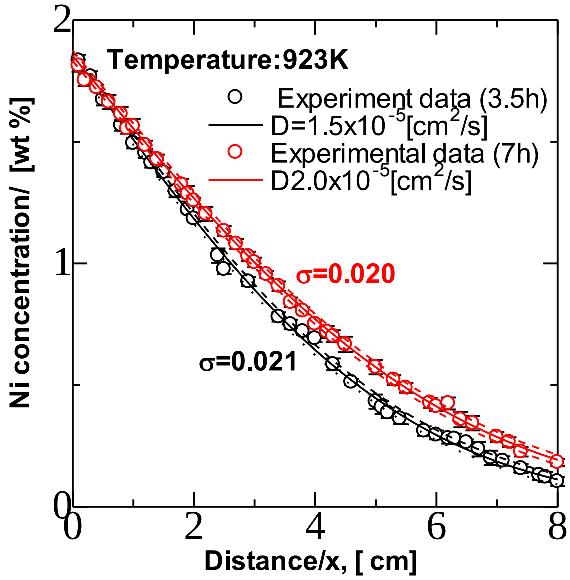

Fig.A7-3 The concentration distribution of diffused Ni in LBE at temperature of 923K**.** The black plots denote the results at time of 3.5 h and the red plots show the results at time of 7 h.

2. Concentration distribution of Fe in liquid Pb-17Li

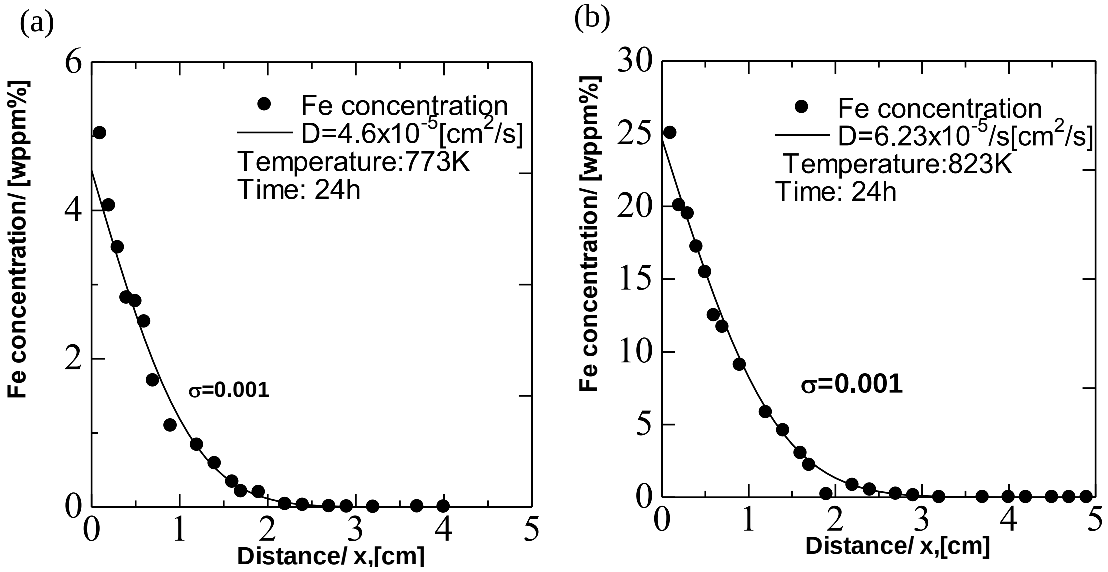

Fig.A7-4 The concentration distribution of diffused Fe in Pb-17Li.

(a) Diffusion temperature is 773K; **(b)** Diffusion temperature is 823K.

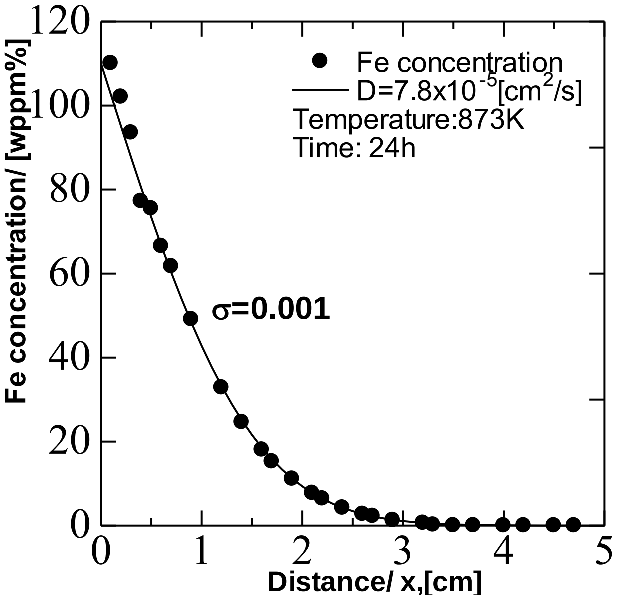

Fig.A7-5 The concentration distribution of Fe in Pb-17Li at temperature of 723K

3. Concentration distribution of Fe in liquid Pb-17Li

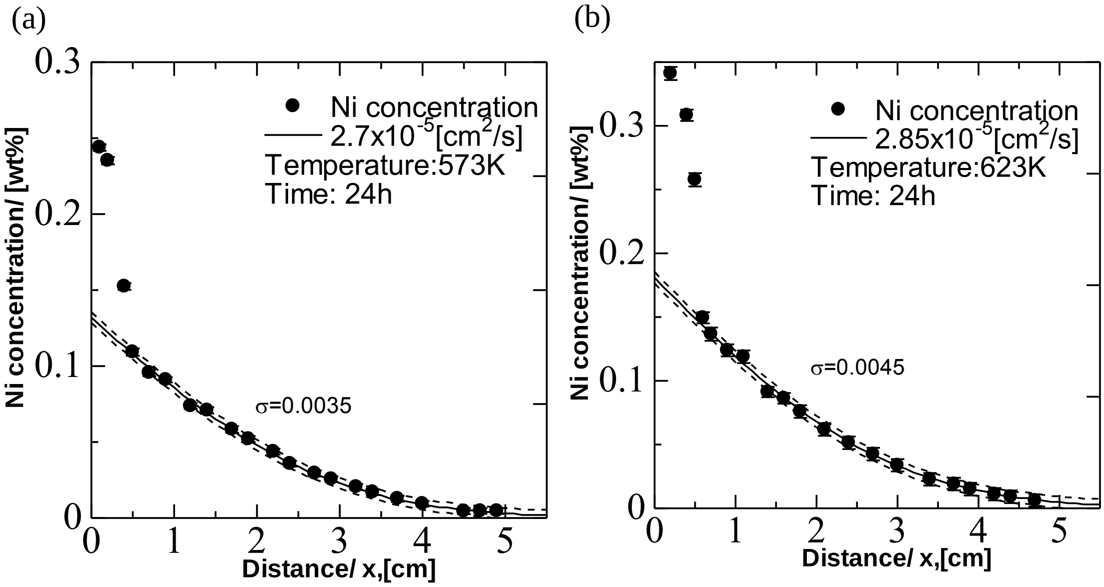

Fig.A7-6 The concentration distribution of diffused Ni in Pb-17Li.

(a) Diffusion temperature is 573K; **(b)** Diffusion temperature is 623K.

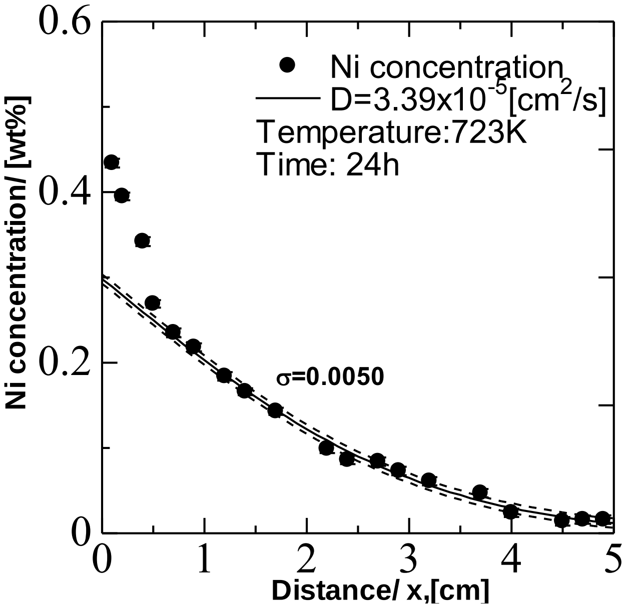

Fig.A7-7 The concentration distribution of Ni in Pb-17Li at temperature of 723K

Reference

[A1-1] C. Schroer, J. Konys, "Physical Chemistry of Corrosion and Oxygen Control in Liquid Lead and Lead-Bismuth Eutectic" Forschungszentrum Karlsruhe, 2007.

[A2-1] P. Langevin, "On the theory of Brownan Motion", C. R. Acad. Sci. (Paris) 146, pp530-533 (1908).

[A2-2] D. Frenkel, B. Smit, "Understanding Molecular Simulation: From Algorithms to Applications", Academic Press, 196, pp97 (2nd Ed).

[A2-3] G. G. Stokes, "On the Theories of the Internal Friction of Fluids in Motion, and of the Equilibrium and Motion of Elastic Solids", Trans. Camb. Phil. Soc. 8, pp287-319 (1845).

[A3-1] D. McMullan, "Scanning Electron Microscopy 1928-1965", Scanning 17 (3), pp175-185

[A3-2] J. Goldstein, "Scanning Electron Microscopy and X-ray Microanalysis", Springer (2012).

[A4-1] J. E. Lennard, "On the Determination of Molecular Fields", Proc. Soc. Lond. A. 106, pp463-477 (1924)

[A5-1] A. D. Ken, "Molecular Driving Forces – Statistical Thermodynamics in Biology, Chemistry, Physics, and Nanoscience", Garland Science, pp483-485 (2nd Ed)

[A6-1] W. Humphrey, A. Dalke and K. Schulten, Journal of Molecular Graphics. Vol. 14, Issue 1, pp 33-38 (1996)

LIST OF PUBLICATION

JOURNAL ARTICLES

(1) Yun Gao, Minoru Takahashi, Masao Nomura, “Experimental Study on Diffusion of Ni in Lead-bismuth Eutectic (LBE),” Energy Procedia, Vol. 71 (2015) pp.313-319

(2) Yun Gao, Minoru Takahashi, Masao Nomura, “Characteristics of Iron and Nickel Diffusion in Molten Lead-bismuth Eutectic,” Mechanical Eng. J., Vol. 2, No.6 (2015), [DOI: 10.1299/mej.15-00149].

(3) Yun Gao, Minoru Takahashi, Masao Nomura, Takashi Nozawa, “Characteristic of Nickel and Iron Diffusion in Molten Lead-17lithium Alloy,” Fusion Eng. Des. (2016) pp1604-1608.

(4) Yun Gao, Guido Raos, Carlo Cavallotti, Minoru Takahashi, “Molecular Dynamics Simulation of Liquid Lead-bismuth Eutectic (LBE),” Procedia Engineering Journal Vol. 157 (2016) pp214-221.

(5) Yun Gao, Guido Raos, Carlo Cavallotti, Minoru Takahashi, “Characteristics of Nickel and Iron Diffusion in Molten Lead-bismuth Eutectic,” Journal of Nuclear Materials, (under review).

(6) Yun Gao, Guido Raos, Carlo Cavallotti, Minoru Takahashi, “Characteristics of Nickel and Iron Diffusion in Molten Lead-17lithium Alloy,” Journal of Nuclear Materials, (to be submitted).

INTERNATIONAL CONFERENCES

(1) Yun Gao, Minoru Takahashi, Masao Nomura, “Experimental Study on Diffusion of Ni in Lead-bismuth Eutectic (LBE),” The 4th Int. Symposium on Innovative Nuclear Energy Systems (INES-4), Nov. 6-8, 2013, Tokyo, Japan.

(2) Minoru Takahashi, Yun Gao, Marion Guihot, Asril Pramutadi, “Overview of Studies on Lead-bismuth Technology in Tokyo Institute of Technology,” International Symposium on Nuclear Back-end Issues and the Role of nuclear Transmutation Technology after the accident of TEPCO’s Fukushima Daiichi Nuclear Power

Stations, Kyoto, 28th November, 2013.

(3) Yun Gao, Minoru Takahashi, Masao Nomura, “Diffusion Coefficients of Metallic Impurities in High Temperature in Lead-bismuth Eutectic (LBE),” 2014, 22nd International Conference on Nuclear Engineering (ICONE-22), ICONE22-30507, Jul. 7-11, 2014, Prague, Czech.

(4) Yun Gao, Minoru Takahashi, Masao Nomura, Takashi Nozawa, “Characteristic of Nickel and Iron diffusion in Molten Lead-17Lithium Alloy,” 2015, 12th International Symposium on Fusion Nuclear Technology (ISFNT-12), P1.095, Sep.14-18, 2015, Jeju, Korea.

(5) Yun Gao, Guido Raos, Carlo Cavallotti, 2015 Molsimeng, “Molecular Dynamics of Liquid Alloys for Generation IV Reactors,” Sep. 16, 2015, Milan, Italy.

(6) Yun Gao, Guido Raos, Carlo Cavallotti, Minoru Takahashi, "Molecular Dynamics Simulation of Liquid Lead-Bismuth Eutectic (LBE)," IX International Conference on Computational Heat and Mass Transfer, ICCHMT 2016, 75, Cracow, Poland, May 23-26, 2016.

(7) Yun Gao, Guido Raos, Carlo Cavallotti, Minoru Takahashi, “ Molecular Dynamics Study on Thermal Physical Propertied of Liquid Pb-17Li”, The Nuclear Materials Conference, Numat2016, 1-40, Montpellier, France, November 7-10, 2016.

DOMESTICS CONFERENCES

(1) 高雲，高橋実，野村雅夫，「細管内における鉛ビスマス中の金属の拡散特性，日本原子力学会　2013 年秋の大会，L12, 2013 年 9 月 3～5 日,八戸工業大学.

(2) 高雲，野村雅夫，高橋実，「液体鉛ビスマスにおける Ni の拡散係数測定，日本質量分析学会第 61 回質量分析総合討論会(2013 つくば), 2P-32, 2013 年 9 月 10～12 日，つくば国際会議場エポカル.

(3) 高雲, 高橋実, 野村雅夫,「細管内における鉛ビスマス中の金属の拡散特性　–第 2 報-金属の性質の影響」，日本原子力学会 2014 年春の大会，F36, 2014 年 3 月 26～28 日，東京都市大学　世田谷キャンパス.

(4) 高雲，高橋実，野村雅夫，(JAEA) 野澤　貴史，朴昶虎，鈴木　達也「細管内における鉛リチウム中の金属の拡散特性」，日本原子力学会 2015 年春の大会，F24, 講演予稿集 P215, 2015 年 3 月 20～22 日，茨城大学　日立キャンパス．

(5) 高雲, Guido Raos, Carlo Cavallotti, 高橋実,「液体鉛ビスマス合金中の金属不純物の拡散特性に関する分子動力学的研究」日本原子力学会 2016 年春の年会（仙台）, 2016 年 3 月 26 日～3 月 28 日,1H08.

AWARDS

(1) 高雲，”日本原子力学会関東・甲越支部第 7 回学生発表会　奨励賞”，2014 年 2 月 28 日

(2) Yun Gao, “The 22nd International Conference on Nuclear Engineering (ICONE-22) Best paper award “, 7th-11th July, 2014

(3) 高雲，”日本原子力学会 材料部会 奨励賞”，2016 年 9 月 8 日